

THESIS

AN OBSERVATIONAL CLIMATOLOGY OF MIDLATITUDE MESOSCALE
CONVECTIVE VORTICES

Submitted by

Eric James

Department of Atmospheric Science

In partial fulfillment of the requirements

For the Degree of Master of Science

Colorado State University

Fort Collins, Colorado

Spring 2009

COLORADO STATE UNIVERSITY

January 29, 2009

WE HEREBY RECOMMEND THAT THE THESIS PREPARED UNDER OUR SUPERVISION BY ERIC JAMES ENTITLED AN OBSERVATIONAL CLIMATOLOGY OF MIDLATITUDE MESOSCALE CONVECTIVE VORTICES BE ACCEPTED AS FULFILLING IN PART REQUIREMENTS FOR THE DEGREE OF MASTER OF SCIENCE.

Committee on Graduate Work

Committee Member Dr. Steven Rutledge

Outside Committee Member Dr. Jorge Ramirez

Advisor Dr. Richard Johnson

Department Head Dr. Richard Johnson

ABSTRACT OF THESIS

AN OBSERVATIONAL CLIMATOLOGY OF MIDLATITUDE MESOSCALE
CONVECTIVE VORTICES

Climatological characteristics of 45 mesoscale convective vortices (MCVs) occurring over the state of Oklahoma during the late spring and summer of four years are summarised. The MCV cases are selected based on vortex detection by an objective algorithm operating on analyses from the Rapid Update Cycle model. Consistent with a previous study, true MCVs represent ~20% of the relative vorticity maxima detected by the algorithm. The MCVs have a broad range of radii and intensities, and MCV longevities range between one and 54 h. The median radius is ~200 km, and the median mid-level relative vorticity is $\sim 1 \times 10^{-5} \text{ s}^{-1}$. Approximately 40% of the MCVs generate secondary convection within their circulations, and MCVs with secondary convection last ~5 h longer, on average, than those without secondary convection.

The mean synoptic-scale MCV environment is determined through constructing a composite of all 45 cases at four different stages in the MCV evolution, defined based on their detection by the objective algorithm. MCV initiation is closely tied to the diurnal

cycle of convection over the Great Plains, with MCVs forming in the early morning, near the time of maximum extent of nocturnal mesoscale convective systems (MCSs). The most significant feature later in the MCV life cycle is a persistent mesoscale trough in the mid-level height field.

Five repeating patterns of precipitation organisation and surface pressure effects are defined based on observations from the Next Generation Weather Radar Network and the Oklahoma Mesonet. Three of these MCV types, comprising 28 of the 45 cases, involve well-defined surface mesolows in the vicinity of the vortex. Eight of the 45 cases are classified as “collapsing stratiform region MCVs”. These MCVs arise from small and asymmetric parent MCSs. As the stratiform region of the MCS weakens, a large and broad mesolow appears beneath its dissipating remnants due to broad subsidence warming, and at the same time the mid-level vortex spins up due to column stretching. Nineteen of the 45 cases are classified as “rear inflow jet MCVs”, and tend to form within large and intense asymmetric MCSs. Rear inflow into the MCS, enhanced by the development of an MCV on the northern side, produces a rear inflow notch and a distinct wake low at the back edge of the stratiform region. One of the 45 cases, called a “surface-penetrating MCV”, contains a large and well-defined surface mesolow and associated cyclonic circulation, apparently due to the strength of the mid-level warm core and the weakness of the low-level cold pool. Three of the 45 cases are classified as “cold

pool dominated MCVs”; these cases contain significant precipitation but no discernable surface pressure perturbations. The remaining 14 cases are classified as “remnant circulation MCVs” containing no significant precipitation and producing no surface pressure effects.

Eric James
Department of Atmospheric Science
Colorado State University
Fort Collins, CO 80523
Spring 2009

TABLE OF CONTENTS

I. Introduction.....	7
II. Data Sources.....	27
III. Methodology.....	42
IV. MCV Climatology.....	62
V. MCV Types.....	96
VI. Discussion.....	145
VII. Conclusions.....	161
References.....	167

I. INTRODUCTION

a. Mesoscale Convective Vortices

Mesoscale convective vortices (MCVs) are a commonly observed and well-documented feature of mature to decaying mesoscale convective systems (MCSs) in both the midlatitudes (e.g., Ogura and Liou 1980; Johnston 1982; Smull and Houze 1985; Menard et al. 1986; Leary and Rappaport 1987; Stirling and Wakimoto 1989; Johnson et al. 1989; Smith and Gall 1989; Murphy and Fritsch 1989; Tollerud et al. 1989; Brandes 1990; Verlinde and Cotton 1990; Hales 1990; Biggerstaff and Houze 1991; Wang et al. 1993; Fritsch et al. 1994; Scott and Rutledge 1995; Bartels et al. 1997; Trier and Davis 2002; Knievel and Johnson 2002; Galarneau and Bosart 2005; Davis and Trier 2007; Trier and Davis 2007; Schumacher and Johnson 2008) and the tropics (e.g., Houze 1977; Leary 1979; Fortune 1980; Gamache and Houze 1982, 1985; Houze and Rappaport 1984; Wei and Houze 1987; Chong et al. 1987; Kuo and Chen 1990; Chen and Liang 1992; Keenan and Rutledge 1993; Jou and Yu 1993; Harr and Elsberry 1996; Yu et al. 1999; Chong and Bousquet 1999; Bousquet and Chong 2000; Litta et al. 2007; May et al. 2008). They are quasi-steady, mesoscale, cyclonic circulations that form in the mid-troposphere within the stratiform regions of MCSs, often persisting after the dissipation

of the parent MCS. MCVs have been documented at a wide range of vertical and horizontal scales, but in general they are on the order of a few hundred kilometres in radius, attaining their maximum relative vorticity near the melting level in the mid-troposphere (typically between 600 and 500 hPa), with a corresponding anticyclone at upper levels (above 500 hPa) (Johnson and Bartels 1992). It has been demonstrated that they are sometimes responsible for the repeated generation of convection in long-lived and serial MCSs (Bosart 1986; Fritsch et al. 1994), which in turn occasionally produce flash flooding (Bosart and Sanders 1981). A subset of MCSs, mesoscale convective complexes (MCCs; Maddox 1980), has been extensively studied both in the United States and abroad (e.g., Maddox 1983; Cotton et al. 1983, 1989; Wetzel et al. 1983; Velasco and Fritsch 1987; Miller and Fritsch 1991; Laing and Fritsch 1993a,b). There are some indications that MCVs are a fundamental feature of MCCs, causing their quasi-circular shape and contributing to their longevity (Velasco and Fritsch 1987; Leary and Rappaport 1987; Menard and Fritsch 1989; Olsson and Cotton 1997a,b). It is also possible that the frequently observed “asymmetric” structure of leading-line/trailing-stratiform mid-latitude MCSs (Houze et al. 1990) is a manifestation of an embedded MCV (Houze et al. 1989; Pandya et al. 2000; see Figure 1.1).

While not the primary focus of such experiments, MCVs have been documented in connection with many meteorological field programmes in the tropics and sub-tropics

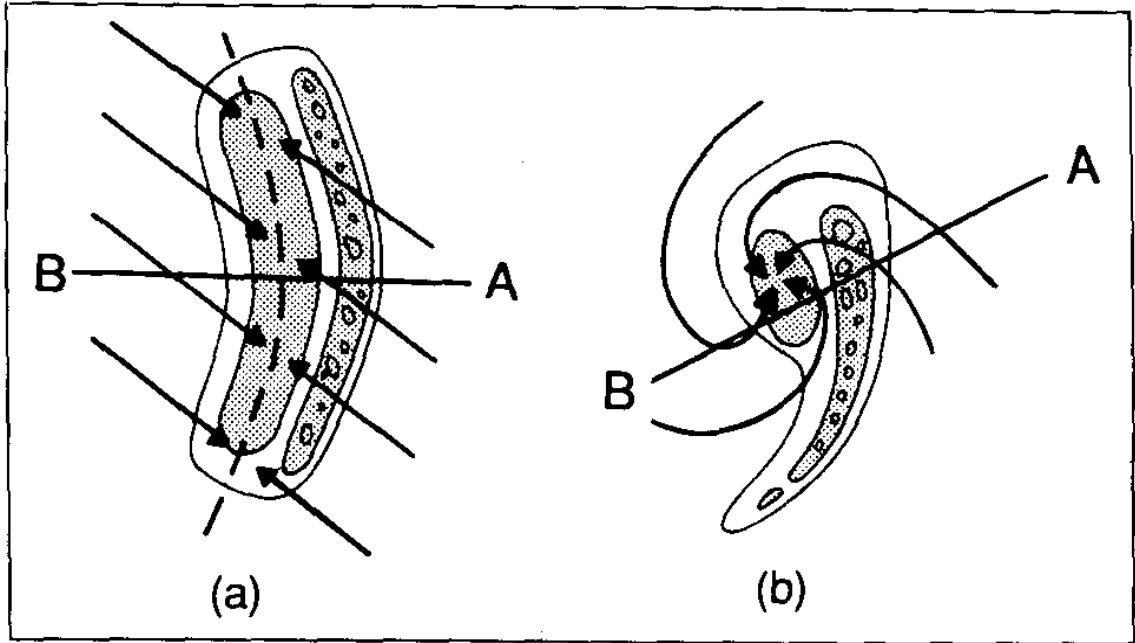


Figure 1.1: Conceptual model of a mid-level horizontal cross-section through (a) an approximately two-dimensional squall line, and (b) a squall line with a well-defined mesoscale vortex in the stratiform region (from Houze et al. 1989).

over the last few decades. A review of progress arising from the 1974 Global Atmospheric Research Programme (GARP) Atlantic Tropical Experiment (GATE; Kuettner et al. 1974) by Houze and Betts (1981) suggests that cyclonic vortices are a frequent if not fundamental characteristic of MCSs in the eastern tropical Atlantic. Tropical MCVs were also observed during the Convection Profonde Tropicale 1981 (COPT 81; Sommeria and Testud 1984) experiment in continental West Africa (Chong et al. 1987; Chong and Hauser 1989, 1990), in the 1987 Taiwan Area Mesoscale Experiment (TAMEX; Kuo and Chen 1990) and the 2008 Terrain-Induced Monsoon Rainfall Experiment (TIMREX; R. Johnson, personal communication) in the vicinity of

Taiwan (Chen and Liang 1992; Jou and Yu 1993; Yu et al. 1999), in the 1988-1990 Down Under Doppler and Electricity Experiment (DUNDEE; Rutledge et al. 1992) and the 2006 Tropical Warm Pool International Cloud Experiment (TWP-ICE; May et al. 2008) in northern Australia (Keenan and Rutledge 1993), and in the 1992-1993 Tropical Ocean Global Atmosphere Coupled Ocean-Atmosphere Response Experiment (TOGA COARE; Webster et al. 1992) in the western tropical Pacific (Chong and Bousquet 1999; Bousquet and Chong 2000). Some studies have appeared in the Chinese and Japanese literature regarding the role of the “southwest vortex” in heavy rain producing MCSs in southern China (Huang 1986, Huang and Xiao 1989); the “southwest vortex” appears to be at least partially generated by the terrain of the Tibetan plateau, but is perhaps enhanced by MCV dynamics (Tao and Ding 1981; Kuo et al. 1986; Ma and Bosart 1987; Wang and Orlanski 1987; Wang 1987; Wang et al. 1993). These findings demonstrate that MCVs are a widespread phenomenon, apparently occurring in all areas that are climatologically susceptible to organised convection in the tropics and subtropics, in addition to the lower mid-latitudes. There have also been a large number of numerical modeling studies of MCVs (e.g., Chen and Dell’Osso 1984; Zhang and Fritsch 1985, 1986, 1987, 1988a,b,c; Dell’Osso and Chen 1986; Kuo et al. 1988; Zhang 1992; Chen and Frank 1993; Weisman et al. 1993; Davis and Weisman 1994; Skamarock et al. 1994; Zhang and Harvey 1995; Zhang and Bao 1996a,b; Weisman and Davis 1998; Trier et al.

2000a; Rogers and Fritsch 2001; Cram et al. 2002; Davis and Trier 2002; Hawblitzel et al. 2007; Conzemius et al. 2007) over the past ~20 years, some of which have been motivated by the possibility of improving warm season quantitative precipitation forecasts (QPF) by successfully resolving and predicting the evolution of MCVs (e.g., see Zhang and Fritsch 1986, 1988c; Hawblitzel et al. 2007).

b. Proposed Formation and Maintenance Mechanisms

Local increases and decreases of cyclonic or anticyclonic relative vorticity are described by the vorticity equation. A number of formation mechanisms for MCVs have been proposed in the literature, based on the various terms in the vorticity equation. These include the concentration of planetary vorticity by stretching or convergence (Bartels and Maddox 1991; Davis and Weisman 1994; Skamarock et al. 1994; Weisman and Davis 1998), the tilting of ambient horizontal relative vorticity (Zhang 1992; Brandes and Ziegler 1993; Chong and Bousquet 1999; Cram et al. 2002), and the convergence of ambient vertical relative vorticity (Brandes 1990; Johnson and Bartels 1992; Bousquet and Chong 2000). Additionally, the reduction of the local Rossby radius of deformation due to the low static stability in the moist stratiform regions of MCSs may be necessary for MCV formation (Chen and Frank 1993; Yu et al. 1999). Recent studies have suggested that MCVs may follow a variety of developmental paths (Kirk 2003, 2007).

Observations generally support the notion that MCVs are warm core (Bartels et al. 1997). In terms of potential vorticity (PV) thinking, MCVs are the balanced response to the increasing latent heating with height associated with the stratiform regions of MCSs (Hertenstein and Schubert 1991; Davis and Trier 2002) (see Figure 1.2). This profile of heating generates a local maximum in PV at the mid levels, which appears to be another distinguishing feature of MCVs (Fritsch et al. 1994). This PV anomaly can interact with vertical wind shear in such a way that the resulting balanced lifting locally favours the regeneration of convection just downshear of the vortex, thereby intensifying the latent heat release and strengthening the vortex (Raymond and Jiang 1990; Jiang and Raymond 1995; Hawblitzel et al. 2007), as well as producing torrential rain (Trier and Davis 2002; Schumacher and Johnson 2008). A recent modeling study by Conzemius et al. (2007) demonstrates that this mechanism is capable of generating and maintaining mid-level PV anomalies in the typical environmental conditions of an MCV. The evolution of the mass and flow fields around MCVs thus appears to be driven by horizontal and vertical gradients of latent heating. Similarly, surface signatures of MCVs must depend on the integrated characteristics of the overlying atmosphere.

The balanced nature of MCVs can allow them to persist for a long time, as long as the deleterious effect of vertical wind shear is minimised in the environment. If the MCV's environment remains otherwise favourable for convection, the MCV can generate

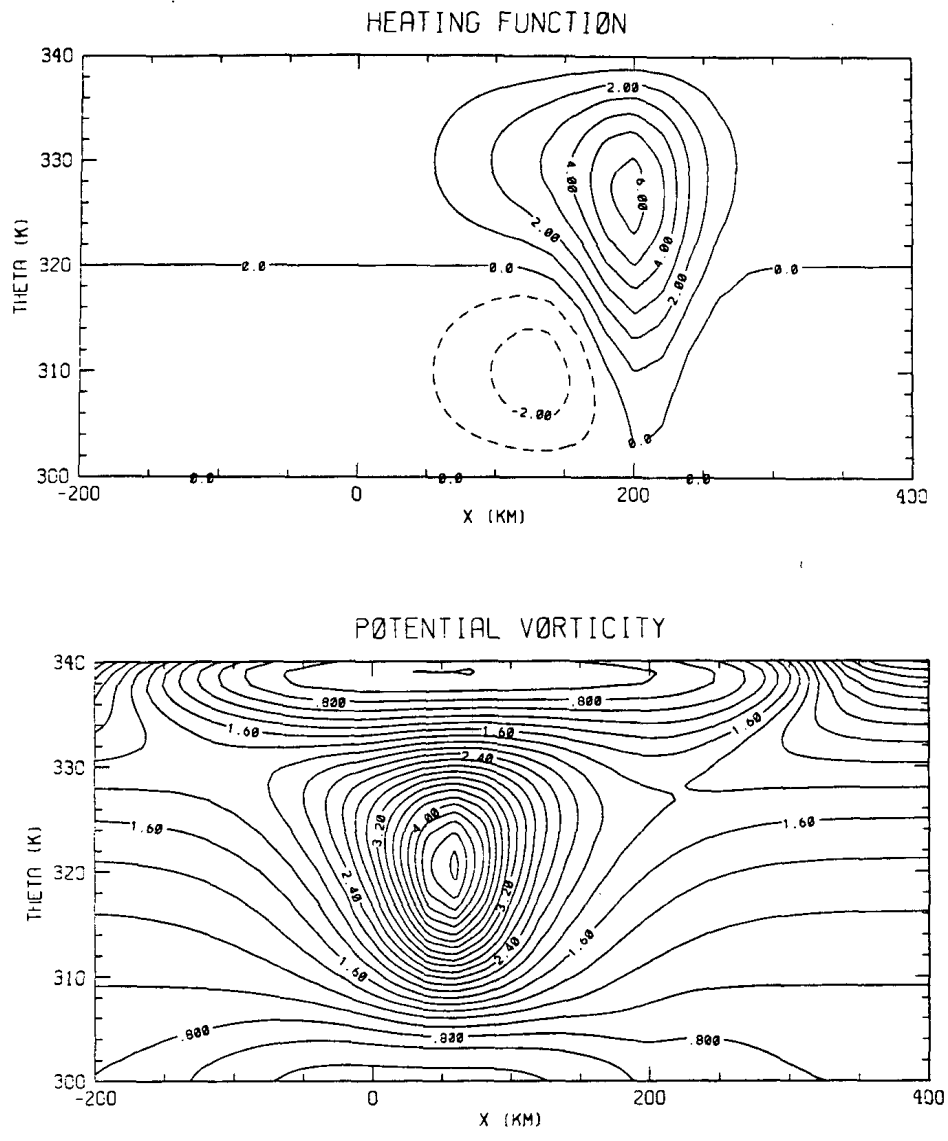


Figure 1.2: (top) Vertical section of heating function (K/h; contour interval 1 K/h, negative heating contours dashed) representing stratiform heating, and (bottom) resulting dimensionless PV distribution (contour interval 0.2) in the wake of this heating propagating from X=0 to X=200 km within semigeostrophic model (from Hertenstein and Schubert 1991).

new MCSs by the above-described mechanism involving the PV anomaly. Each sequential MCS strengthens the vortex by intensifying latent heat release, further

prolonging the MCV life span. This process can continue for several days, as MCSs are generated and dissipate during each diurnal cycle. Convection is generally most vigorous during the nighttime, dissipates in the morning, and regenerates in the late afternoon and evening. One of these so-called serial MCSs, containing an MCV, was responsible for the 19-20 July 1977 Johnstown, Pennsylvania flood (Bosart and Sanders 1981).

c. Previous Studies

There have been several climatological studies of MCVs over the past several decades. Early work by Bartels and Maddox (1991) focused on the synoptic environment of MCVs detected over the United States in eight years of satellite imagery. They found that MCVs are favoured in situations with weak flow, weak vertical wind shear, weak background relative vorticity, and intense vertical and horizontal moisture gradients. Trier et al. (2000b) undertook a climatology of MCVs for one warm season in the central United States, using a variety of observational platforms. They found a relatively large number of long-lived MCVs, which appeared to be favoured under low vertical wind shear. Regeneration of convection occurred in more than half of their identified cases. Davis et al. (2002) investigated MCV detection and prediction using the Rapid Update Cycle (RUC) model. They developed an automated algorithm which is capable of distinguishing MCVs from dynamically different vortex types in hourly RUC analyses,

and demonstrated its ability to detect MCVs over the Great Plains during a warm season. Using this algorithm, they summarised some climatological aspects of midwestern MCVs. It was found that MCVs constitute fewer than half of mid-level mesoscale vortices during the season of interest. They also found that there is a significant positive relationship between MCV intensity and longevity. The RUC appears to be devoid of skill at predicting the development of MCVs in advance.

Upper-air observations of MCVs since the early 1990s have been greatly facilitated by the implementation of the National Oceanic and Atmospheric Administration (NOAA) Profiler Network (NPN) in the midwestern United States. Numerous detailed studies of the kinematic structure of MCVs have been undertaken using these data. Johnson and Bartels (1992) studied an MCV over Oklahoma and Kansas on 23-24 June 1985. They described the vertical structure of the vortex in some detail using a variety of observing platforms, including NPN data. The vortex was 100-200 km in horizontal scale, extending over 3-8 km altitude, with maximum relative vorticity near the melting layer. In general the MCV was warm core, with the most significant warm anomaly at low levels, associated with a descending inflow jet. Bartels et al. (1997) examined an MCV over northeastern Colorado on 8 June 1988, finding values of mid-level relative vorticity greater than three times the local Coriolis parameter. They used gradient wind balance to derive a balanced temperature field associated with

the MCV, which implied a warm core over cold core thermodynamic structure. Knievel and Johnson (2002) used wind profiler data to derive the synoptic and mesoscale flow features associated with an MCV observed in Oklahoma and Kansas on 1 August 1996. This MCV grew to a depth of 12 km. They recorded the presence of a mesoscale updraught and a mesoscale downdraught, as well as upper- and low-level divergent outflow. In a subsequent study (Knievel and Johnson 2003), the authors constructed a scale-discriminating relative vorticity budget for this MCV, finding that the MCV deepened and strengthened during the dissipation of the parent MCS due to convergence of absolute vorticity by the mesoscale wind. A final investigation of this case (Knievel et al. 2004) sought to determine the extent of hydrostatic and gradient wind balance in the MCV, finding that the MCV was at least partially unbalanced.

Two more recent studies have been based on observations from the Bow Echo and Mesoscale Convective Vortex Experiment (BAMEX) of 2003 (Davis et al. 2004). This experiment is so far the only field programme designed specifically to observe MCVs. It focussed on upper-air observations from dropsondes, wind profilers, and aircraft, rather than on dense surface observations, so most studies stemming from this experiment have likewise dealt with the upper-level characteristics of MCVs. Trier and Davis (2007) and Davis and Trier (2007) summarised some initial results from five BAMEX intensive observing periods (IOPs) focusing on MCVs. They described a very

wide variety of structures among the mature vortices examined. In general the MCVs were observed to arise from the stratiform precipitation regions of MCSs. They were 5-8 km deep, attaining their maximum relative vorticity between 600 and 550 hPa. The MCVs had varying degrees of tilt with the environmental shear; one case they examined appeared to be resilient and resisted tilting in shear. Vortex penetration into the boundary layer appeared to require weak low-level wind shear. They also found that, on average, outbreaks of secondary convection are favoured in the downshear right quadrant of MCVs, due to a favourable kinematic and thermodynamic environment.

There have been abundant studies examining the surface features of MCSs and general convection over the past 70 years. Specific subjects have included the hydrostatically-induced mesohigh beneath the convection (e.g., Sawyer 1946; Schaffer 1947; Williams 1948, 1953; Fujita 1951, 1955, 1959; Brunk 1953; Purdom 1973; Fankhauser 1974), the density current-like gust front at the leading edge of the mesohigh (e.g., Freeman 1950; Newton 1950; Tepper 1950, 1955; Charba 1974; Goff 1976; Miller and Betts 1977; Wakimoto 1982; Roux et al. 1982, 1984; Mueller and Carbone 1987; Nicholls et al. 1988), the pre-squall mesolow induced by subsidence warming aloft ahead of the active convection (Feteris 1961, 1978; Hoxit et al. 1976, 1977; Sanders 1977; Fritsch and Chappell 1980a,b), the wake low induced by subsidence warming within a descending rear inflow jet (Brunk 1949; Williams 1954; Magor 1958; Charba and Sasaki

1971; Menard et al. 1988; Gallus 1996; Wicker and Skamarock 1996; Johnson 2001), surface flow through these pressure features (Garratt and Physick 1983; Vescio and Johnson 1992), the “squall wake” due to a shallow layer of cool, moist convective outflow behind the active convection (Zipser 1977; Johnson and Nicholls 1983), pressure responses to gravity waves (Haertel and Johnson 1998, 2000), transitory pressure features (Kniewel and Johnson 1998), and non-hydrostatic effects (Levine 1942; Mal and Rao 1945; Marwitz 1972). However, to date there have been relatively few studies investigating the particular surface features that accompany MCVs. This may be partly due to the lack of sufficiently dense surface observing networks, or the paucity of field programmes designed to observe MCVs.

The Oklahoma-Kansas Preliminary Regional Experiment for Storm-Scale Operational and Research Meteorology (OK PRE-STORM; Cuning 1986) provided the first high resolution surface observations of MCSs and their associated MCVs in the summer of 1985, motivating numerous studies of the surface features of MCSs (Johnson and Hamilton 1988; Johnson and Gallus 1988; Zhang et al. 1989; Zhang and Gao 1989; Smull and Jorgensen 1990; Stumpf et al. 1991; Smull et al. 1991; Nachamkin et al. 1994; Loehrer and Johnson 1995), and several studies specifically addressing surface features of MCVs. An investigation of the 23-24 June 1985 OK PRE-STORM MCS by Johnson et al. (1989) found several interesting surface features associated with the decay of the

MCS and the development of a mid-level circulation. There was a strong mesohigh situated beneath the stratiform rain portion of the MCS during the system's mature phase. As the stratiform rain degenerated, this mesohigh transformed into a strong mesolow (see Figure 1.3). This transformation was coincident with the development of a well-defined cyclonic vortex, visible in satellite imagery. The authors proposed that the mesolow formed from hydrostatic effects due to warming and drying within a region of strong mesoscale subsidence in the absence of any precipitation; this warm subsiding air actually produced localised “heat bursts” at several mesonet sites (Bernstein and Johnson 1994). It was unclear if there was any connection between the mesolow and the MCV development. The existence of unsaturated downdraughts driven by rainfall evaporation has been demonstrated in a well-known modeling study (Brown 1979), and is understood to be the mechanism for both microbursts (Fujita and Wakimoto 1981; Brown et al. 1982; McNulty 1991) and heat bursts (Johnson 1983). Brandes (1990) and Brandes and Ziegler (1993) studied the 6-7 May 1985 OK PRE-STORM MCS and its associated MCV. They found that the MCV focused and intensified a descending rear inflow jet into the southern portion of the system. This descending air current apparently led to strong low-level subsidence warming and drying, producing a mesolow with a perturbation pressure anomaly of -4 hPa (see Figure 1.4). Again, it is unknown to what extent the MCV was responsible for the production of this mesolow. They also found

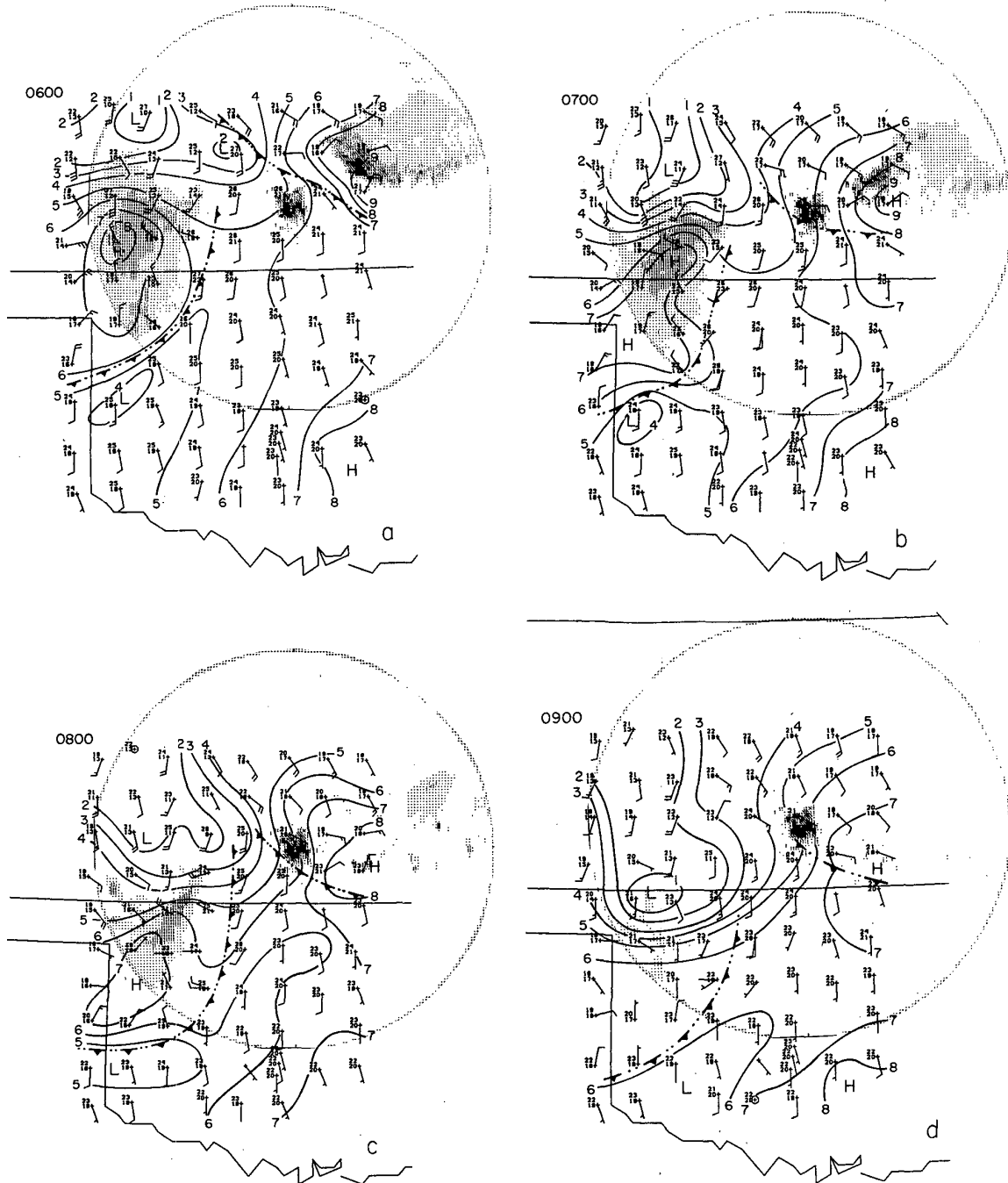


Figure 1.3: Surface pressure analyses (hPa; contour interval 1 hPa) of OK PRE-STORM mesonet network at (top left) 0600, (top right) 0700, (bottom left) 0800, and (bottom right) 0900 UTC on 24 June 1985. Pressure is adjusted to 518 m, given as departure from 950 hPa. Hatched regions represent precipitation (from Johnson et al. 1989).

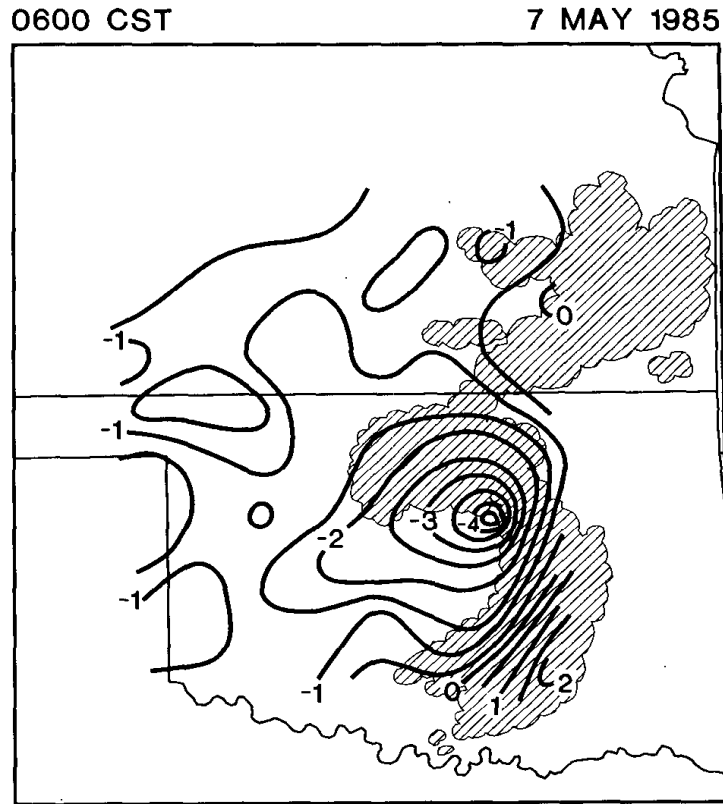


Figure 1.4: Surface pressure analysis (hPa; contour interval 0.5 hPa) of OK PRE-STORM mesonet network at 0600 CST on 7 May 1985. Pressure is given as departure from 24-h mean. Hatched regions represent precipitation (from Brandes 1990).

that the MCV was amplified by convergence into the mesoscale downdraught associated with the MCS.

A rear inflow jet was also documented in connection with a tropical MCV by Chong and Bousquet (1999) and Bousquet and Chong (2000). While rear inflow jets do commonly appear in MCVs, and likely enhance the convergence and relative vorticity within MCVs, it has been shown that they can be generated by microphysical processes

unrelated to MCV dynamics (Braun and Houze 1997). The rear inflow mechanism for mesolow generation consists of concentrated descent within the inflow being forced by evaporational cooling-induced subsidence at the rear of the stratiform region, which eventually becomes unsaturated and warms adiabatically, hydrostatically forming a wake low (Johnson and Hamilton 1988; Stumpf et al. 1991). A modeling study by Gallus (1996) suggests that this mechanism will only form a mesolow if the evaporating rainfall is decreasing in intensity, as occurs during the dissipation stage of an MCS; only under this condition will the adiabatic warming due to subsidence outweigh the cooling due to the evaporation of the precipitation. A study by Fortune et al. (1992) addressed the tendency for MCSs to evolve in a manner resembling the frontal-wave pattern observed in synoptic-scale extratropical cyclones, using data collected in four OK PRE-STORM MCSs. They found indications that this pattern is not related to the development of cyclonic mesoscale relative vorticity. Their mesoanalyses of the MCSs revealed fairly well-defined mesohighs and mesolows; however, these MCSs did not appear to contain well-defined MCVs.

d. The Tropical Cyclogenesis Problem

The specific mechanisms involved in the process of tropical cyclogenesis remain elusive despite much focused research. Some notable similarities between tropical

cyclones and MCVs suggest that MCVs may be a necessary ingredient in incipient tropical cyclones (Zhang and Fritsch 1987; Keenan and Rutledge 1993; Fritsch et al. 1994; Ritchie et al. 1995; Zhang and Bao 1996a,b; Harr et al. 1996a,b; Simpson et al. 1997; Davis et al. 2004). Two main tropical cyclogenesis hypotheses have been proposed recently, both of which may be active in different cyclogenesis cases. One theory is that an initially mid-level vortex, consisting of a PV maximum above a low-level cold pool, can gradually build downward toward the surface through strengthening and deepening of the PV maximum by repeated MCS generation and dissipation (Fritsch et al. 1994; Rogers and Fritsch 2001; Trier and Davis 2002). Such a transformation likely also requires significant sensible and latent heat fluxes from the ocean surface, which may explain the rarity of sustained convectively-induced mesolows over land and over cool (< 26 °C) waters. In an extension of this theory, Mapes and Houze (1995) propose that several anomalous characteristics of divergence profiles within tropical MCSs would favour downward development of an initially elevated cyclonic circulation. They present evidence, from the TOGA COARE MCS of 6 February 1992, of low- to mid-level divergence and near-surface convergence, as well as adiabatic subsidence, all of which would act to lower the relative vorticity maximum and destroy the low-level cold pool. The other cyclogenesis hypothesis is that low-level PV generation by developing convection in the form of vortical hot towers spins up the vortex, with an MCV providing

a favourable environment with weak background cyclonic relative vorticity (Montgomery and Enagonio 1998; Reasor et al. 2005). Several studies have used numerical modeling to explicitly investigate the role of observed mid-level mesovortices during the genesis stage of tropical cyclones (Ritchie and Holland 1997; Bister and Emanuel 1997; Montgomery and Enagonio 1998; Kieu and Zhang 2008). It remains unclear which hypothesis is more realistic, but MCVs may play a key role in the tropical cyclogenesis process.

There have been a number of documented cases of tropical cyclones developing from MCSs moving offshore. The Johnstown MCV, in July 1977, actually intensified to tropical storm strength after emerging off the coast into the Atlantic (Bosart and Sanders 1981). This tropical cyclogenesis was confirmed in more recent model simulations by Zhang and Bao (1996a,b). Another interesting case was observed during the recent TWP-ICE campaign in tropical Australia. A large MCS formed as the monsoon trough retreated northward away from Australia in late January 2006, and clear cyclonic rotation was observed in the cloud field as the MCS emerged over water. The system deepened to 999 hPa as it made landfall southwest of Darwin, and continued to intensify to 988 hPa over land, maintaining its convection and spiral cloud structure for two days (May et al. 2008). Other systems similar to this have been observed over northern Australia, and are locally known as “landphoons”. Emanuel et al. (2008) have proposed that these cyclones

are maintained by strong vertical heat fluxes from the underlying hot desert soil which has been moistened by the first rains of the approaching system. Climatological studies of global MCC populations in the Americas (Velasco and Fritsch 1987), the western Pacific (Miller and Fritsch 1991), southern Asia (Laing and Fritsch 1993a), and Africa (Laing and Fritsch 1993b) have found numerous cases of tropical cyclones developing from MCCs, presumably due to the presence of embedded MCVs.

While true tropical cyclogenesis is only possible over warm water, there have been several observed cases of significant MCV-induced surface mesolows over land, as summarised above. Zhang and Harvey (1995) describe a real-case simulation demonstrating enhancement of extratropical cyclogenesis by a convectively-generated mesovortex. Rogers and Fritsch (2001) describe another real-case simulation in which a pronounced mesolow forms beneath an MCV over land after three cycles of convective redevelopment. Since surface observations are very sparse over the oceans in regions of frequent tropical cyclogenesis, surface observations over land beneath MCVs may be the best source of observational evidence to support one of the theories of cyclogenesis.

e. Objectives

The goal of this study is to provide a broad climatological overview of the structure and evolution of midlatitude MCVs by using relatively dense surface and upper-

air observations of a large number of MCVs occurring during the late spring and summer months of four years over the state of Oklahoma. It is hoped that such a climatology will facilitate generalisations about the physical characteristics of MCVs which will help to synthesise and solidify the conclusions reached in the large number of individual MCV case studies summarised above. It is also anticipated that the large population of MCVs investigated herein will provide a statistically robust basis for validation of numerical simulations of MCVs, from both the numerical weather prediction (NWP) and general circulation modeling (GCM) perspectives. An additional important objective is the documentation of MCV penetration to the surface and the proposal of some mechanisms for this phenomenon, which may be active in the tropical cyclogenesis process.

The remainder of this paper is organised as follows. The data sources used, and their strengths and weaknesses, are described in section 2. Section 3 describes the methodology followed for selecting and analysing the individual MCV cases, and constructing the various composites. Results are presented in sections 4 and 5, and are discussed in section 6. Section 7 contains the conclusions of the study.

II. DATA SOURCES

A variety of observational and model datasets are used in this study. Model data are used in the detection of MCV cases, and to provide a synoptic-scale context for the analysis of each case. Observational data are used to investigate the mesoscale structure of the MCVs in more detail. This section provides descriptions of the various datasets used in this study, and highlights potential quality problems unique to each dataset.

a. The Rapid Update Cycle

The RUC (Benjamin et al. 2004) is a high-resolution model analysis and forecasting system designed to aid in short-term operational forecasting of hazardous weather situations. The RUC system is an assimilation-forecast cycle: thus, each new analysis is based on a background field derived from the model's earlier forecast for that time. The horizontal and vertical grid spacing of the model have been upgraded several times; the current operational version of the model has a horizontal grid spacing of 20 km and 50 vertical levels. In addition to the standard synoptic observations, the RUC assimilates a wide variety of asynoptic data types to improve the quality of its hourly analyses (see Figure 2.1). Two of the most important asynoptic data sources for the RUC

Data type	~ Number	Frequency
Rawinsonde (including special obs)	80	/12 h
NOAA 405-MHz profiler wind	31	/ 1 h
Boundary layer (915 MHz) profiler wind ^d	24	/ 1 h
RASS virtual temperatures ^d	10	/ 1 h
VAD winds (WSR-88Ds) ^a	110–130	/ 1 h
Aircraft (ACARS) ^b (wind, temperature)	1400–4500	/ 1 h
Surface/METAR—land (V , p_{fc} , T , T_d)	1500–1700	/ 1 h
Surface/Mesonet—land ^d	2500–4000	/ 1 h
Buoy	100–150	/ 1 h
GOES precipitable water	1500–3000	/ 1 h
GOES cloud-drift winds	1000–2500	/ 1 h
GOES cloud-top pressure/temperature	~10 km resolution	/ 1 h
SSM/I ^c precipitable water	1000–4000	/ 6 h
GPS precipitable water ^d	200	/ 1 h
Ship reports	5–40	/ 3 h
Reconnaissance dropwindsonde	0–10	/variable

^a Weather Surveillance Radar-1988 Doppler.

^b Aircraft Communications, Addressing, and Reporting System.

^c Special Sensor Microwave Imager.

^d At FSL only as of Oct 2003.

Figure 2.1: Observational data assimilated into the operational RUC model as of spring 2003 (from Benjamin et al. 2004).

are NPN wind profiles and Aircraft Communication Addressing and Reporting System (ACARS) reports from commercial aircraft. These data sources, consisting of numerous additional vertical wind profiles of the atmosphere, are critical for identifying MCVs, and represent a great improvement upon the twice-daily and very sparse national radiosonde network. The success of MCV detection by the RUC analysis has been demonstrated by Davis et al. (2002). While model representations of MCVs may be unrealistic, this method of detection avoids the necessity of scanning through days of radar or satellite data looking for potential MCVs, and is consistent throughout all times. The Davis et al. (2002) algorithm (see section 3a for more details) detects MCVs based on consideration of the RUC gridded hourly analysis winds at 600, 550 and 500 hPa (covering the pressure levels where MCVs are typically strongest). Data for this algorithm are obtained from

the NOAA National Operational Model Archive and Distribution System, and consist of zonal and meridional wind data at these three levels over the late spring and summer (May-August) of the years 2002-2005, over the entire RUC domain (the continental USA and immediate surroundings). The operational version of the RUC during these four years, the RUC-236, had a horizontal grid spacing of 40 km. The years examined have a varying amount of missing data. The 2002 data are 39% complete, 2003 is 87% complete, 2004 is 91% complete, and 2005 is 38% complete. It is likely that numerous MCVs were not detected in 2002 and 2005, but this will not affect the conclusions drawn about the successfully detected systems. For each of the MCV cases analysed in this study, the full RUC data (all variables and all levels) are obtained in order to perform a more detailed analysis of each case. The vertical spacing of the RUC-236 data is 50 hPa, from 1000 to 100 hPa. Variables retrieved include surface-based convective available potential energy (CAPE) and convective inhibition (CIN); column-integrated precipitable water; 2-m temperature, pressure, mean sea level pressure, and relative humidity; 10-m zonal and meridional wind speed; and pressure-level geopotential height, temperature, relative humidity, pressure vertical velocity, and zonal and meridional wind speed. The pressure vertical velocity variable in the RUC is only available at certain pressure levels (850, 700, 500, 300, and 200 hPa), and the relative humidity variable is only available every 50 hPa at and below 500 hPa. A variety of other variables are derived from the

RUC variables, including vapour pressure, saturation vapour pressure, mixing ratio, saturation mixing ratio, dewpoint temperature, divergence, relative vorticity, potential temperature, equivalent potential temperature, and absolute vorticity at 2 m and at constant pressure levels, as well as PV at constant pressure levels. RUC data are missing or incomplete for all times of the 3 June 2002, 4-5 June 2002, and 9-10 June 2002 cases, and for 11 hours of the 20 June 2004 case, four hours of the 3 June 2003 case, three hours of the 24-25 June 2003 case, two hours of the 19 June 2004 case, and one hour of the 10 June 2005 case.

While model fields are very convenient and attractive due to their completeness and their organisation on a regular grid, all models have major shortcomings. It was found by Davis et al. (2002) that the RUC has virtually no skill in predicting the formation of MCVs 12 h in advance. This is likely due to the inherent unpredictable nature of the convection which produces MCVs. While this study does not make use of any RUC forecasts, the design of the RUC model as an assimilation-forecast cycle implies that RUC forecasts do have an influence on the hourly analyses. Thus, unrealistic model physics may negatively impact the analysis representations of MCVs. This problem can be exacerbated by sparse observations being ingested into the RUC. If there happen to be no useful asynoptic data available for assimilation at a particular time, the background field derived from the RUC forecast will be almost unmodified to

produce the final 0-h analysis. In extreme situations (such as a lack of any new analysis data), the RUC analyses can progressively become farther and farther from reality with each hour that passes. Another problem associated with the RUC analyses is aliasing associated with time windows for observations. The asynoptic observations assimilated into the RUC are generally not valid at exactly the same time as the analysis time; thus, some error is introduced into the analysis by allowing a finite window of time in which observations will be incorporated. Finally, the RUC analyses can suffer simply from the relatively coarse resolution of the model grid; 40 km may be insufficient to resolve features on the small side of the mesoscale. Due to these inherent deficiencies with the RUC analyses, these data are only used to describe the synoptic-scale environment of MCVs. Conclusions drawn about the mesoscale structure of MCVs based on RUC analyses should be treated with caution.

b. The NOAA Profiler Network

The primary upper-air observations used in this study are taken from the NPN (Weber et al. 1990). The NPN is a network of 404-MHz (74.3-cm wavelength) radar wind profilers concentrated in the midwestern USA (see Figure 2.2). The profilers operate with three upward pointing beams directed by a large, fixed, phased-array antenna: one vertical beam, one pointing north at 73.7° elevation angle, and one pointing

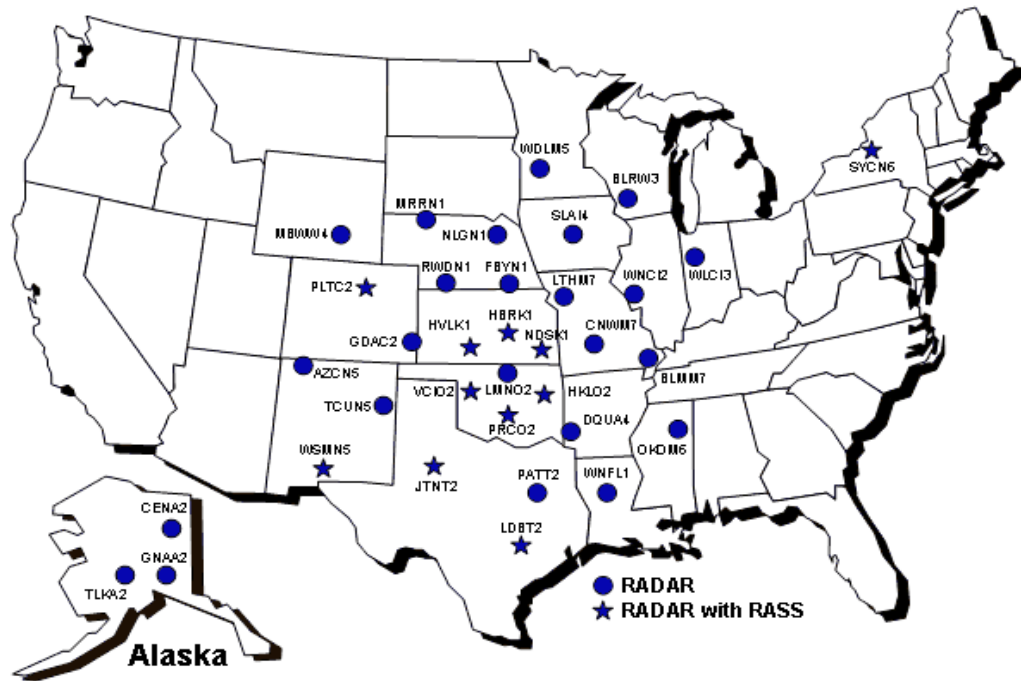


Figure 2.2: NPN site map. Data used in this study are taken from Dequeen, Arkansas (DQUA4); Haskell, Oklahoma (HKLO2); Haviland, Kansas (HVLK1); Jayton, Texas (JTNT2); Lamont, Oklahoma (LMNO2); Neodesha, Kansas (NDSK1); Purcell, Oklahoma (PRCO2); and Vici, Oklahoma (VCIO2).

east at 73.7° elevation angle. The profilers have a vertical gate spacing of 250 m, covering the altitude range from 500 m to 16.25 km above ground level. The data used in this study are hourly wind profiles, consisting of averages of sub-hourly (6-minute) observations. Horizontal winds are derived from raw radial velocities by simple trigonometry, after determining the vertical velocity from the vertically pointing beam and then subtracting the component of this along the off-vertical beams. Limited thermodynamic profiles can also be obtained from some of the NPN sites. The Radio

Acoustic Sounding System (RASS; North et al. 1973) technique makes use of the fact that air compression and rarefaction by sound waves alters the dielectric constant of the medium, causing a partial reflection of electromagnetic energy from a radar. An acoustic source sends out a sound wave into the atmosphere, which can then be tracked by the radar. The speed of the sound wave can be related to the virtual temperature of the layer through which the wave passes; thus it is possible to derive a virtual temperature profile of the lower atmosphere. A major advantage of RASS is its high temporal sampling; it is possible to continuously monitor the virtual temperature profile. Hourly profiler data are obtained for each MCV case from the NOAA NPN online archive. Wind profiles from the following profiler sites are obtained: Dequeen, Arkansas; Haskell, Oklahoma; Haviland, Kansas; Jayton, Texas; Lamont, Oklahoma; Purcell, Oklahoma; Neodesha, Kansas; and Vici, Oklahoma. RASS equipment is installed at all eight of these profiler sites except Dequeen, Arkansas, and Lamont, Oklahoma. Table 2.1 lists the MCV cases for which some profiler data were missing, and the number of missing hours at each profiler site during these cases.

Wind profiler data quality can become an issue under certain conditions. Specifically, convective precipitation (Wuertz et al. 1988) and gravity waves (Nastrom and Vanzandt 1996) can violate the fundamental horizontal homogeneity assumption (beam spacing is several kilometres at high altitudes), and migrating songbirds can cause

<i>Case</i>	<i>Missing NPN Observations</i>
17 May 2002	Dequeen (6), Vici (1)
9-10 June 2002	Lamont (6)
24 August 2002	Haviland (14)
27 August 2002	Haskell (16), Purcell (3), Vici (2)
21 May 2003	Neodesha (11)
24-25 May 2003	Jayton (14), Lamont (1)
3 June 2003	Jayton (1)
12 June 2003	Purcell (17), Jayton (2)
21 June 2003	Jayton (3)
3-4 June 2004	Dequeen (8)
6-8 June 2004	Lamont (24)
20-21 June 2004	Neodesha (2)
1-2 July 2004	Haviland (2)
5 July 2004	Neodesha (2)
28 July 2004	Jayton (1)
29 July 2004	Dequeen (1)
11-12 August 2004	Lamont (8)
20-21 August 2004	Dequeen (5)
10 June 2005	Haviland (11)
17 June 2005	Vici (14), Dequeen (13), Purcell (1)
1-2 July 2005	Neodesha (8), Vici (2)

Table 2.1: Missing observations from the NPN during MCV cases examined in this study. Numbers in parentheses indicate the number of missing hours at the specified site for each listed case.

unrealistic wind speeds and directions in low-level profiler observations in the early morning during the migration season (spring or autumn) (Wilczak et al. 1995). This study uses only data passing a bird contamination check (Wilczak et al. 1995) and a time-height continuity check (Weber et al. 1993), so these problems should not affect the results of this study. Errors in the RASS measurement of virtual temperature can be introduced by the presence of vertical velocity, or by an inaccurate measurement of the sound pulse velocity (particularly at low signal-to-noise ratios, which can occur at long range). All RASS data used in this study have passed the time-height continuity check (Weber et al. 1993). However, through manual inspection of the data, it became clear that some quality issues remained. Specifically, the RASS temperature profiles occasionally contained layers of varying thickness with unrealistically and uniformly high virtual temperatures. In the most extreme cases, the profiles consisted of near 40 °C virtual temperatures at all range gates between the surface and 500 hPa. Fortunately, these erroneous temperatures are easily detectable by an automated process. The Fortran-77 programme written to analyse the profiler data thus includes a simple quality control check consisting of a range of allowed virtual temperatures at each height. Data falling below the minimum allowed virtual temperature or above the maximum allowed virtual temperature at each height are changed to missing data. The allowable virtual temperature range is 20 °C at each height, centred on realistic values for the summer

season in Oklahoma. This simple algorithm appears to have removed erroneous data from consideration.

c. The Oklahoma Mesonet

Mesoscale surface observations in this study consist of data from the Oklahoma Mesonet (McPherson et al. 2007). This network of high-quality automated surface weather stations is made up of 127 sites distributed around the state (see Figure 2.3). The mesonet was established in 1994, and its data have been used in a variety of applications including public safety, emergency management, education, resource management, agriculture, industry, and research. Data are recorded every five minutes, resulting in a very high spatial and temporal resolution representation of the state of the environment. Strict standardisation of the station siting and instrumentation, as well as extensive quality control, ensure high data quality. A large number of variables are measured; the relevant variables for this study are 1.5-m air temperature and relative humidity, surface rainfall, surface pressure, and 10-m wind speed, wind direction, and wind gusts. Historically, there have been very few high-quality surface mesonets, despite their demonstrated importance in improving our understanding of MCSs and their governing dynamics. Prior to the establishment of the Oklahoma Mesonet, most mesonets were associated with specific field campaigns (such as OK PRE-STORM), and

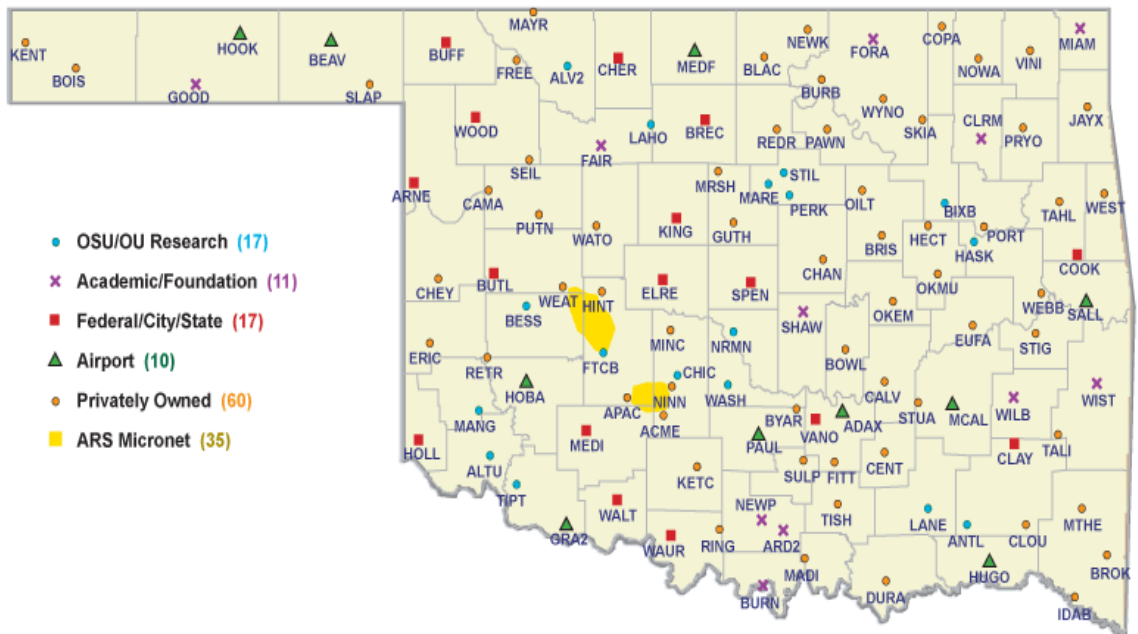


Figure 2.3: Oklahoma Mesonet site map.

only lasted for a few months at most. The Oklahoma Mesonet now provides continuous data, facilitating further studies, and new advances in our understanding of the dynamics of plains convection (Johnson et al. 1996).

Due to the extensive quality control procedures implemented by the Oklahoma Climatological Survey, it was not anticipated that there would be many data quality problems. All instruments installed at mesonet sites are calibrated by mesonet staff prior to deployment. Mesonet sites are visited by a technician for maintenance and on-site calibration at least three times per year. Automated quality control procedures include an initial quality filter (which flags data falling outside the variable range), independent

algorithms (including step, persistence, and spatial tests), and a quality decision maker algorithm (which assigns a final flag to the observation). Manual quality control is also implemented. The data used in this study, from May through August of the years 2002-2005, appear to have no quality problems. One or two sites are sometimes missing data, but this in no way affects the overall mesoanalyses contained herein.

d. The Next Generation Weather Radar Network

One of the primary data sources for investigating the evolution of MCSs and their MCVs in this study is the Next Generation Weather Radar (NEXRAD) network of Weather Surveillance Radars 1988-Doppler (WSR-88Ds). This national network of Doppler radar installations provides complete coverage of the state of Oklahoma. The individual radars operate at 10 cm wavelength, and are optimised for observing precipitation. Therefore they are a powerful tool for observing the development, movement, and evolution of precipitation systems such as MCSs. For this study, NEXRAD Level 3 data are obtained for each MCV case in order to provide a background field for subsequent analysis. Reflectivity composite images (the maximum reflectivity observed at any level at each gridpoint) are obtained at 15-minute intervals during each case from WSI Corporation. Level 3 reflectivity data are also obtained for individual Oklahoma radar sites in order to track the heading and speed of the MCVs. The specific

radar sites used are Frederick, Oklahoma (FDR); Inola, Oklahoma (INX); Fort Smith, Arkansas (SRX); Twin Lakes, Oklahoma (TLX); and Vance Air Force Base, Oklahoma (VNX). These data are retrieved from the National Climatic Data Center (NCDC).

Radar observation in meteorology has a long history, and many potential quality issues have been highlighted by both the research and the operational communities in the past several decades. Many of these problems are associated with the observation of the Doppler velocity. The WSR-88Ds' Doppler capability allows determination of the radial velocity of meteorological targets; this information is not used in this study. Rather, this study utilises the most basic radar-observed quantity: the radar reflectivity. Radar reflectivity within a distribution of meteorological targets depends upon a variety of factors, including characteristics of both the radar and the contents of the target volume. The radar reflectivity is proportional to the diameter of the scatterers to the sixth power, and thus is highly sensitive to large scatterers. 10-cm, or S-band, radars are sensitive to precipitation-sized particles (typically several mm in diameter), so the NEXRAD reflectivity data are a proxy for precipitation intensity. In some instances, the reflectivity measurement can be affected by the presence of ice (including snow, graupel, ice pellets, and hail) but in the warm season this effect is usually fairly minor. Radar reflectivity can also be contaminated by antenna sidelobes, as well as by ground clutter; these issues are largely resolved by operational algorithms. In this study, the radar reflectivity is used

only in a qualitative sense, to distinguish between the stratiform and convective regions of MCSs and to determine the relative intensities of areas of convection.

e. Miscellaneous Data

Several other data sources are used in the analysis of MCV cases. The primary source of information concerning the synoptic-scale context for each case is the standard operational radiosonde network. This network, which covers the continental USA with a reasonable station spacing (~70 stations), gives a broad overview of the upper-level flow patterns within which MCVs are situated. Soundings are launched twice daily, at synoptic times 0000 and 1200 universal coordinated time (UTC). The individual soundings from Norman, Oklahoma, and surrounding sites are occasionally examined in more detail when they were taken in the immediate vicinity of passing MCVs. Individual soundings, as well as upper-air analyses produced by the NOAA Storm Prediction Center (SPC), are accessed through the National Center for Atmospheric Research (NCAR) Mesoscale and Microscale Modeling (MMM) Division's online image archive.

Satellite imagery from the Geostationary Operational Environmental Satellite (GOES) platforms covering the eastern and western portions of the country is used to ascertain the extent and type of cloud cover associated with the MCVs. During the daytime, visible imagery is examined, and during nighttime, infrared (IR) imagery is

used. Knowledge of the presence and type of cloud cover in different regions of MCVs is helpful in determining possible dynamics of some observed surface features. Satellite imagery is also obtained through MMM's online image archive.

The Department of Energy (DOE) Atmospheric Radiation Measurement (ARM) programme runs a permanent observing facility in north-central Oklahoma: the Southern Great Plains (SGP) Cloud and Radiation Testbed (CART) site. In addition to a variety of cloud remote sensors and surface observing instruments, the site is equipped with a radiosonde launcher, and soundings are launched every six hours (more frequently during special observing periods). Each available sounding taken from this site (near Lamont, Oklahoma) during the passage of an MCV through Oklahoma is obtained from the ARM data archive. These supplemental soundings provide valuable additional upper-air kinematic and thermodynamic information.

III. METHODOLOGY

This section provides details of the methodology used in the selection and analysis of individual MCV cases, as well as in the construction of MCV composites. Case analyses and compositing are carried out using both observational and model-based (RUC) data.

a. Case Selection

To facilitate generalisations about the structure and dynamics of MCVs, it is important to obtain a large number of MCV cases to examine in detail. Several possible detection methods have been proposed in the literature in the past few decades. The subjective method of Bartels and Maddox (1991) involves searching 4-km visible satellite imagery for systems which exhibit well-defined cloud bands for more than one hour, whose “shape and pattern suggest cyclonic rotation, even when viewed on a single satellite image”. This method, applied by Bartels and Maddox (1991) to approximately eight years of satellite imagery over the central USA, appeared to significantly underestimate the total number of MCVs occurring. This is likely due to the limitations of the satellite imagery; MCVs were only detected if they had well-defined cyclonic

curvature in the mid- and low-level clouds, with limited obstructing upper-level cirrus. They found 24 events over an eight-year period. A more recent study by Trier et al. (2000b) used a larger variety of observational platforms in their MCV detection, including radar reflectivity, IR satellite imagery, and NPN wind profiles. They considered an MCV to exist whenever a circulation was indicated by any of these platforms after the dissipation of convection associated with the parent MCS. Using this method, Trier et al. (2000b) detected 16 MCVs during the warm season of 1998. A third MCV detection methodology, involving analyses from the RUC model, was developed by Davis et al. (2002). Their algorithm, which requires relative vorticity maxima to pass a variety of tests in order to be considered MCVs, provides an objective means of MCV detection. While this method is based on model data, and thus may be occasionally inaccurate, it is consistent among all times, and can be automated, thus reducing the time required for finding cases. Based on these advantages, and the limitations associated with the earlier two methods, the Davis et al. (2002) algorithm is used to detect MCVs in this study.

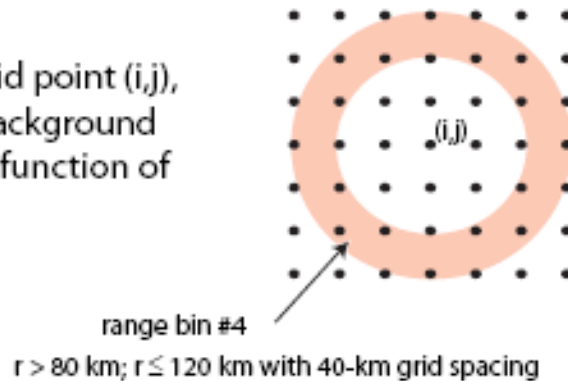
The Davis et al. (2002) algorithm detects MCV within a gridded field of vertical relative vorticity (Figure 3.1). In order to focus on MCVs, which are typically most intense in the mid-troposphere, the relative vorticity input to the algorithm is calculated (using centred-differencing) from the gridded wind field at each level between 600 and

Detecting MCVs in gridded vorticity field

Search 600-500 mb layer.

Find round vertical vorticity maxima 100 to 600 km wide.

For each grid point (i,j) ,
calculate background
vorticity as function of
range (r) .



For center point to qualify as MCV, background vorticity must:

- decrease monotonically with range
- decrease 90% within 50-300 km range
- not vary much within any range bin (roundness test)

Roundness test:

To ensure roundness, the standard deviation may not vary significantly with azimuth. If the standard deviation (normalized by the center vorticity) exceeds 0.3 within any range bin, the center point is disqualified.

Figure 3.1: Description of MCV detection algorithm developed by Davis et al. (2002).

500 hPa, and then averaged over that layer. The first step in the algorithm is the identification of relative vorticity maxima, defined as gridpoints where the Laplacian of the relative vorticity is negative. The next step filters out horizontally elongated vorticity features, which are quite common but non-convective in origin. To do this, the algorithm calculates several metrics associated with the radial distribution of relative vorticity around each vorticity maximum. The radial distribution of relative vorticity is determined by taking the azimuthal mean of all the gridpoints within a series of increasingly distant range bins of radial width 40 km (equal to the spacing of the RUC grid). The radius R of the vortex is defined as the radius bin annulus in which the azimuthal mean relative vorticity decreases to less than 10% of its maximum (central) value. For each radius bin within R , the standard deviation of relative vorticity about the azimuthal mean relative vorticity is calculated. Horizontally elongated features are removed by excluding all vortices whose relative vorticity standard deviation (in any range bin) is above 30% of the maximum (central) relative vorticity. The algorithm also requires that the azimuthal mean relative vorticity decrease monotonically out to radius R , which excludes vorticity lobes attached to larger-scale maxima. The radial distribution of relative vorticity is only determined out to seven range bins. The seventh range bin corresponds to an average radius of 262 km; thus, larger vortices are not detected by the algorithm. This filters out synoptic-scale vorticity anomalies, and keeps

the focus on the mesoscale. The original algorithm was written in Fortran 77; the algorithm used in this study was developed in Matlab, based on the original algorithm provided by David Ahijevych. The presence of numerous times in the RUC data when at least one of the three pressure levels was missing prompted a modification of the algorithm to search for MCVs based on only one or two levels. The final algorithm is run on the available gridded wind fields for the months of May through August of 2002-2005, over the entire RUC domain. For the purposes of this study, output is only examined over the central USA, particularly in the vicinity of Oklahoma.

Once the algorithm has detected all the MCV-like vortices present in the RUC analyses, it remains to determine which of them are actually MCVs. Davis et al. (2002) report that the algorithm detects dry vortices in addition to MCVs; they suggest that these could be topographically generated since they tend to be concentrated in the immediate lee of the Rocky Mountains. For each vortex detected within a latitude-longitude box containing Oklahoma and part of the Texas panhandle, archived radar and satellite imagery are examined. Vortices are classified as MCVs only if they are embedded within, or arising from, significant stratiform precipitation and anvil cloud associated with deep convection. This definition is inevitably subjective, but the vast majority of the vortices detected by the algorithm are clearly MCVs or clearly not. Vortices associated with convection, but in the absence of any stratiform precipitation, are also

separately noted; these are fairly rare. All the MCVs detected by this algorithm over the state of Oklahoma are recorded, and each is examined in more detail using both observations and model data.

b. Mesonet and Profiler Analyses

For the purposes of this study, it is important to examine individual cases in detail. To this end, gridded mesoscale analyses are constructed for each case based on data from the Oklahoma Mesonet and the NPN. It has been noted in several previous mesoscale analysis studies (e.g., Fujita 1955, Bartels et al. 1997) that, under certain conditions, the density of observations in the vicinity of a moving feature of interest can be artificially increased by employing a time-space transformation. This involves determining the speed and direction of the motion of the feature being tracked. Once this is known, and assuming the feature is in a steady state (i.e., not changing significantly over the time separating observations), previous and subsequent observations at a point can be “transformed” from time to space. The additional observations are plotted along a line oriented along the direction of motion of the feature, and their separation distance from the original observation point depends on the speed of the feature of interest. Obviously, this approach introduces some error into a dataset. However, it can be quite useful in an environment of sparse observations, as long as the steady-state

approximation is not grossly violated. For this study, MCVs are the feature of interest, and it can be argued that they are at least approximately in steady state. Their very nature, as quasi-balanced systems, suggests that they evolve very slowly, and this is supported by the numerous reported cases of long-lived MCVs (e.g., Bosart and Sanders 1981, Fritsch et al. 1994, Galarneau et al. 2005; see also section 4a). A time-space transformation is carried out both for the Oklahoma Mesonet data and the NPN data. In order to avoid clear violations of the steady-state approximation, the transformation is only applied over a limited area surrounding the MCV. This area is a 3° latitude by 3° longitude box, centred over the MCV and moving with it through the state of Oklahoma. The size of the box was determined by trial and error, roughly guided by the fact that an MCV might be expected to influence its environment out to approximately a Rossby radius of deformation (~ 280 km in a typical MCS environment; Chen and Frank 1993). The speed and heading of each MCV are determined by the motion of the vortex in radar imagery. The Advanced Weather Interactive Processing System (AWIPS) software is used to display Level 3 radar data, and the AWIPS “distance-speed tool” is used to find the heading and speed of the vortices. All the MCV cases examined contain some radar echoes in their vicinity, which can be seen rotating around the vortex. Heading and speed are determined for two-hour periods throughout the passage of the system through Oklahoma, allowing a time-space transformation to be carried out for the same time

period. While it is likely that the heading and speed determined in this way are not always perfect, experimentation with differences in the system velocity have confirmed that the general mesoanalyses are not greatly affected by small changes in heading and speed. The time-space transformation for the Oklahoma Mesonet surface observations is carried out using the system speed for the two-hour period containing the observation time. For each observation, the two previous observations (five and ten minutes before) and the two following observations (five and ten minutes later) are transformed. The same method is used for the NPN upper-air observations, except only one previous observation (one hour earlier) and one subsequent observation (one hour later) are transformed. Figure 3.2 shows an example of the additional observations that can be obtained using this method.

With all the actual and artificial observations available, the actual analyses are carried out using multiquadratic interpolation. The characteristics and advantages of this method of analysis have been described in some detail by Nuss and Titley (1994). Multiquadratic analysis utilises radial basis functions to interpolate scattered observations onto a regular grid. The interpolation equation is

$$H(X) = \sum_{i=1}^N \alpha_i Q(X - X_i) ,$$

where $H(X)$ is some spatially varying field, $Q(X - X_i)$ is a radial basis function where the

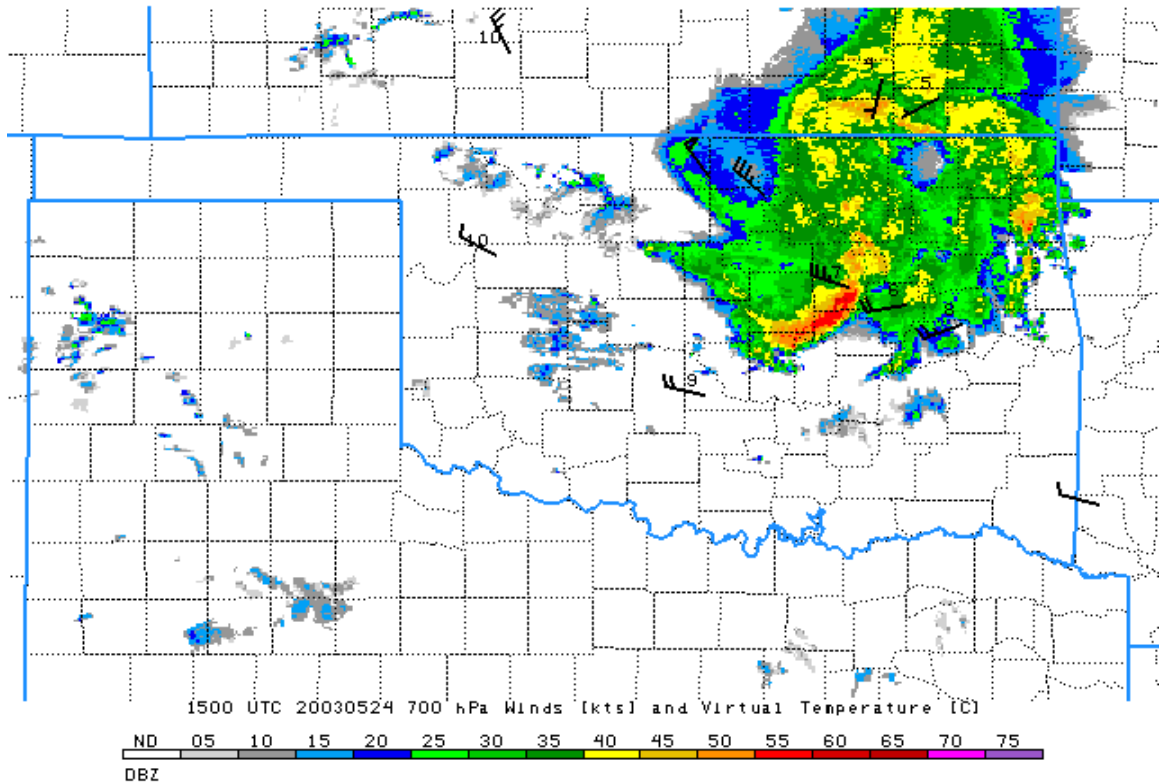


Figure 3.2: Observed NPN 700 hPa wind barbs and RASS virtual temperatures (°C) overlaid on NEXRAD composite radar reflectivity (colours; dBZ) at 1500 UTC on 24 May 2003.

argument represents the vector between an observation point X_i and any other point in the domain, and α_i are weighting factors to be determined from the observations. The basis functions are hyperboloids, given by the equation

$$Q(X - X_i) = -\sqrt{\frac{\|X - X_i\|^2}{c^2} + 1.0} ,$$

where c is a tunable parameter (the multiquadratic parameter). In matrix notation, when

observational error is considered and accounted for, the final interpolation equation is

$$\mathbf{H}_j = [\mathbf{Q}_{ij} + (N \lambda \sigma_i^2 \delta_{ij})] \boldsymbol{\alpha}_i ,$$

where \mathbf{H}_j is the analysed field, \mathbf{Q}_{ij} is the set of basis functions at each observation point,

N is the number of observations, λ is another tunable parameter (the smoothing

parameter), σ_i^2 is the mean-squared observation error, δ_{ij} is the Kronecker delta, and

$\boldsymbol{\alpha}_i$ are the coefficients determined from the observations. Historically, this method of analysis has not been much used in the field of meteorology, but the study by Nuss and Titley (1994) confirms that it is actually superior to two more popular methods: the Barnes and Cressman methods. Their study also demonstrates the influences of the two tunable parameters, the multiquadratic parameter and the smoothing parameter. The multiquadratic parameter, c , serves to keep the multiquadratic basis function from having discontinuous derivatives. It determines the sharpness of the curvature of the hyperboloids used in the interpolation. If c is small, the hyperboloids will have very sharp curvature, and thus tight gradients can be easily represented. Low values of c can also cause individual observations to affect only their immediate vicinity in the final analysis. If c is large, flat hyperboloids are used and the interpolation may have trouble with closely spaced observations and tight gradients. In this study, the multiquadratic parameter was extensively modified to find the optimal setting by trial and error.

Optimal results are obtained with $c=1.5$, and this setting is used for all analyses in this study. The smoothing parameter, λ , has the effect of reducing the small-scale noise in the final analysis. If λ is small, the analysis will retain a large amount of the noise arising from the original observations. If λ is large, it acts as a spectral low-pass filter to reduce the number of small-scale features and remove structure at short horizontal wavelengths. Once again, the smoothing parameter was chosen by trial and error. Small values of λ result in unrealistic values in data-sparse regions, due to the extrapolation of gradients by the interpolation technique. Very large values of λ result in excessive smoothing of real gradients associated with the MCVs. The best balance is achieved using $\lambda=0.000005$ for the mesonet analyses, and $\lambda=0.0001$ for the profiler analyses, and these values are used throughout this study. Different values of λ are used for the mesonet and profiler analyses due to the different inherent spacing of the observations in both cases. It was found that slight changes in these values do not greatly affect the analysis results, so the analyses can be viewed with some confidence. Analyses are carried out on a 0.1° latitude by 0.1° longitude grid covering the state of Oklahoma. Mesonet analyses cover the Oklahoma panhandle, whereas the profiler analyses do not.

Using the multiquadratic interpolation technique, a variety of surface plots are created from the Oklahoma Mesonet data. Plots are created for every 15 minutes throughout the MCV case analysis period. The 15-minute temporal resolution is dictated

by the background composite radar images obtained from WSI Corporation; these images are available only every 15 minutes. Analysis fields are overlaid on these radar images to provide a useful context for the observations. Mesonet observations that are analysed include the relative humidity (%), 1.5-m air temperature (°C), 10-m wind speed (m/s), 10-m wind direction (°), 10-m wind gusts (m/s), accumulated rainfall (mm), and station pressure (hPa). From these variables, several others are determined. The vapour pressure (e ; hPa) is given by

$$e = 0.06112 RH \exp\left(17.67 \frac{T}{T + 243.49}\right),$$

where RH is the relative humidity (%), and T is the 1.5-m air temperature (°C). The mixing ratio (r ; g/kg) is given by

$$r = 622 \frac{e}{p - e},$$

where p is the station pressure (hPa). The dewpoint temperature (T_d ; °C) is calculated from the equation

$$T_d = \left(\frac{1}{273} - 0.0001844 \ln\left(\frac{e}{6.112}\right) \right)^{-1} - 273.15 .$$

The station pressure variable is modified by removing the diurnal cycle of pressure from the raw observations. This is achieved by subtracting, for each station and for each 5-

minute observation during the day, the averaged pressure at that station and time of day over the month of interest. Pressure is also corrected to a constant elevation of 356.6 m, which is the average elevation of all the Oklahoma Mesonet stations. This is achieved by the equation

$$p' = p \exp \left(\frac{z - 356.6}{29.3 [T + 273.15] \left[1 + 0.6112 \frac{r}{1000} \right]} \right),$$

where z is the station elevation (m), and p' is the corrected 356.6-m pressure (hPa).

Equivalent potential temperature (θ_e ; K) is then determined from the equation

$$\theta_e = \left(T + 273.15 + \frac{L_v r}{1000 c_{pd}} \right) \left(\frac{1000}{p'} \right)^{0.286},$$

where L_v is the latent heat of vapourisation of water (2.5×10^6 J/kg) and c_{pd} is the specific heat capacity of dry air at constant pressure ($1004 \text{ JK}^{-1}\text{kg}^{-1}$). 10-m divergence (δ ; s^{-1}) and relative vorticity (ζ ; s^{-1}) are calculated from the 10-m wind field by the equations

$$\delta = \frac{\partial u}{\partial x} + \frac{\partial v}{\partial y} \quad \text{and}$$

$$\zeta = \frac{\partial v}{\partial x} - \frac{\partial u}{\partial y},$$

using centred-differencing. Finally, the accumulated rainfall variable is converted to a 5-min rainfall amount. Plots are created every 15 minutes of the observed 10-m wind barbs

and gusts at mesonet stations, and the analysed 10-m divergence, 10-m wind speed, station pressure corrected to 356.6-m elevation, 1.5-m relative humidity, 10-m streamline analysis, 1.5-m air temperature, 1.5-m dewpoint temperature, 1.5-m equivalent potential temperature, and 10-m relative vorticity. In addition to these surface maps, meteograms are also constructed for each individual mesonet station for the period of interest during each case. These meteograms display the 1.5-m air temperature and dewpoint temperature, 356.6-m pressure, 10-m wind barbs, 10-m wind speed and gusts, and 5-min accumulated rainfall.

Profiler fields are only available every hour; thus the pressure-level plots are overlaid on hourly composite radar reflectivity images. Directly observed variables include wind speed (m/s) and direction ($^{\circ}$) at 250-m vertical resolution, as well as RASS virtual temperatures ($^{\circ}\text{C}$) in the lower troposphere at certain profiler sites. These data are linearly interpolated to constant pressure levels at 25-hPa intervals. In cases where several hours of profiler data are missing, but with valid profiles before and after, the data are linearly interpolated in time. In addition to these directly observed variables, divergence (s^{-1}) and relative vorticity (s^{-1}) are determined on each 25-hPa level by centred-differencing. Plots are created every hour of the observed wind barbs at all of the eight profiler sites, as well as the analysed divergence, wind speed, streamline analysis, virtual temperature, and relative vorticity, at 850, 700, 500, 300, and 200 hPa.

Various types of plots are also created for each individual profiler site. Virtual temperature anomalies are calculated throughout the period of analysis for each MCV case at each RASS-equipped site. These are determined by subtracting the mean virtual temperature (determined separately for each level) over the analysis period from each individual virtual temperature observation. This provides an easy way to visualise virtual warming and cooling in the column above each profiler site, and can often provide guidance as to the mechanisms for surface effects around MCVs. Time-height sections of this virtual temperature anomaly, overlaid on profiler wind observations, are constructed for each profiler site and for each case. Skew-T/Log-p diagrams are also plotted for each profiler site at each analysis time. While the virtual temperature is strictly not equivalent to the actual air temperature, skew-T diagrams of the virtual temperature profile can give a basic sense of the state of the atmosphere. Hodographs are also constructed for each profiler site at each analysis time.

Finally, divergence and vorticity profiles, derived from the pressure-level gridded profiler analyses, are plotted through the centre of the MCV at each hour. The MCV positions used for these profiles are determined from the RUC analyses, as described in section 3c. These profiles can be compared with collocated ones from the RUC analyses to get a sense of the dynamics of the MCVs at various stages in their life cycle, as well as the performance of the RUC model.

c. RUC Analyses

For each MCV case, a variety of variables derived from the hourly RUC analyses are plotted. Some variables are directly included in the RUC data; others can be derived from the given variables. Each RUC analysis includes the following variables which are plotted each hour: surface-based CAPE (J/kg) and CIN (J/kg); surface mean sea level pressure (hPa); column-integrated precipitable water (mm); 2-m relative humidity (%) and temperature (°C); 10-m zonal and meridional wind speed (m/s); and pressure-level geopotential height (m), temperature (°C), relative humidity (%), zonal and meridional wind speed (m/s), and pressure vertical velocity (Pa/s). Derived variables that are plotted each hour include 10-m and pressure-level divergence (s⁻¹) and relative vorticity (s⁻¹); 2-m and pressure-level dewpoint temperature (°C) and equivalent potential temperature (K); and pressure-level mixing ratio (g/kg) and PV (PVU=10⁻⁶ Km²kg⁻¹s⁻¹). PV is calculated by the following equation:

$$PV = \frac{1}{\rho} ((\zeta + f) \cdot \nabla \theta) ,$$

where ρ is the air density (kg/m³), θ is the potential temperature, and

$$f = 7.292 \times 10^{-5} \sin(\phi)$$

is the Coriolis parameter (s⁻¹), where ϕ is the latitude (°). If we assume that the gradient of potential temperature is strictly in the vertical, then, using the hydrostatic

equation, we find that

$$PV = -g(\zeta + f) \frac{\partial \theta}{\partial p} ,$$

where g is the acceleration of gravity (9.8 m/s^2). Now, using the definition of potential temperature

$$\theta = T \left(\frac{1000}{p} \right)^{\frac{R}{c_p}}$$

where R is the gas constant for dry air ($287 \text{ JK}^{-1}\text{kg}^{-1}$) and T is in Kelvin, and substituting in numerical values, we find that, in units of PVU,

$$PV = -(9.8 \times 10^6)(\zeta + f) \left\{ \frac{\partial T}{\partial p} \left(\frac{1000}{p} \right)^{0.286} - 0.286 \left(\frac{1000}{p} \right)^{-0.714} \left(\frac{10 T}{p^2} \right) \right\} ,$$

where we have used the chain rule to evaluate the partial derivative of θ with respect to p . All moisture-related fields are derived from relative humidity, as shown in section 3b.

In general, surface fields are overlaid on mean sea level pressure contours, and pressure-level fields are overlaid on geopotential height contours. All of the above plots are created for each hour of the analysis period for each MCV. In addition, if the MCV is detected by the RUC algorithm before or after it moves through Oklahoma (i.e., before the beginning or after the end of the mesonet and profiler analysis period), plots are created for each of these times. Thus we can obtain an overview of the entire MCV life span with the RUC fields.

To aid in visualising the structure of the MCVs and their synoptic-scale environment, east-west and north-south cross-sections of some variables through the centre of the MCV are constructed. These variables include divergence, PV, relative humidity, equivalent potential temperature, zonal and meridional wind speed, relative vorticity, and mixing ratio. These cross-sections are overlaid on isentropes, which give a sense of the thermal structure of the system.

Finally, vertical profiles of several variables through the MCV centre are also constructed. The profile variables are divergence, relative vorticity, PV, and relative humidity. These profiles provide a means of following the evolution of MCV intensification and weakening by summarising the vertical structure of the vortices with regard to these variables.

d. Composite MCV Construction

Numerous past studies of individual MCVs have demonstrated that these systems pass through a predictable evolution during their lifetimes, and that the structure and intensity of a single MCV can vary greatly from one period to another (Fritsch et al. 1994; Rogers and Fritsch 2001). Thus, it would be advantageous to identify the life cycle evolution of the MCV cases studied here. Ideally, pure observations could be used to track the intensity of the vortex, and some criteria could be used to define life cycle

stages. However, the observations available in this study are quite sparse. Due to the varying degree of resolution of MCV circulations by the profiler network, the evolution of the analysed relative vorticity may be different from the evolution of the real relative vorticity. For example, when an MCV passes through the core of the profiler network its relative vorticity is likely to be fairly well resolved, but if a mature MCV passes along the edge of the network its relative vorticity may be analysed as much smaller than reality. It is thus difficult to unambiguously identify the time of the MCV's maximum relative vorticity using the profiler analyses. To circumvent these issues, this study utilises the RUC model to follow the evolution of MCVs throughout their life cycles. RUC data are used to define four different life cycle stages. MCV initiation is defined as the hour at which the MCV is first detected by the objective algorithm described in section 3a. MCV maturity is defined as the hour at which the MCV attains its maximum relative vorticity at any level between 600 and 500 hPa inclusive. MCV dissipation is defined as the hour at which the MCV is last detected by the objective algorithm. Finally, MCV development is defined as the analysis hour that is halfway between initiation and maturity (rounded up). While these stages of the life cycle of an MCV are admittedly arbitrary, they are at least consistent, and should be expected to provide a basic sense of the evolution of different MCVs. The RUC certainly has deficiencies in its representation of MCVs, due to issues discussed in section 2a. However, the advantage

of using the RUC is its consistency among all times, allowing an unbiased comparison of the longevity and evolution of different MCVs.

Using these four life stage definitions, it is possible to construct composite analyses for each of them. RUC data are used to create synoptic-scale composites of the initiation, developing, mature, and dissipation stages of MCV evolution. Each MCV case with valid RUC data at the times of interest is included in these composites. The RUC grids are shifted such that the vortices are all centred in Oklahoma (at 33.5° north, 97.5° west). The shifting of the vortices is accomplished based on the position of the 500 hPa relative vorticity maximum associated with each MCV at each analysis time. The horizontal position of the MCVs should not vary significantly between 600 and 500 hPa, so the composite fields should faithfully represent the MCV environment relative to the mid-level vortex centre. Due to the coarseness of the RUC data, these composites are mostly of use for investigating the synoptic scale environment of MCVs at different stages of their life cycles.

IV. MCV CLIMATOLOGY

This section presents the first part of the results of this study, summarising the main findings concerning mid-latitude MCV climatology and the synoptic-scale environment of these MCVs.

a. Climatological Characteristics

The results of the MCV detection algorithm over the study period of May-August 2002-05 are presented in Table 4.1, and are compared with results from previous climatological studies of MCVs. It should be noted that the detection methodologies of the previous studies have been of variable sophistication and efficiency, as discussed in section 3a. It is also important to recognise the differences in the experimental design between this study and that of Davis et al. (2002), despite the use of the same algorithm. Davis et al. (2002) ran the algorithm on 3-hourly RUC analyses, whereas hourly analyses are used in this study. Additionally, Davis et al. (2002) documented vortices throughout the Great Plains (see Figure 4.1), whereas this study documents vortices only in Oklahoma and the Texas panhandle. Thus, some differences in the frequency of MCVs are to be expected among these studies.

<i>Study</i>	<i>Time Period</i>	<i>Number of MCVs</i>
Bartels and Maddox (1991)	Jan 1981-Sep 1988	24
Trier et al. (2000b)	15 May-15 Sep 1998	16
Davis et al. (2002)	1 May-31 Aug 1999	43 (203)
This study	1 May-31 Aug 2002	20 (113)
This study	1 May-31 Aug 2003	21 (134)
This study	1 May-31 Aug 2004	39 (136)
This study	1 May-31 Aug 2005	15 (59)

Table 4.1: Comparison of the number of MCVs found in previous studies with this study. Numbers in parentheses indicate the total number of vortices (including non-MCVs) detected by the objective algorithm of Davis et al. (2002).

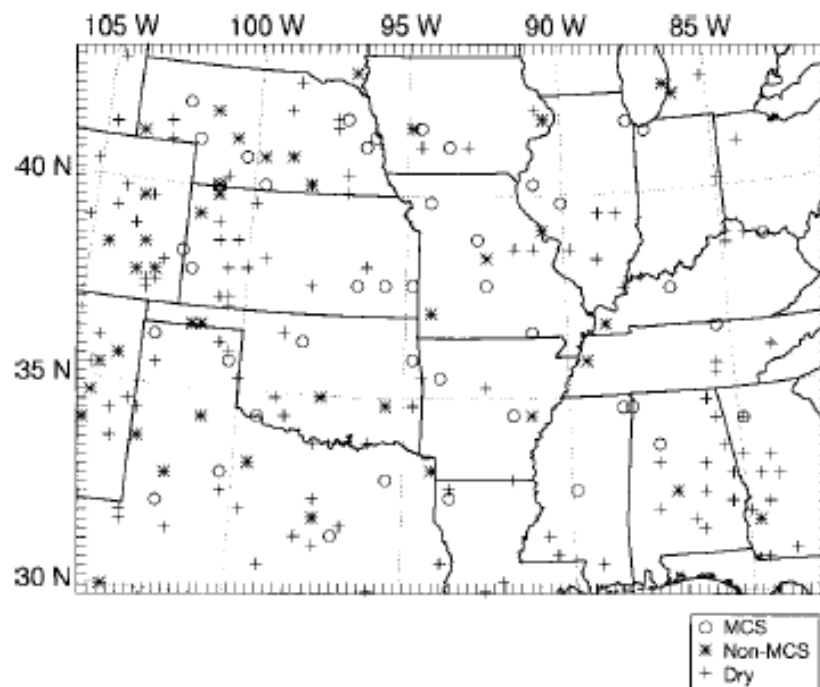


Figure 4.1: Domain over which MCVs were documented for May-August 1999 by Davis et al. (2002).

This study finds 95 MCVs over the four years of interest, with between 15 and 39 occurring each year. This is a significantly larger number of MCVs than has been found by Bartels and Maddox (1991) and Trier et al. (2000b), even though those earlier studies covered a much broader area. Assuming that the Davis et al. (2002) algorithm detects all MCVs, we can make a rough estimate that, in an average year, approximately 20 MCVs occur over Oklahoma and the Texas panhandle, out of perhaps ~100 throughout the Great Plains. The numbers in parentheses in Table 4.1 indicate the total number of vortices (i.e., the sum of MCVs and non-MCVs) for each year. Interestingly, both in this study and in Davis et al. (2002), the non-MCV vortices detected by the algorithm outnumber the actual MCVs. The differences in the domain sizes and the temporal resolution of the RUC data in the two studies can be overcome by comparing percentages of vortices that are MCVs. Overall, it appears that MCVs account for about 20% of the vortices that are detected by the objective algorithm. Given the design of the algorithm, and within its inherent limitations, we can conclude that MCVs constitute about 20% of the small-scale, circular, mid-level summertime vortices occurring in the Great Plains.

Forty-five of the 95 detected MCVs moved over the main part of Oklahoma at some point in their evolution, and these 45 cases are investigated in more detail in the remainder of this study. Figure 4.2 shows the seasonal distribution of these 45 cases. There appears to be a broad peak in the early summer (June), but it is difficult to draw

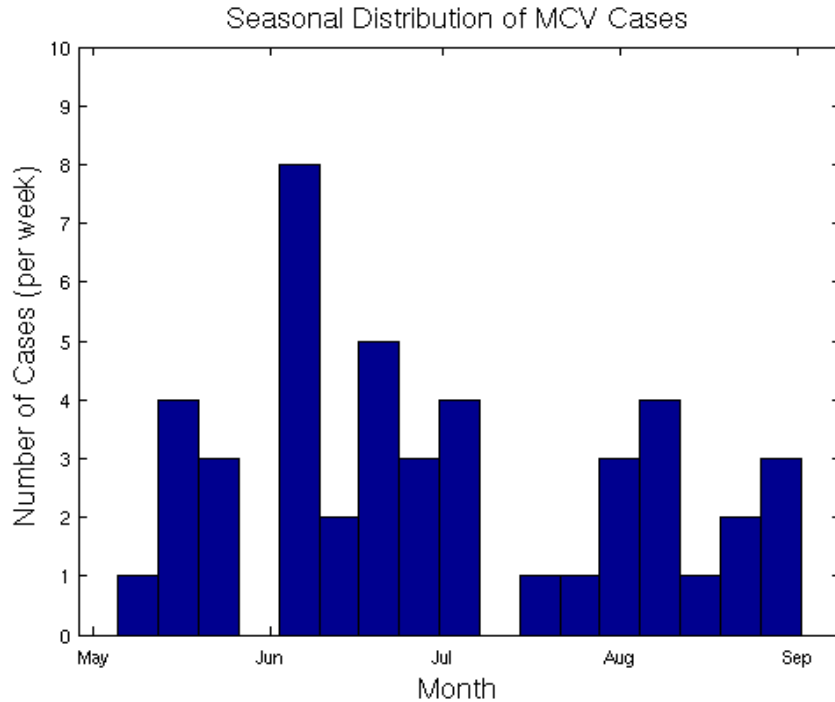


Figure 4.2: Seasonal distribution of MCV cases (by week) detected over Oklahoma during May-August 2002-05.

any firm conclusions about the seasonality of MCVs because of the extensive periods of missing RUC data (and thus likely missing MCVs) during the years 2002 and 2005. Figure 4.3 shows the seasonal distribution of available RUC data over the four years of interest, in terms of the number of available analysis hours per day. Note that a date with complete RUC data over all four years will contain (24x4) 96 analysis hours. Four years is likely insufficient to determine a climatological seasonal cycle.

For the MCV cases having valid RUC analyses at their initiation and dissipation, it is possible to determine the MCV longevity. This is defined as the number of hourly

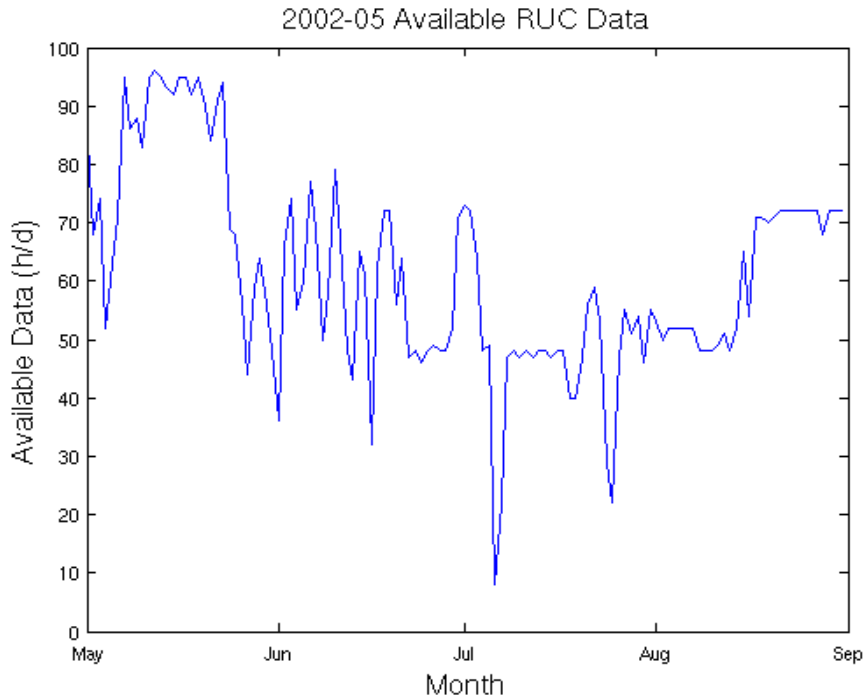


Figure 4.3: Seasonal distribution of available RUC data (hours per day) during May-August 2002-05.

RUC analyses between the initiation and dissipation of a single MCV, including the initiation and dissipation hours. The distribution of MCV longevity is shown in Figure 4.4. The distribution is quite asymmetric, with a long tail towards longer MCV lifetimes: the longest-lived MCV found in this study, occurring during 29 June-1 July 2003, lasted for 53 hours. It should be noted that, although all the MCVs included here passed over Oklahoma during some stage of their life cycle, it is possible to track the vortices before or after their passage of Oklahoma using the RUC analyses, which cover the entire contiguous United States. The peak in the longevity of the cases examined is six to ten hours. Four cases lasted five hours or less.

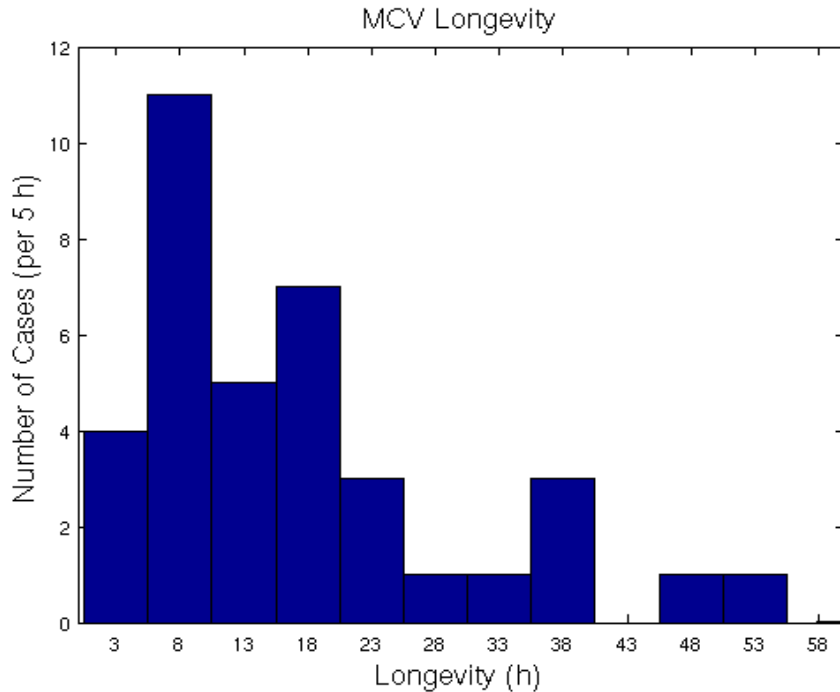


Figure 4.4: Longevity distribution of MCV cases, defined as the number of hours MCV is detected by objective algorithm.

Further insight into the evolution of the MCV cases is obtained by examining the timing of the stages of the life cycle with respect to the diurnal cycle. Figure 4.5 shows a histogram of the hour of MCV initiation, in local time (LT). There is a clear preference for MCV initiation to occur in the early morning hours, between 2300 and 0700 LT. Interestingly, this time period corresponds to the time of maximum extent in studies of central USA MCCs. Thirty-two of the 43 MCCs identified by Maddox (1980) during 1978, and nine of the ten MCCs included in the composite of Maddox (1983), reached their maximum extent during this time of day. This is strong evidence for the close association of MCCs and MCVs; MCVs tend to initiate towards the end of the life cycle

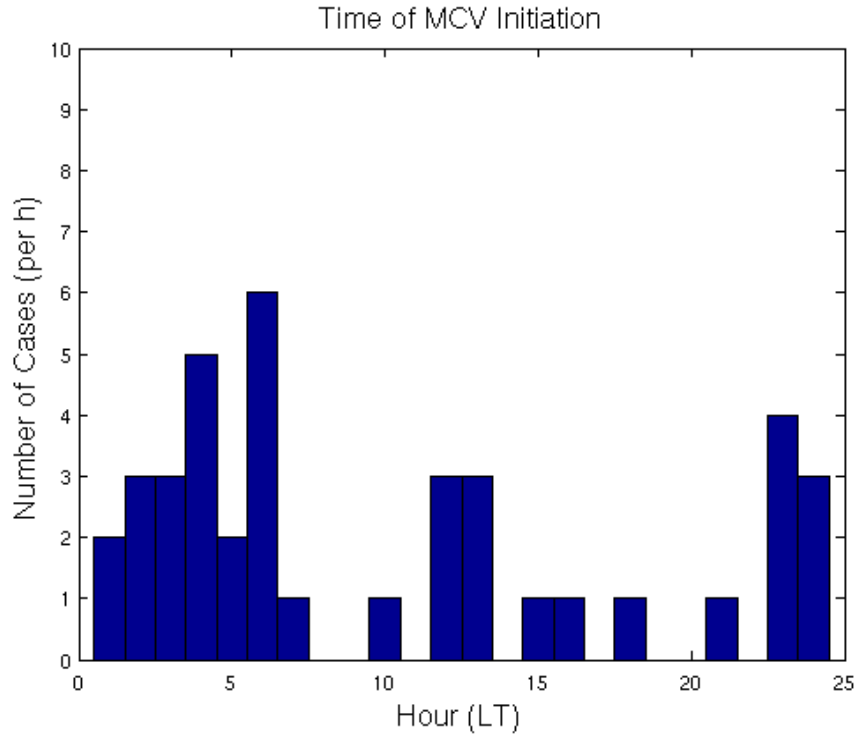


Figure 4.5: Diurnal distribution of MCV initiation (local time).

of nocturnal MCCs. There are very few MCV initiations after 1300 and before 2300 LT, demonstrating that MCV initiation is quite strongly tied to the diurnal cycle. The fact that there are exceptions, though, suggests MCVs can be associated with other types of MCSs besides nocturnal MCCs.

Figures 4.6 and 4.7 show similar histograms of the timing of maturity and dissipation among the MCV cases with respect to the diurnal cycle. The timing of these stages of the life cycle appears increasingly independent of the diurnal cycle, with maturity showing a slight preference for late morning (~0600-1200 LT), and dissipation

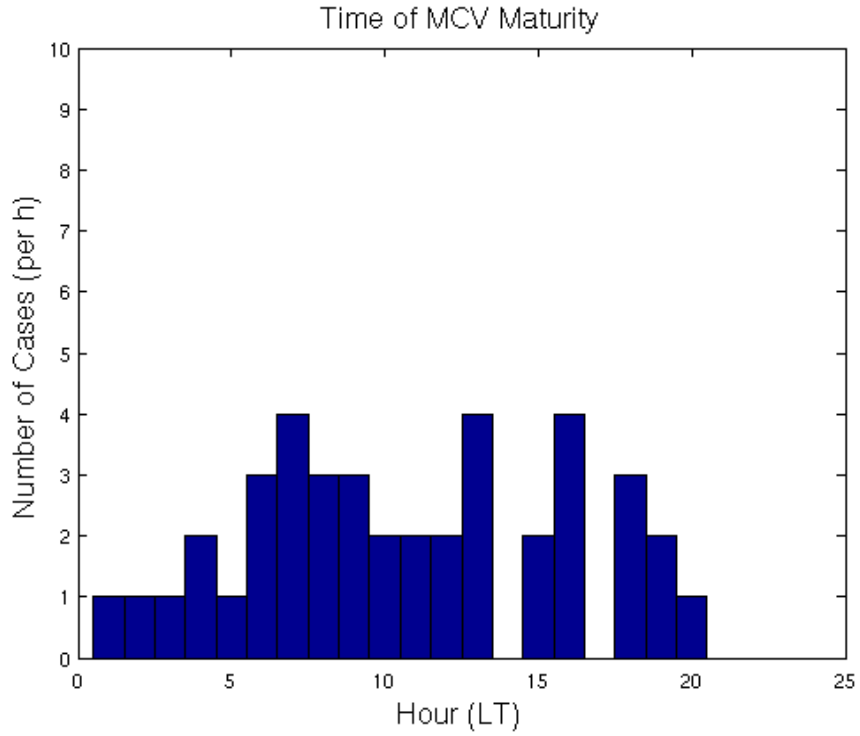


Figure 4.6: Diurnal distribution of MCV maturity (local time).

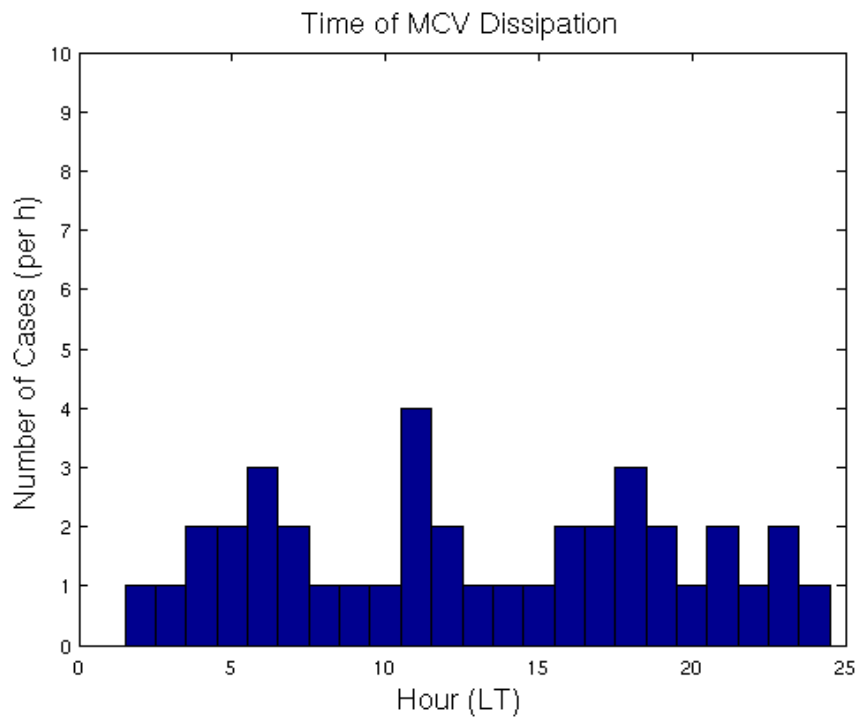


Figure 4.7: Diurnal distribution of MCV dissipation (local time).

showing no significant peak at any time of day. Taken together, these results suggest that MCVs follow a diurnal cycle in their evolution only to the extent that they initiate within nocturnal MCSs. It appears that, once they have formed, MCVs are independent of the diurnal cycle, with their longevity being determined by their intensity (Davis et al. 2002) and environmental conditions. However, the reinvigoration of MCVs by their secondary convection may be tied to the diurnal cycle (Fritsch et al. 1994; Rogers and Fritsch 2001; Trier and Davis 2002). It should be noted that the timing of the MCV life cycle stages presented here depends on the successful capture of the MCVs by the RUC analyses. MCV initiations could be underestimated by the RUC at certain times of day (for example during the early evening) due to their small initial size and the relative scarcity of upper-air observations at non-synoptic times.

Figure 4.8 displays the distribution of MCV sizes documented in this study. The MCV radius R is the same as that defined by Davis et al. (2002); it is the radius bin of RUC gridpoints at which the azimuthally-averaged 600-500 hPa relative vorticity first falls below 10% of the MCV's maximum (central) relative vorticity. This figure can be compared with Figure 8 of Davis et al. (2002); the metric is completely equivalent. In their larger sample of MCV cases, taken from the entire Great Plains, Davis et al. (2002) found a median vortex radius in bin 5, corresponding to an average radius of 185 km; the median radius in this study is located in bin 6, corresponding to an average radius of 224

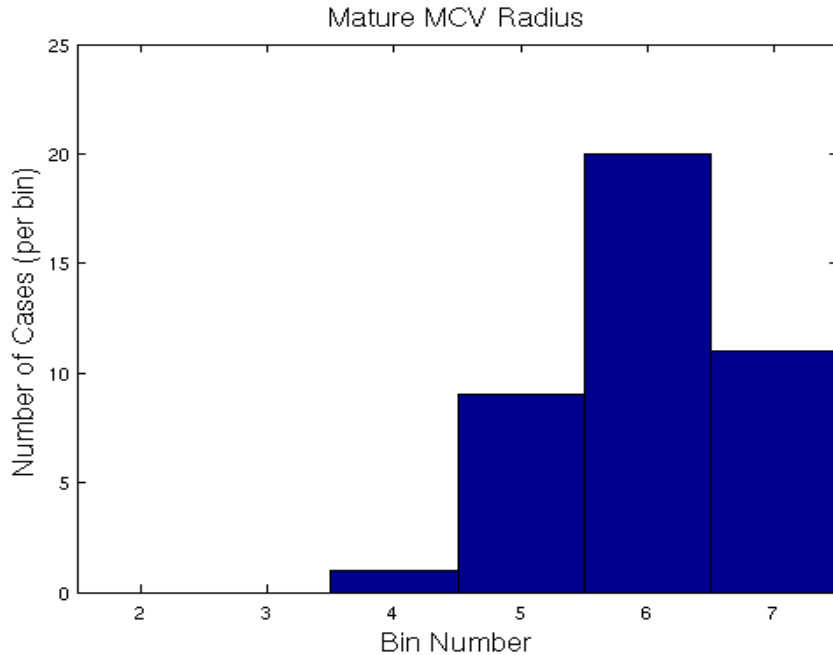


Figure 4.8: Distribution of MCV radius at system maturity, defined as the radius bin at which the MCV's azimuthally-averaged 600-500 hPa relative vorticity first falls below 10% of the central (maximum) relative vorticity. Bins 2-7 correspond to average radii of 49, 97, 142, 185, 224, and 262 km, respectively.

km. It is not known if this is a real difference between the year 1999 and the mean of 2002-05, a result of the different regions covered in the two studies, or a statistical artifact. Both studies demonstrate that the median MCV radius is within bin 7 (262 km), indicating that the cut-off radius of 300 km used in the MCV detection algorithm is likely appropriate. The distribution of intensity of the MCV cases is shown in Figure 4.9. For the purposes of this study, MCV intensity is defined as the mean 600-500 hPa relative vorticity at system maturity. MCV intensity varies between 2×10^{-5} and $2 \times 10^{-4} \text{ s}^{-1}$, with a broad peak between 9×10^{-5} and $1.4 \times 10^{-4} \text{ s}^{-1}$. This distribution of MCV relative vorticity

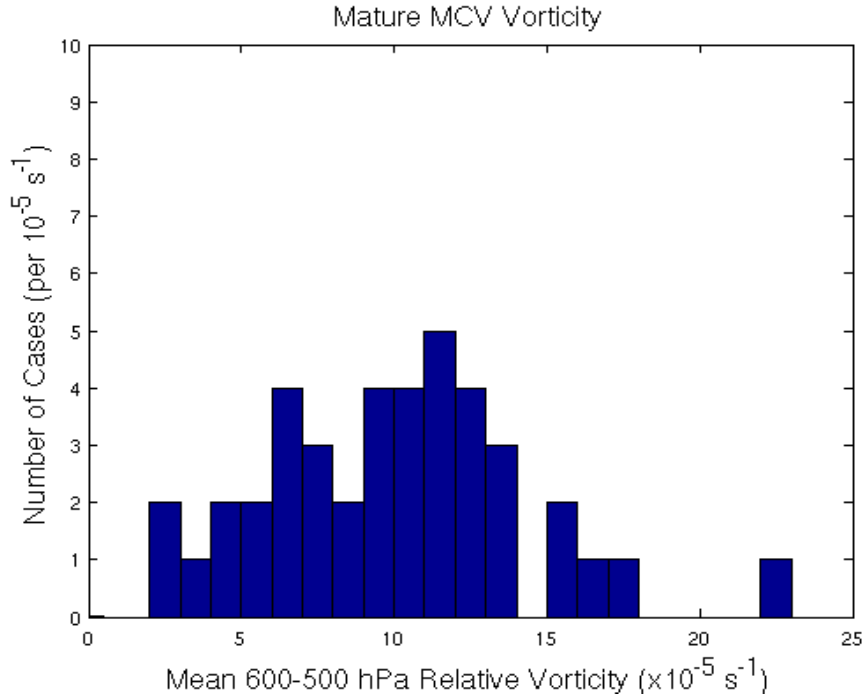


Figure 4.9: Distribution of MCV intensity, defined as the central 600-500 hPa average relative vorticity at system maturity ($\times 10^{-5} \text{ s}^{-1}$).

agrees quite well with that found by Davis et al. (2002), and displayed in Figure 9c of that paper.

In addition to the metrics described thus far, Davis et al. (2002) determined the frequency of MCVs which trigger secondary convection. Their definition of secondary convection, used again in this study, is the appearance of new radar echoes of greater than 40 dBZ reflectivity within ~ 200 km of the MCV centre. They found that 20 of their 43 MCV cases, or 46%, had convective retriggering. In this study, 17 of the 45 cases, or 38%, generate secondary convection within their circulations. Dividing the MCVs into two subsets, one of which generated secondary convection and the other of which did

not, allows us to determine differences in the key parameters of longevity and intensity. Figure 4.10 compares the intensity distributions of the two subsets. Differences between the two distributions are minor. Figure 4.11, similarly, compares the longevity distributions of the two subsets. These distributions may be compared with Figure 10a,b of Davis et al. (2002). As in that study, it is found that MCVs with secondary convection have a peak longevity in the range of 16-20 h, with much shorter and longer lived cases also sometimes occurring. MCVs with no secondary convection have a peak at shorter lifetimes, tailing off gradually towards long-lived MCVs. Figure 4.12 shows a scatterplot of MCV longevity and intensity. The distribution clearly suggests there is a positive relationship between the two variables: longer-lived MCVs tend to be more intense. This scatterplot may be compared with Figure 11 of Davis et al. (2002), which demonstrates the same relationship among the MCVs of 1999.

The individual MCV cases are classified into five types and examined in more detail in section 5; however, it is helpful to summarise some characteristics of their evolution here. Figure 4.13 shows the tracks of all 45 MCVs overlaid on a state map of the central USA. All of the MCVs have a general easterly component to their motion, due to the prevailing winds at this latitude. Beyond this, however, the systems have a variety of specific headings. Other features apparent from Figure 4.13 are the great variety of track lengths, and the occasional chaotic-looking system movement (generally

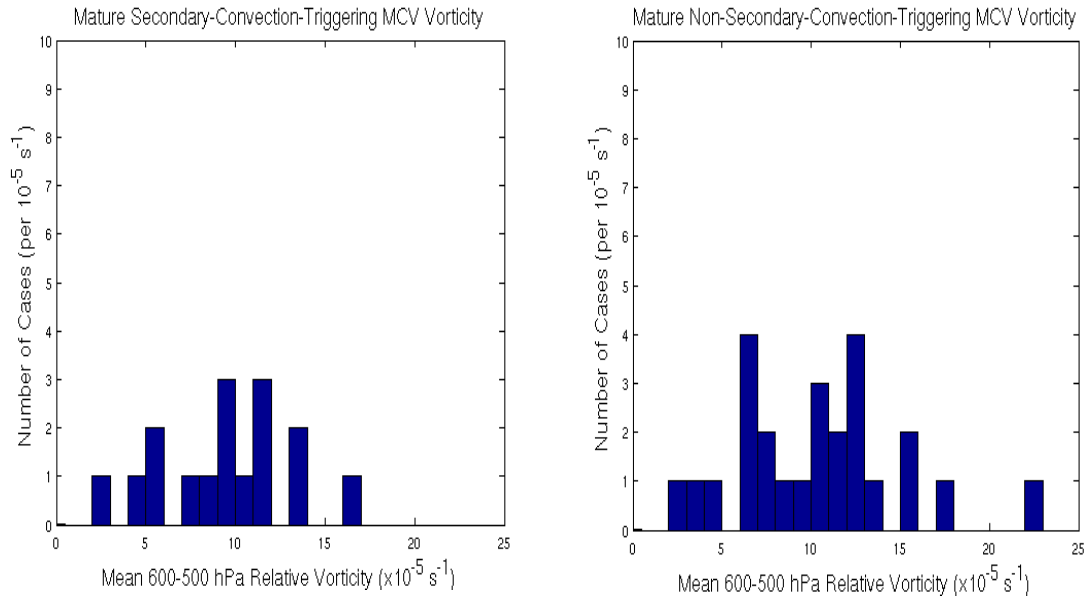


Figure 4.10: Distribution of MCV intensity ($\times 10^{-5} \text{ s}^{-1}$) for (left) secondary convection-triggering MCVs and (right) non-secondary convection-triggering MCVs.

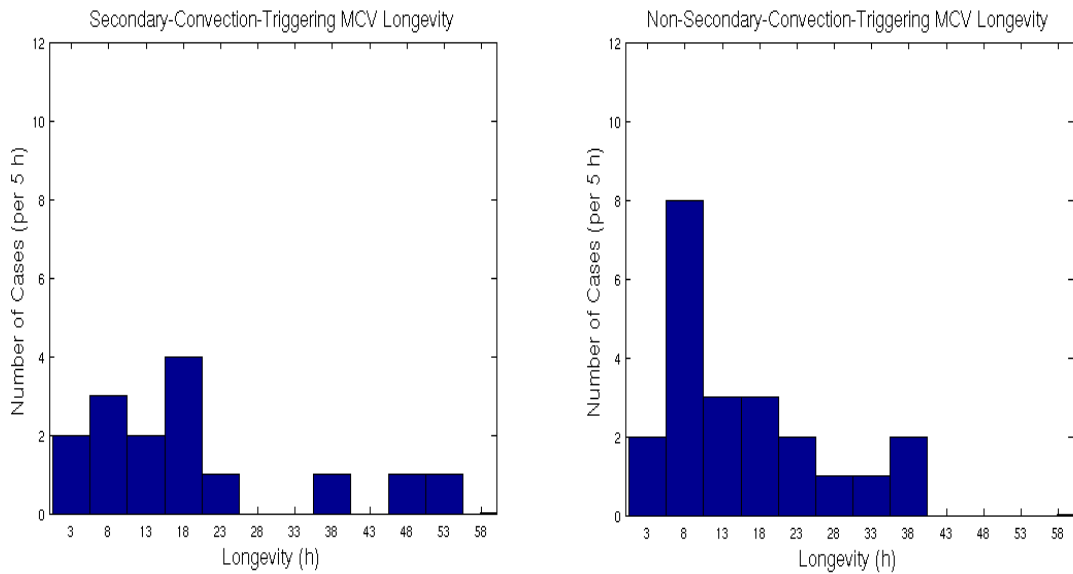


Figure 4.11: Distribution of MCV longevity (h) for (left) secondary convection-triggering MCVs and (right) non-secondary convection-triggering MCVs.

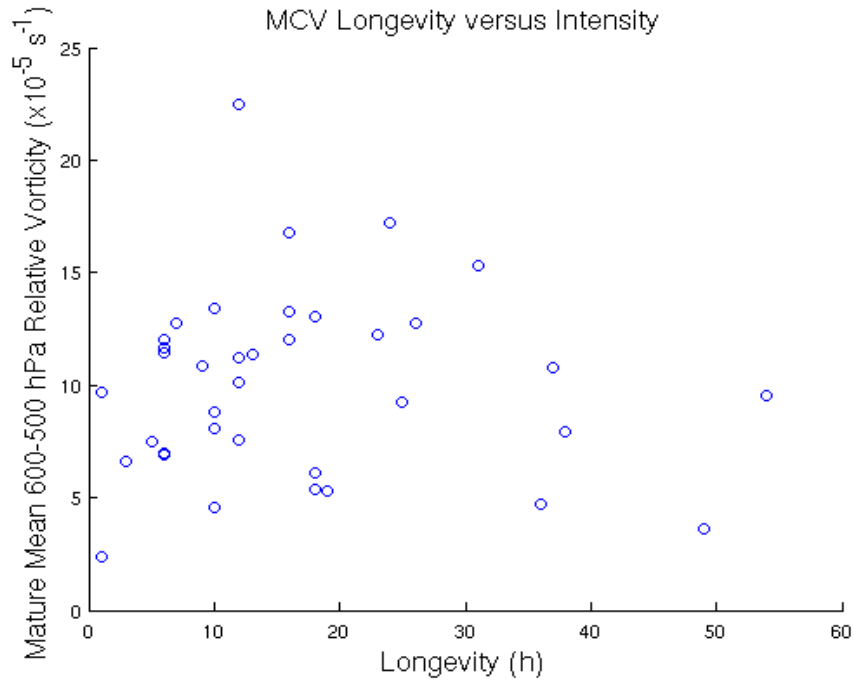


Figure 4.12: Scatterplot of MCV longevity (h) versus intensity ($\times 10^{-5} \text{ s}^{-1}$).

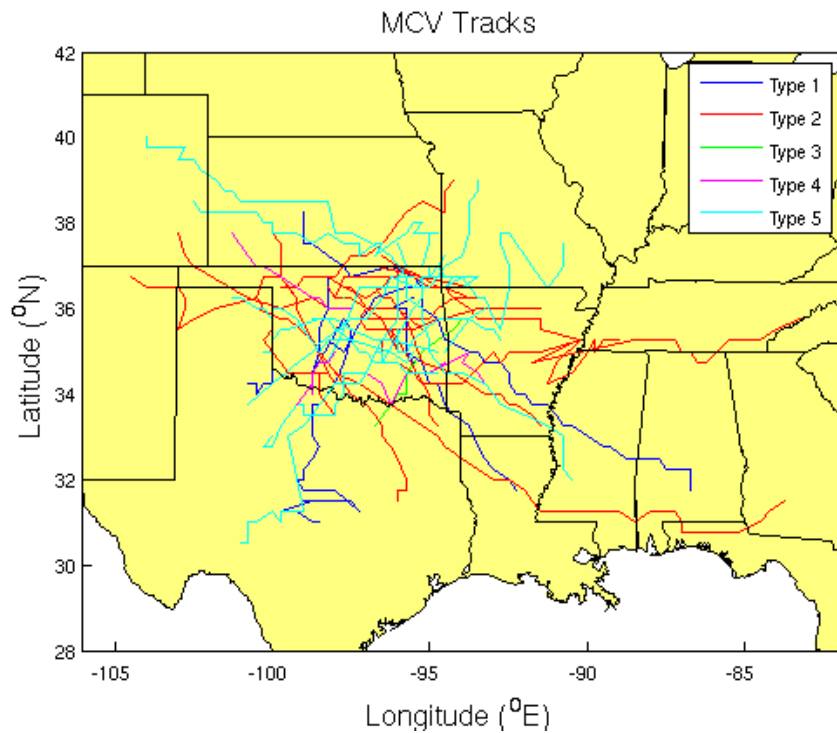


Figure 4.13: MCV tracks overlaid on state map of the south-central USA. Colours indicate the five MCV types identified in this study, as described in section 5a.

indicative of a nearly stationary MCV). Some of the track irregularities are likely due to the limitations of the RUC analyses, and their failure to always resolve the MCVs in the correct locations.

Figure 4.14 shows the relative vorticity evolution of the 45 MCV cases. It is difficult to generalise this evolution in any sense beyond the obvious tendency for an initial increase, followed by a decrease leading up to system dissipation. Several of the MCVs last sufficiently long to have several cycles of reintensification and weakening. It is beyond the scope of this study to rigorously assess the statistical significance of the relationship between these intensification periods and the vigour of secondary convection in the vicinity of the MCV, but there does appear to be an association based on a casual inspection.

Examination of surface pressure mesoanalyses for all 45 MCV cases reveals that 28 of the 45 vortices have significant surface mesolows associated with them. The varying sizes, strengths, and relative locations of the mesolows in each case suggest that no single mechanism is responsible for producing them. Figure 4.15 shows the tracks of the primary mesolows with respect to the vortex centre, for each case with a significant mesolow. The mesolow positions are plotted relative to the vortex centre; thus, the ground-relative mesolow tracks will differ from those in Figure 4.15 depending on the motion of the parent MCVs. The mesolows occur at varying times in the parent MCV

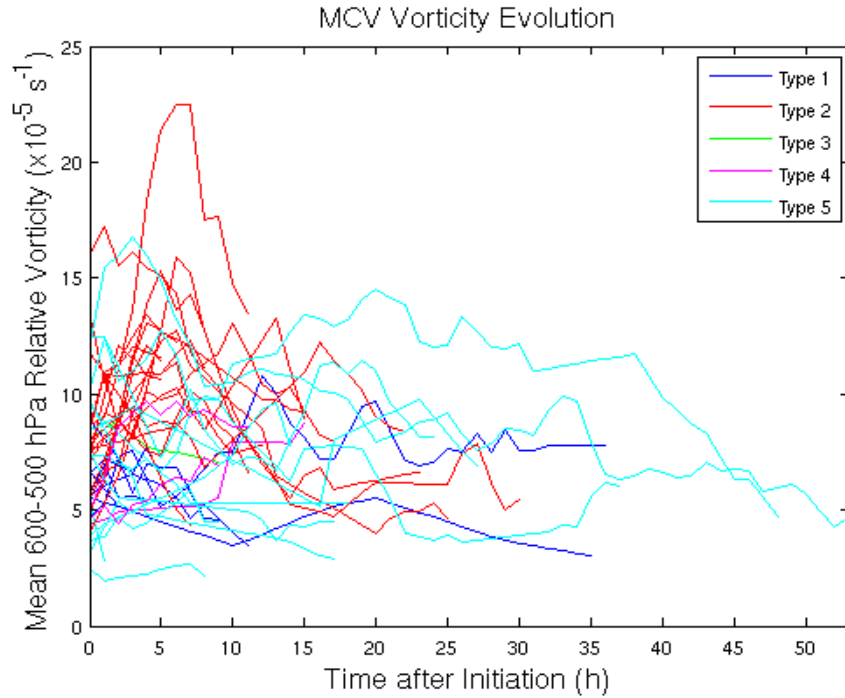


Figure 4.14: MCV mean 600-500 hPa relative vorticity ($\times 10^{-5} \text{ s}^{-1}$) evolution. Colours indicate the five MCV types identified in this study, as described in section 5a.

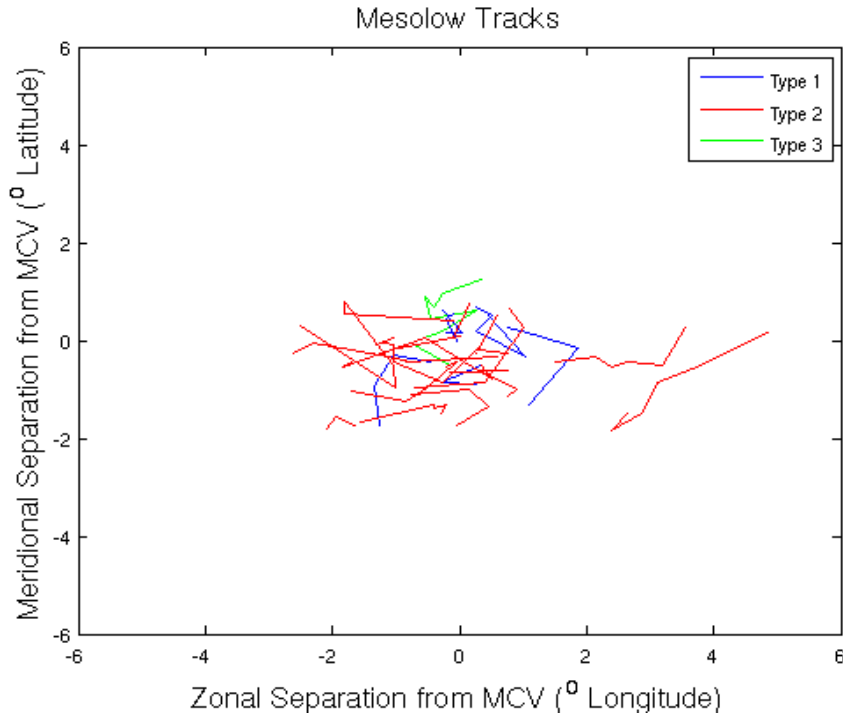


Figure 4.15: MCV primary mesolow track, with respect to MCV centre at 600-500 hPa. Colours indicate the five MCV types identified in this study, as described in section 5a.

life cycle, and have varying durations. In general, Figure 4.15 shows that the mesolows tend to remain fairly close to the MCV centre. There is a slight tendency for mesolow displacement relative to the MCV centre to be more in the zonal than in the meridional direction. The individual tracks tend to be oriented east-west, and their centroid is shifted slightly south of the MCV centre.

The vortex centres in Figure 4.15 have been determined based on the average relative vorticity over the 600-500 hPa layer; plotting the mesolow tracks with respect to the relative vorticity maximum at a single level produces different individual tracks in the many cases where the MCV is tilted to some extent, but the basic nature of the track distribution is unchanged. It is beyond the scope of this study to determine if the tilt of the MCVs in the RUC analyses is a real phenomenon, or a result of shortfalls in the RUC model. The separation frequently seen between the mid-level vortex and the surface mesolow suggests that, at least in many cases, the surface mesolow is not a direct downward penetration of the MCV. It is possible that MCV tilting in vertical wind shear plays a role in the positioning of the surface low pressure centre; significant tilt has been observed in real MCVs (e.g., Davis and Trier 2007). As will be shown in more detail in section 5, the mesolow does not appear to be a direct downward penetration of the MCV circulation in many of the cases examined in this study.

b. Composite MCV

Figures 4.16-4.19 show the mid-level (500 hPa) geopotential height and relative vorticity fields for the four life cycle stages defined in section 3d. A state map of the central USA is overlaid to provide a reference scale; it should be kept in mind that the composite construction involved shifting all MCVs to be centred in Oklahoma, so the map corresponds only to an average position of features among the different cases. It is apparent from Figure 4.16 that the mean MCV initiation location is downstream from a mid-level ridge and upstream from a mid-level trough. This positioning agrees well with that found by Bartels and Maddox (1991), as shown in Figure 4.20, despite the fewer cases identified in that study. The 500 hPa relative vorticity field at MCV initiation shows weak anticyclonic relative vorticity in the environment of the MCV, particularly upstream; this is associated with the anticyclonic flow around the nearby ridge. The MCV itself appears as a concentrated, circular region of cyclonic relative vorticity. At this initial time, there appears to be minimal deformation of the geopotential height contours in the vicinity of the MCV. In the developing and mature composites, shown in Figures 4.17 and 4.18, respectively, the MCV's relative vorticity intensifies and concentrates, while the environmental relative vorticity remains anticyclonic. The MCV becomes detectable as a mesoscale trough in the geopotential height field. At the dissipation stage (Figure 4.19), this mesoscale trough remains well defined, but the

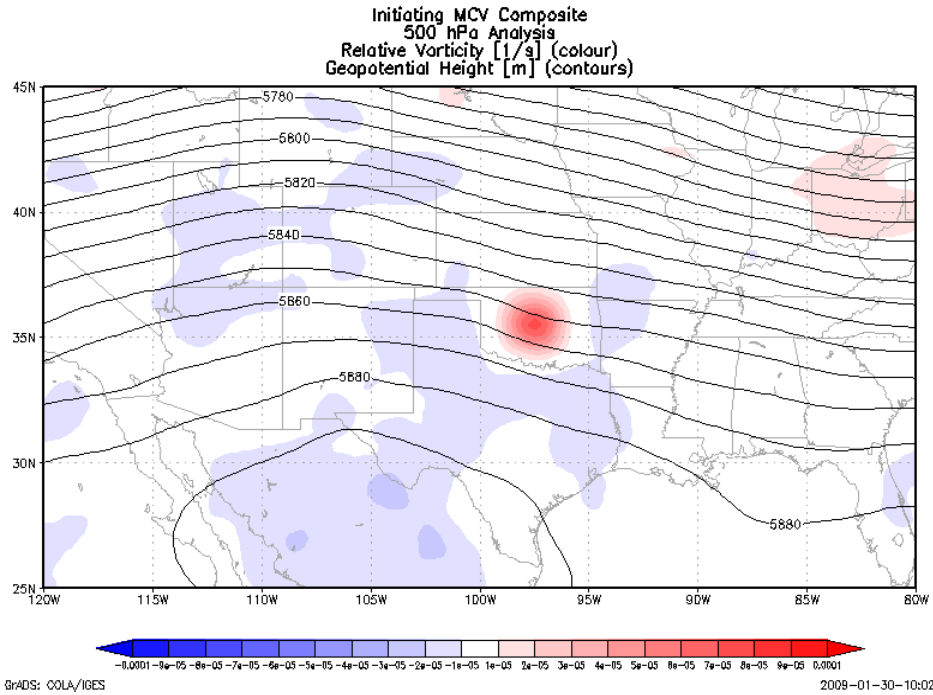


Figure 4.16: Initiating MCV composite (for MCV at 35.5°N, 97.5°W) of 500 hPa geopotential height (m; contour interval 10 m) and relative vorticity (colours; s^{-1}).

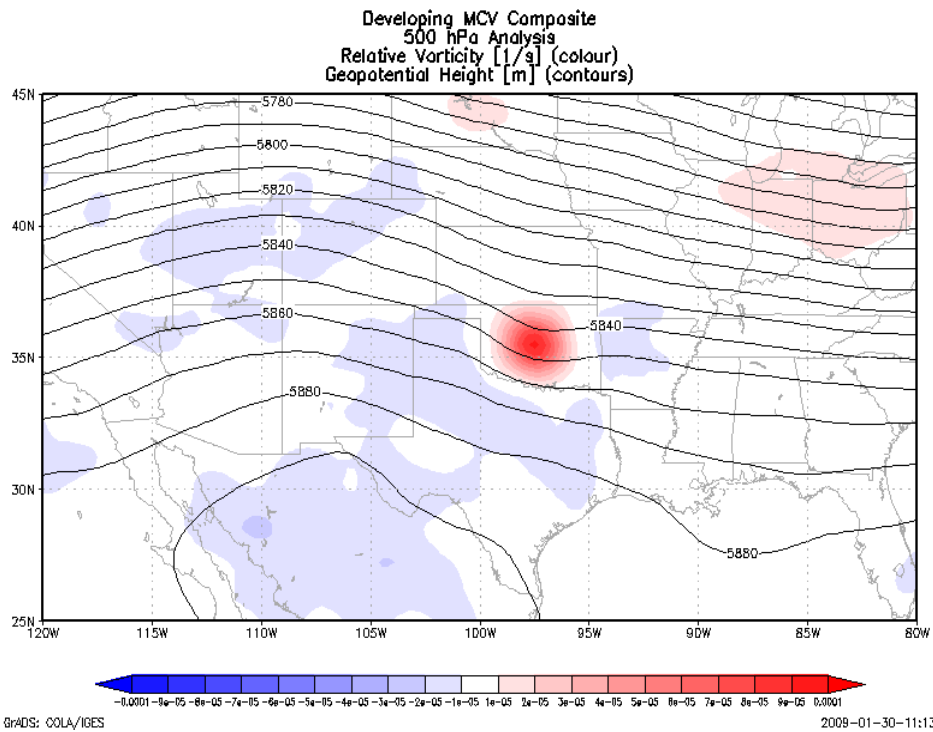


Figure 4.17: Developing MCV composite (for MCV at 35.5°N, 97.5°W) of 500 hPa geopotential height (m; contour interval 10 m) and relative vorticity (colours; s^{-1}).

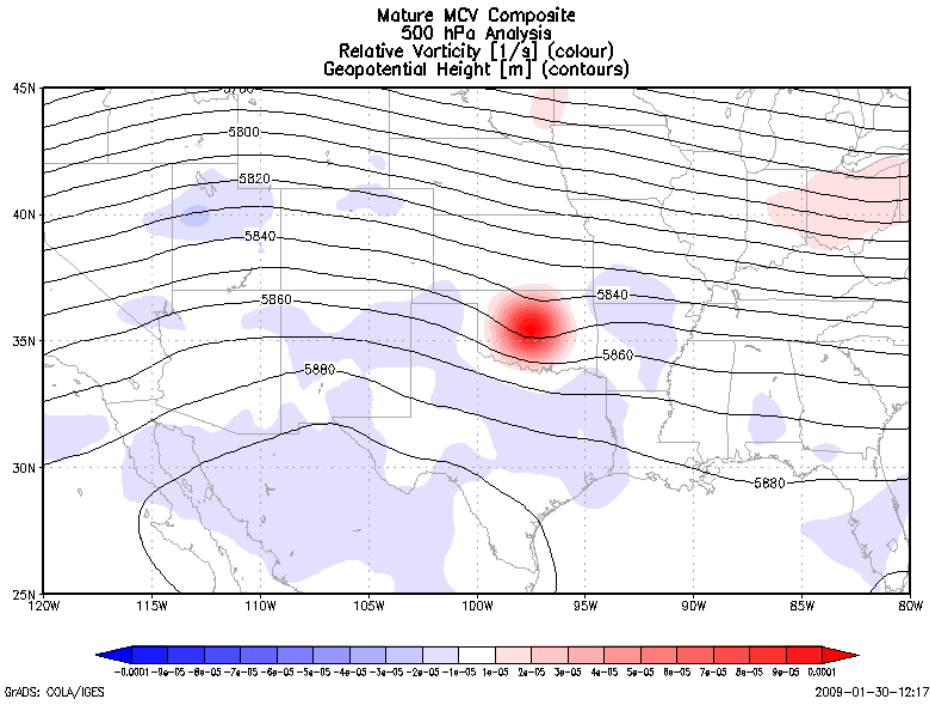


Figure 4.18: Mature MCV composite (for MCV at 35.5°N, 97.5°W) of 500 hPa geopotential height (m; contour interval 10 m) and relative vorticity (colours; s^{-1}).

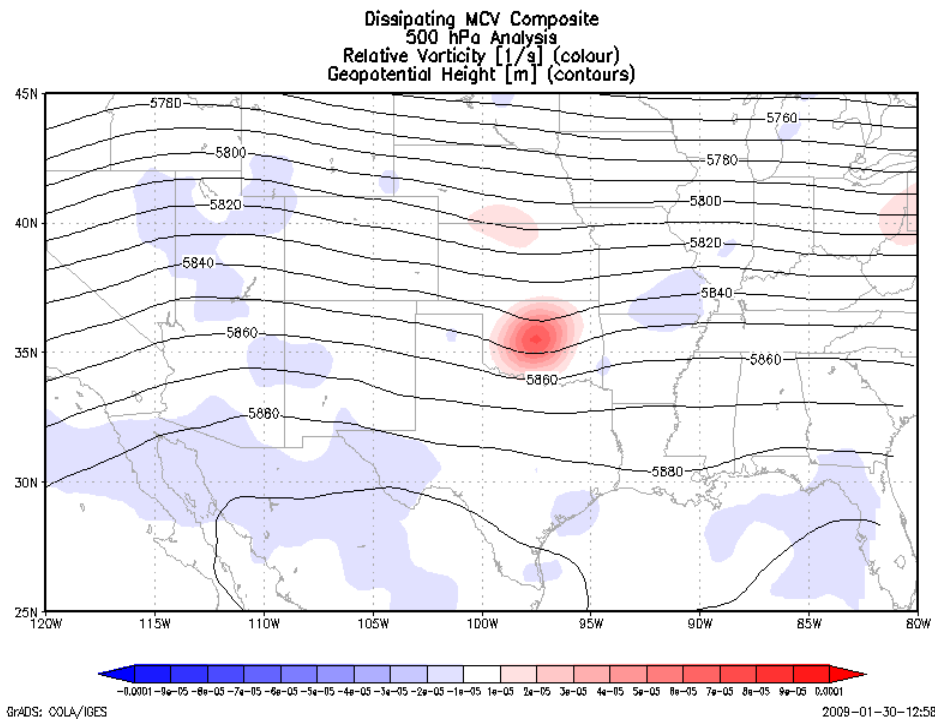


Figure 4.19: Dissipating MCV composite (for MCV at 35.5°N, 97.5°W) of 500 hPa geopotential height (m; contour interval 10 m) and relative vorticity (colours; s^{-1}).

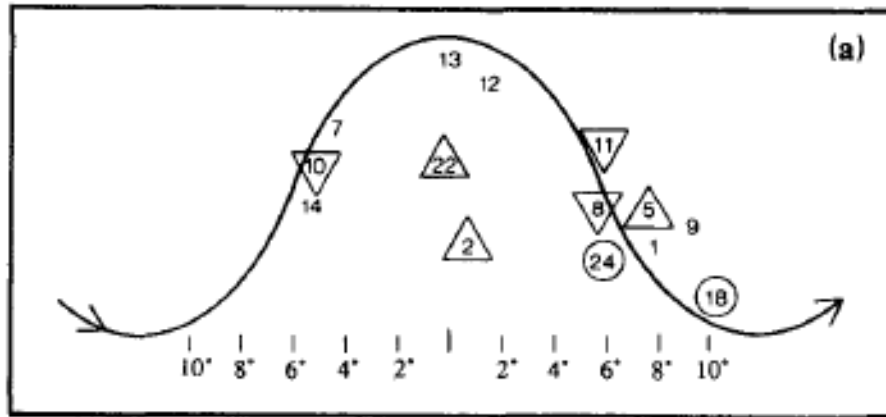


Figure 4.20: Location of MCV events found by Bartels and Maddox (1991) with respect to the 500 hPa large scale flow and ridge ($^{\circ}$ longitude from ridge axis) (from Bartels and Maddox 1991).

system's large core of cyclonic relative vorticity has clearly weakened and contracted considerably.

The 200 hPa composites reveal the average evolution of the MCV's upper-level environment. Figure 4.21 shows the initiating composite; there is a low-amplitude shortwave ridge centred over the system. Downstream of this, the relative vorticity field consists of a concentrated maximum of anticyclonic relative vorticity. This vorticity maximum corresponds to the upper-level outflow of the parent convection, which is, on average, still quite vigorous at this stage. It arises due to a strongly ageostrophic westerly jet streak which exits from the top of the convective system on its northeastern side (isotachs not shown). This feature was an important component of the mature MCC composite constructed by Maddox (1983), as can be seen in Figure 5f of that paper. This

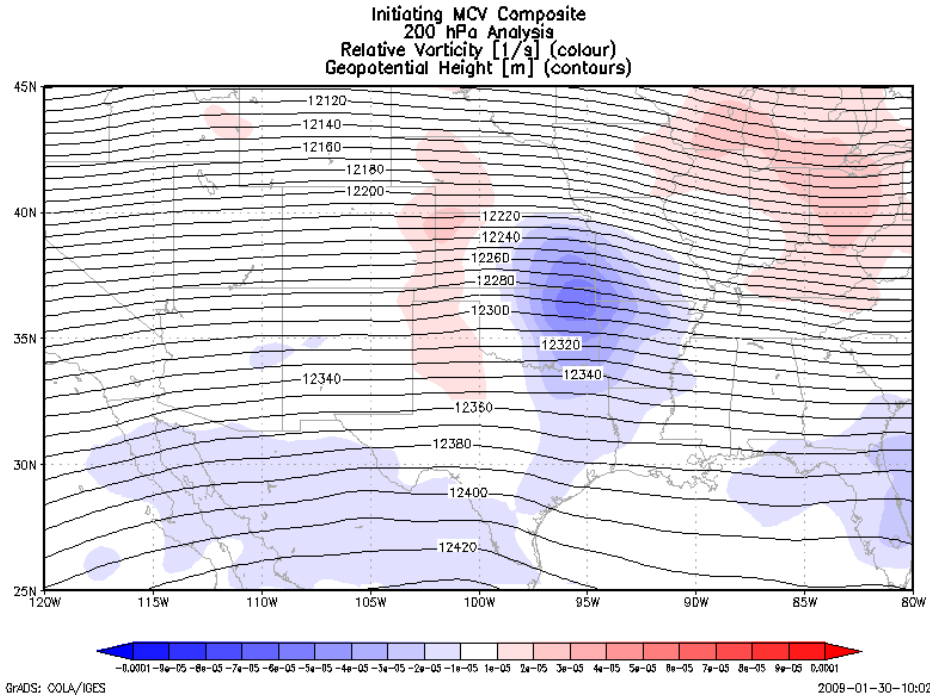


Figure 4.21: Initiating MCV composite (for MCV at 35.5°N, 97.5°W) of 200 hPa geopotential height (m; contour interval 10 m) and relative vorticity (colours; s^{-1}).

is further evidence that MCVs tend to be initiated at the mature stage of typical MCCs. As can be seen in Figure 4.22, which shows the same fields at the MCV dissipating stage, the upper-level anticyclone tends to persist throughout the MCV life cycle, albeit somewhat weakened due to the frequent demise of strong convection near the MCV centre.

Figures 4.23 and 4.24 show the initiating and dissipating composites at the 850 hPa level. Over the central plains, this level corresponds to the lower atmosphere around one km above the surface. However, this pressure level is below the surface over much of the high plains and Rocky Mountains, so the composites should be ignored in these

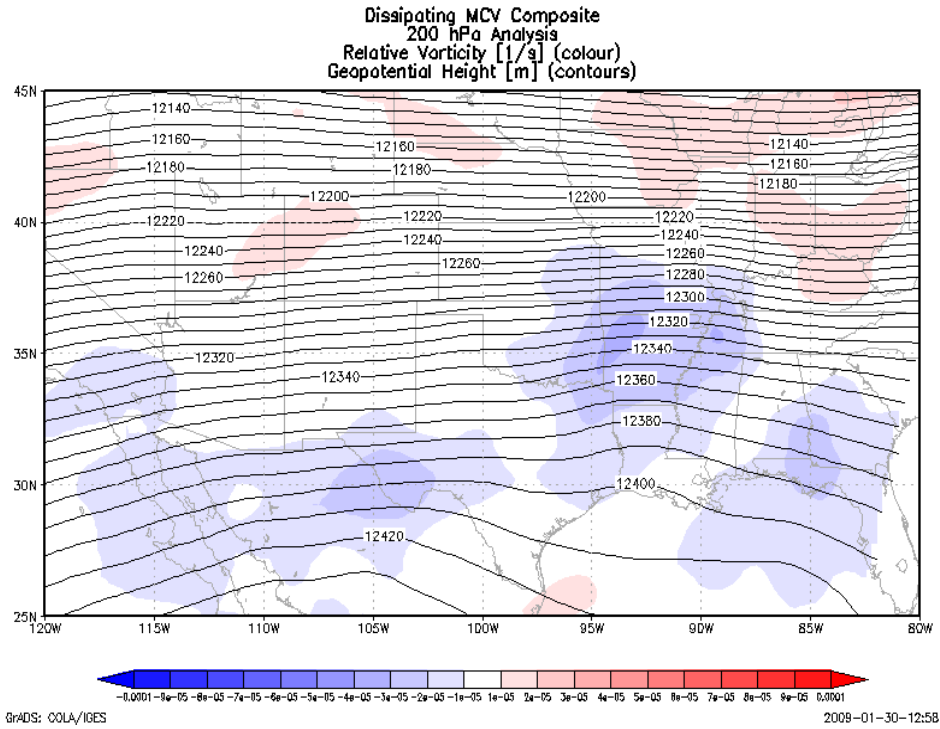


Figure 4.22: Dissipating MCV composite (for MCV at 35.5°N, 97.5°W) of 200 hPa geopotential height (m; contour interval 10 m) and relative vorticity (colours; s^{-1}).

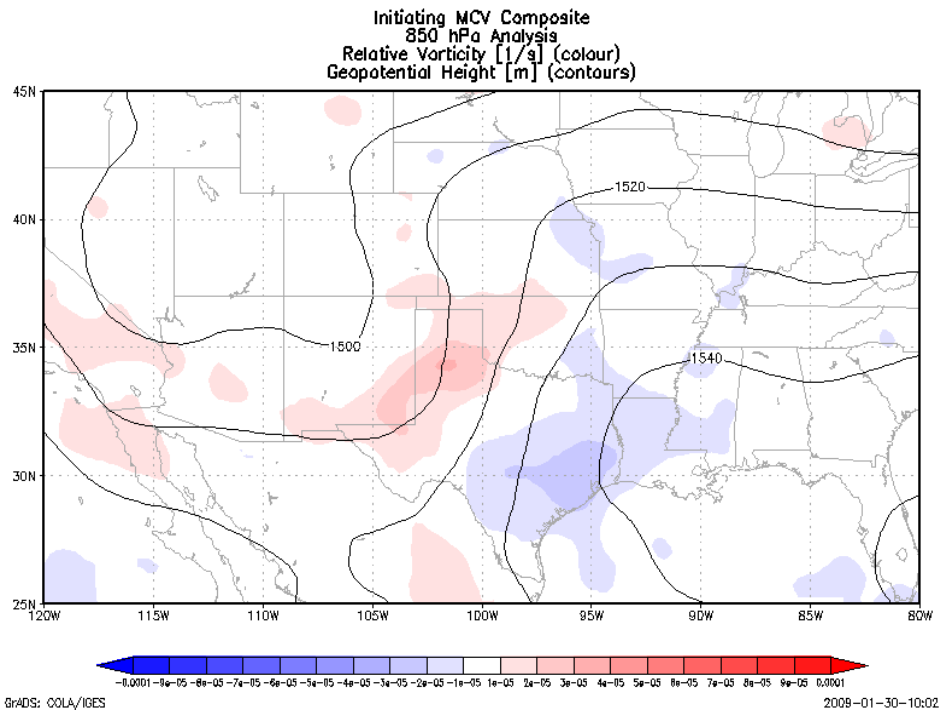


Figure 4.23: Initiating MCV composite (for MCV at 35.5°N, 97.5°W) of 850 hPa geopotential height (m; contour interval 10 m) and relative vorticity (colours; s^{-1}).

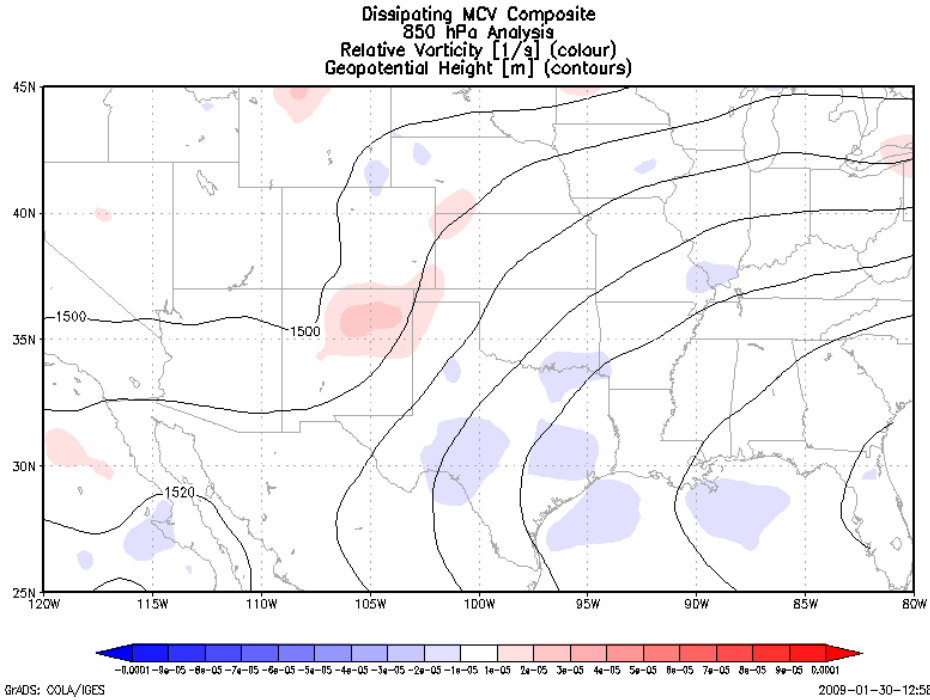


Figure 4.24: Dissipating MCV composite (for MCV at 35.5°N, 97.5°W) of 850 hPa geopotential height (m; contour interval 10 m) and relative vorticity (colours; s^{-1}).

locations. At MCV initiation, the height field consists of a broad trough to the northwest of the MCV, and a broad ridge to the southeast. This pattern would lead to southerly or south-southwesterly winds at this level, which corresponds to the well-documented Great Plains low-level jet (LLJ). This low-level wind maximum is most frequently observed in the early morning hours, which is the average time of MCV initiation. The LLJ is also seen in the mature MCC composite of Maddox (1983), as shown in his Figure 5c. At this stage of the MCV life cycle, the 850 hPa relative vorticity distribution appears dictated by the synoptic-scale height pattern, with cyclonic relative vorticity to the northwest, and anticyclonic relative vorticity to the southeast. Note that there is no trace of the MCV's

relative vorticity at this level, indicating that the MCV is confined to the mid levels at this time. At MCV dissipation, as shown in Figure 4.24, a similar height pattern persists, although the orientation of the height contours has shifted such that the 850 hPa winds are more veered (i.e., southwesterly). This corresponds to the average diurnal weakening of the LLJ, which can also be seen in the MCC decay composite of Maddox (1983; his Figure 6c). There is still no cyclonic relative vorticity evident at 850 hPa in the immediate vicinity of the MCV.

Initiating and dissipating MCV composites at the surface are shown in Figures 4.25 and 4.26. At both times, the surface pressure gradient points towards the east, between a large region of low pressure over the high terrain southwest of the MCV and the western edge of the Bermuda high encroaching on the eastern USA. This produces southeasterly flow at the surface. The surface dewpoint temperature field shows a large-scale moistening over the course of the MCV life cycle. However, this apparent moistening is likely an artificial effect arising from the compositing process. Since, on average, the MCVs move eastwards, they tend to be in a moister environment at their dissipation than at their initiation. During the compositing process, this moisture signature is shifted westward, leading to an apparent moistening over the Great Plains.

Profiles of variables through the composite MCV centre reveal several interesting features of the vertical structure. Figure 4.27 shows the vertical structure of the low- to

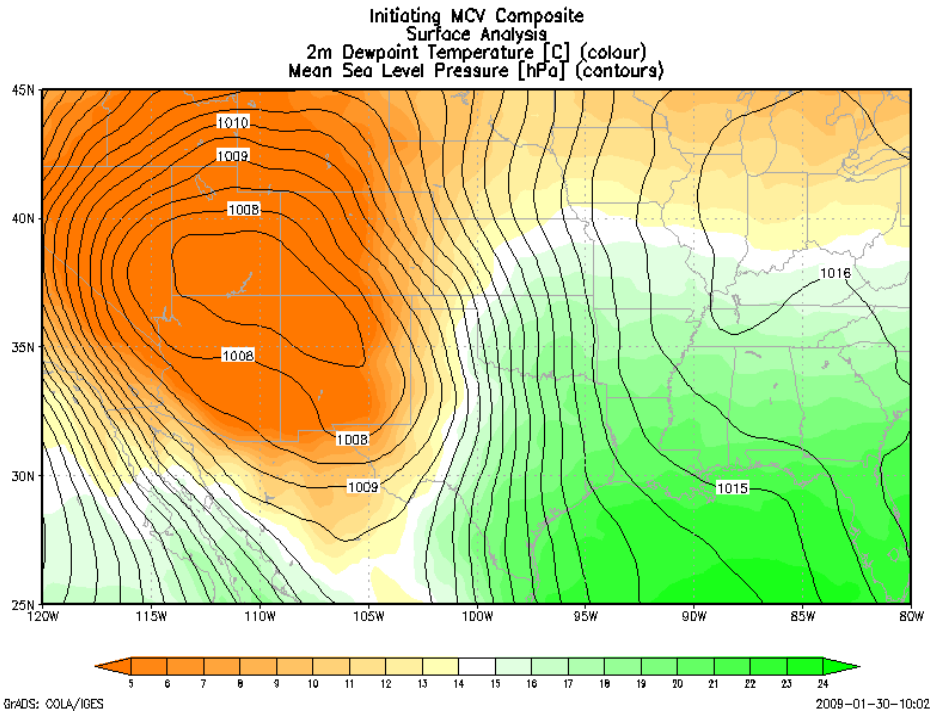


Figure 4.25: Initiating MCV composite (for MCV at 35.5°N, 97.5°W) of mean sea level pressure (hPa; contour interval 0.5 hPa) and 2-m dewpoint temperature (colours; °C).

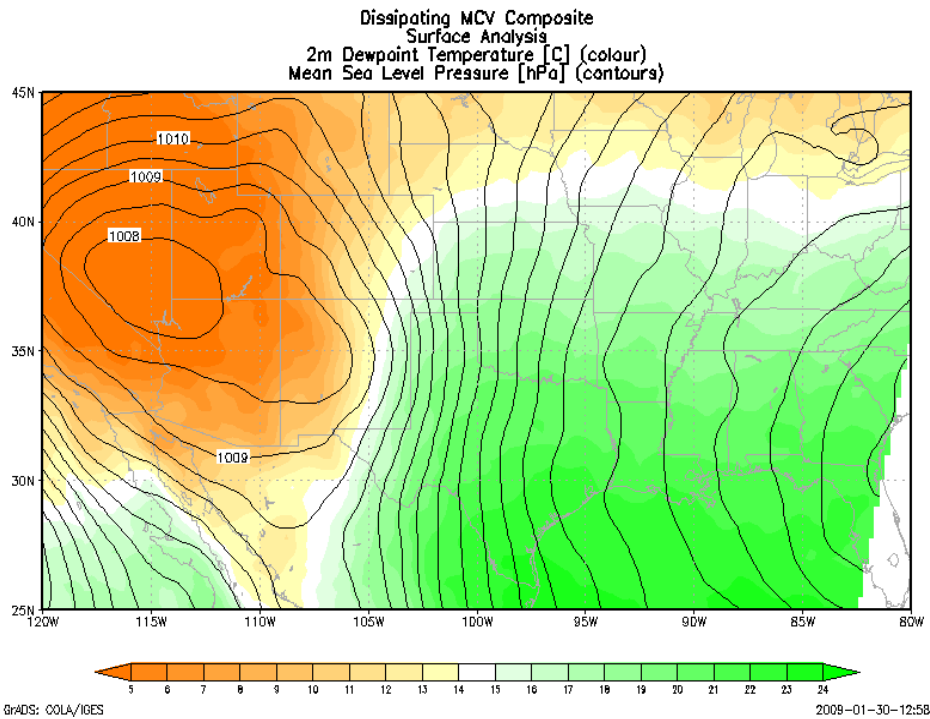
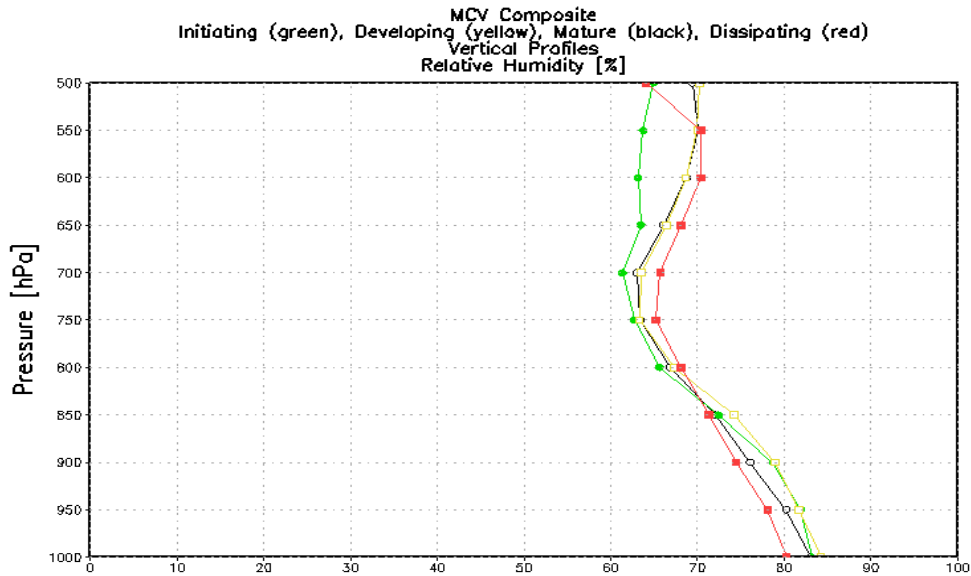


Figure 4.26: Dissipating MCV composite (for MCV at 35.5°N, 97.5°W) of mean sea level pressure (hPa; contour interval 0.5 hPa) and 2-m dewpoint temperature (colours; °C).



GrADS: OOLA/IGES

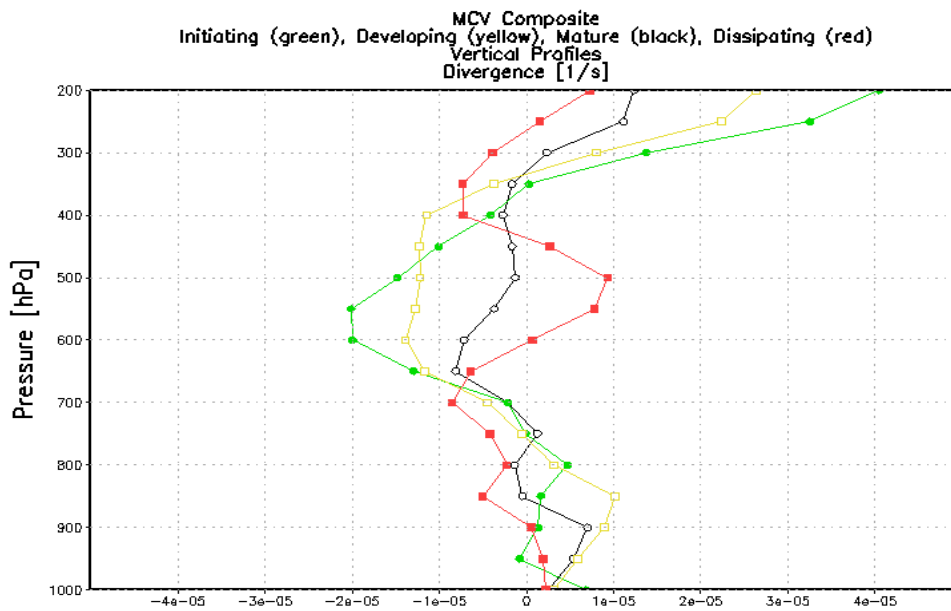
2009-01-27-09:23

Figure 4.27: Composite MCV profiles of relative humidity (%). Colours indicate the different life cycle stages: initiating (green), developing (yellow), mature (white), and dissipating (red).

mid-level relative humidity in the composite MCV. There is not much variability among the different composites, suggesting that the relative humidity remains fairly constant during a typical MCV's evolution. The highest values are near the surface, likely due to the effects of nocturnal surface inversions and shallow convective outflow layers. There is a well-defined minimum in relative humidity at 750-700 hPa, and a maximum above this layer. The RUC moisture data only extend up to 500 hPa, but the relative humidity is relatively high at this level. This could be due to MCV-related mid-level remnant cloudiness, often observed within the circulations of MCVs after the dissipation of the parent MCS.

The vertical structure of divergence at the different composite MCV life cycle stages is shown in Figure 4.28. The strongest mid-level convergence, a well-documented feature within mature MCSs, appears at the initiating stage of the MCV. This signature decreases at the developing and mature stages, actually transitioning to divergence at the MCV dissipation. These results are consistent with the vorticity equation: the MCVs are typically intensifying when they initiate, and weakening when they dissipate, due to mid-level convergence followed by divergence. Near the surface, there is a weak tendency for divergence, likely due to the demise of deep convection in the vicinity of the MCVs. Upper-level divergence, due to convective outflow, is strongest at MCV initiation, weakening in the later composites. All of these features appear quite weak in the composite; there is large variability from case to case.

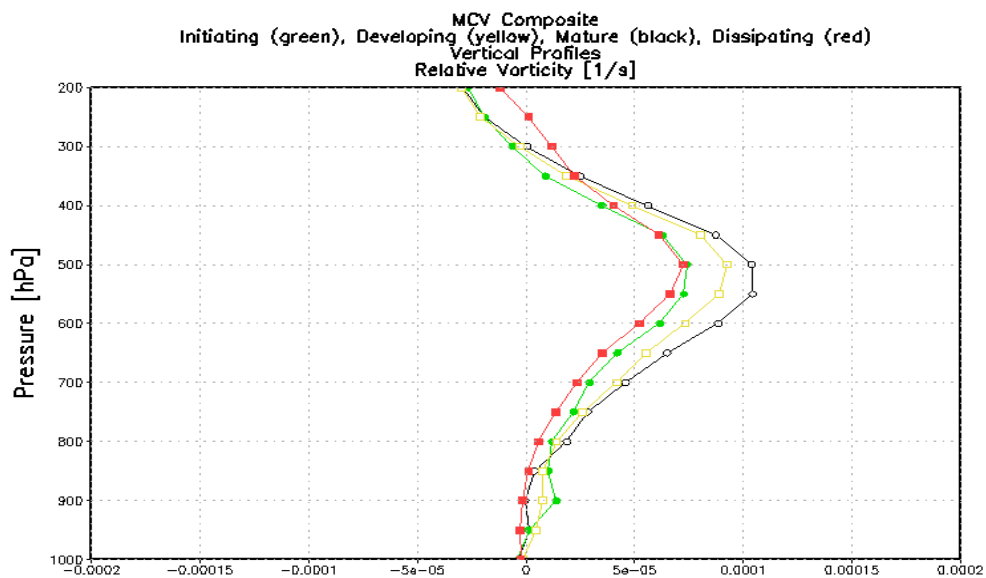
The relative vorticity profiles are shown in Figure 4.29. Relative vorticity peaks at 550-500 hPa, decreasing sharply above this and somewhat less sharply below. Consistent with the definitions of the life cycle stages, the strongest mid-level relative vorticity appears in the mature composite. The structures of the profiles are very similar among the different life cycle stages, only significantly varying in the intensity of the relative vorticity maximum. Relative vorticity is near zero at the surface (although slightly cyclonic at the initiation and developing stages), and somewhat anticyclonic at and above 250 hPa.



GrADS: COLA/IGES

2009-01-26-14:52

Figure 4.28: Composite MCV profiles of divergence (s^{-1}). Colours indicate the different life cycle stages: initiating (green), developing (yellow), mature (white), and dissipating (red).



GrADS: COLA/IGES

2009-01-27-08:40

Figure 4.29: Composite MCV profiles of relative vorticity (s^{-1}). Colours indicate the different life cycle stages: initiating (green), developing (yellow), mature (white), and dissipating (red).

Several previous studies (e.g., Fritsch et al. 1994, Davis and Trier 2002, Conzemius et al. 2007) have investigated MCVs from a PV perspective, examining profiles and cross-sections of PV from both observational and model data. The PV structure of the composite MCV constructed in this study can be compared with these previous results. North-south cross-sections of the composite MCV PV structure at the four life cycle stages are shown in Figures 4.30-4.33. The isentropes, contoured every 2 K, show the static stability component of the PV field. Note that the relevant thermal structure of the MCV is superimposed upon a synoptic-scale temperature gradient; the isentropes slope upward towards the north. At all four times, the MCV appears as a concentrated cyclonic PV anomaly with a maximum PV greater than 1 PVU, centred near 500 hPa. This anomaly occurs within a background 500 hPa PV of approximately 0.3 PVU. In the initiating composite, an additional PV maximum appears at low levels (near 900 hPa). It is believed that this maximum is due to enhanced low-level stability in the early morning hours, which tends to be the time of MCV initiation. This feature does not appear during the later stages of the MCV composite. By the time of the developing composite, the MCV has intensified markedly. The isentropes within the PV maximum have become more closely spaced, indicating greater static stability. Comparison with the initiating composite reveals that this greater stability is due to warming (depressed isentropes) immediately above the MCV and cooling (raised isentropes) immediately

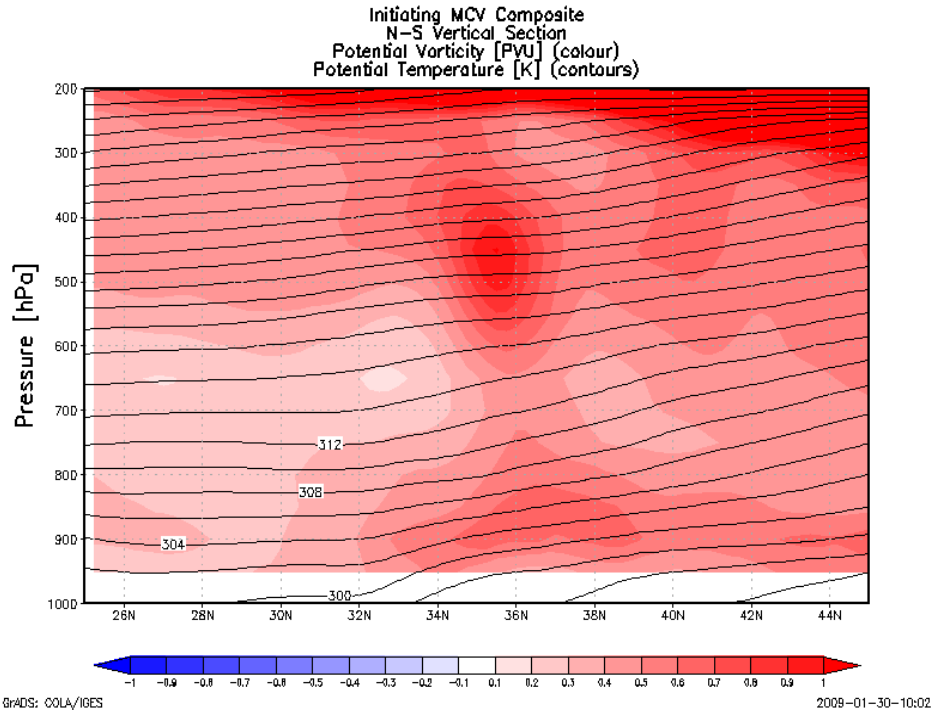


Figure 4.30: Initiating MCV composite (for MCV at 35.5°N) north-south cross-section of potential temperature (K; contour interval 2 K) and potential vorticity (colours; PVU).

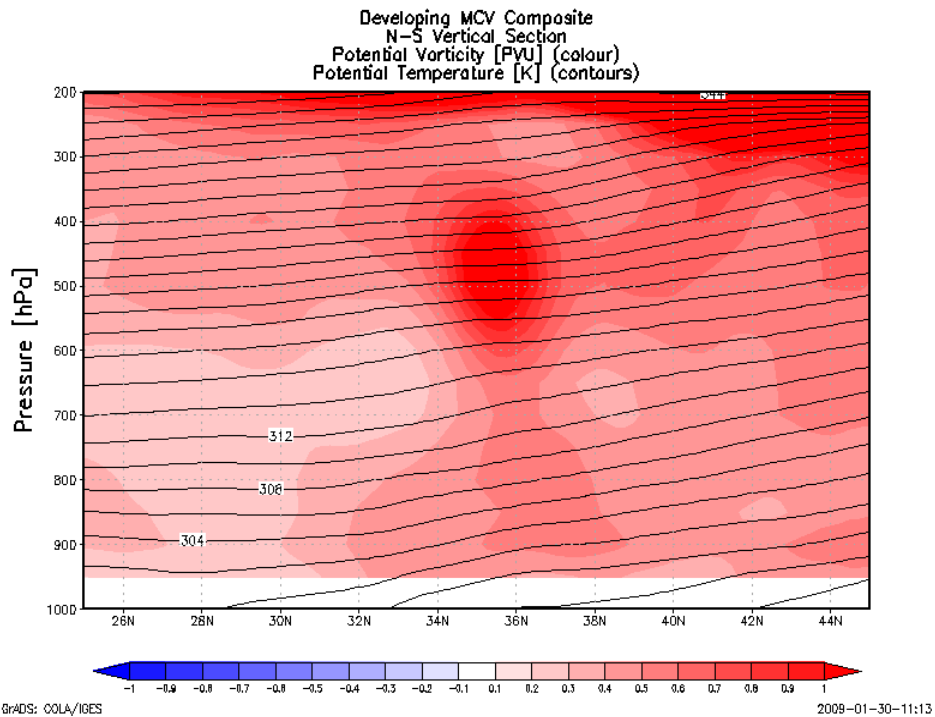


Figure 4.31: Developing MCV composite (for MCV at 35.5°N) north-south cross-section of potential temperature (K; contour interval 2 K) and potential vorticity (colours; PVU).

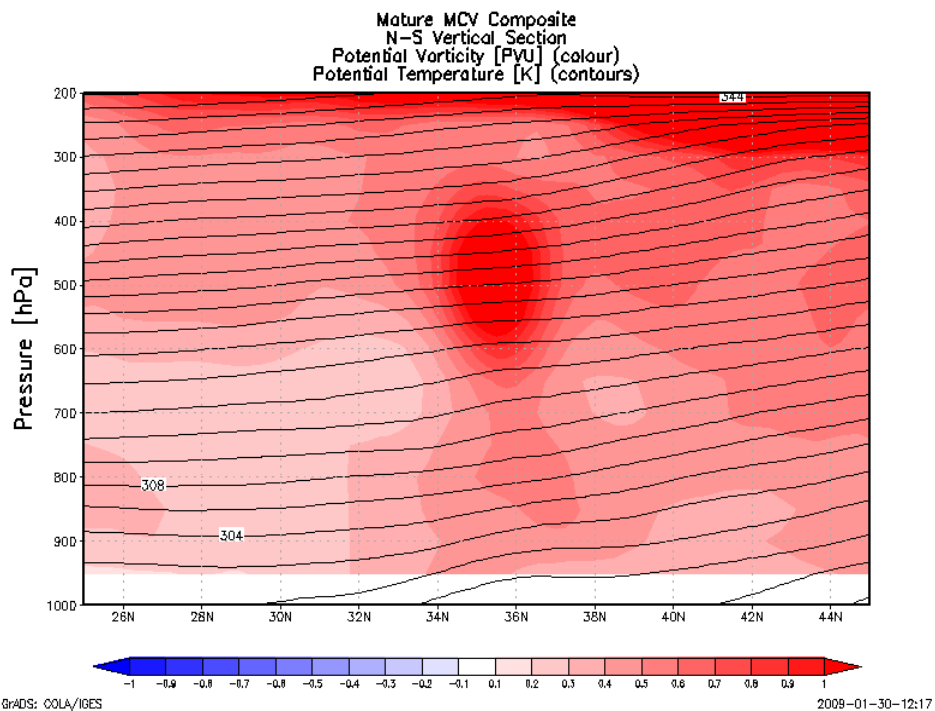


Figure 4.32: Mature MCV composite (for MCV at 35.5°N) north-south cross-section of potential temperature (K; contour interval 2 K) and potential vorticity (colours; PVU).

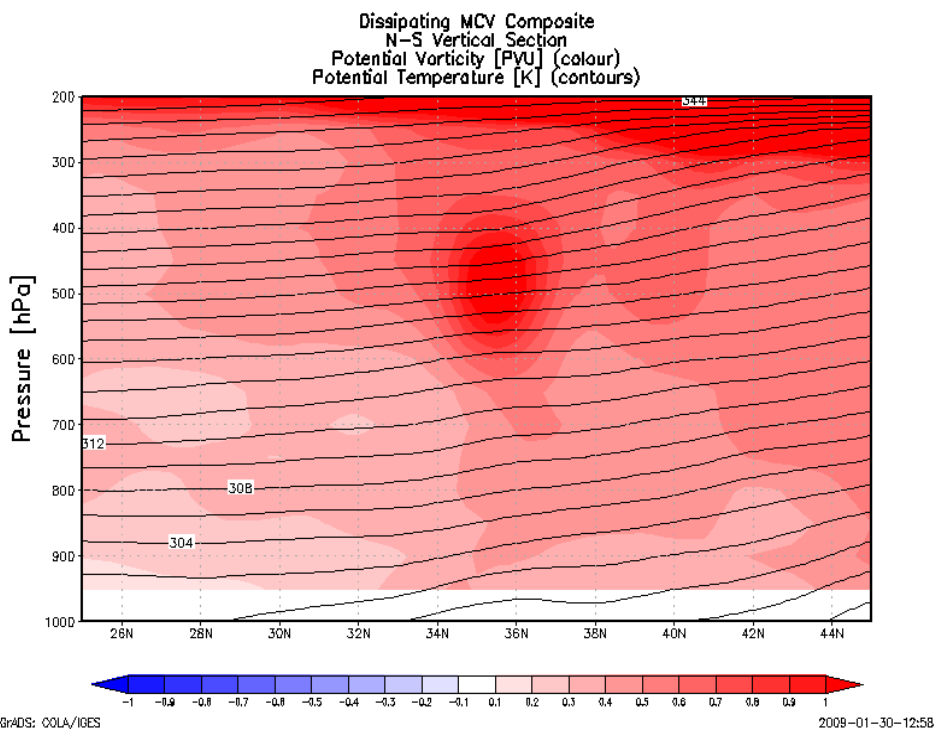


Figure 4.33: Dissipating MCV composite (for MCV at 35.5°N) north-south cross-section of potential temperature (K; contour interval 2 K) and potential vorticity (colours; PVU).

below the MCV. The mature MCV composite shows a further intensification of the MCV, with a relatively deep stable layer from ~600-400 hPa, and a PV maximum of more than 1.3 PVU at 500 hPa. Cyclonic PV does extend downward somewhat towards the surface, but this extension remains relatively broad and weak in the composite. The dissipating composite shows that the MCV has weakened by this time, although a mid-level PV maximum persists.

c. Summary

An analysis of several characteristics of the population of MCVs detected by the RUC algorithm used here reveals a mid-latitude MCV climatology that is broadly consistent with previous studies. The MCVs tend to form within the stratiform regions of MCSs, many of which are nocturnal (including MCCs). The maturity of most MCSs during the night leads to a strong nocturnal maximum in MCV initiation at this time of day. The MCVs documented here last for a greatly varying amount of time after their initiation, occasionally up to 48 h or more. MCVs which generate secondary convection at some point during their lifetime tend to be longer-lived than those that do not. The sizes of the vortices recorded here, averaging ~225 km, is ~40 km larger than found in a previous study by Davis et al. (2002); both studies agree that MCV radii are generally below 300 km. The maximum 600-500 hPa relative vorticity attained during the MCV

events varies between $2 \times 10^{-5} \text{ s}^{-1}$ and $2 \times 10^{-4} \text{ s}^{-1}$. The MCV tracks show a variety of orientations, but all have an easterly component to their motion. For the 28 cases containing a significant surface mesolow, the low tends to be located near and slightly south of the MCV centre.

The synoptic-scale environment of the MCVs is further examined through the construction of a composite MCV. Although there is much variability among the cases, MCVs tend to initiate downstream of a mid-level ridge and upstream of a mid-level trough, in agreement with Bartels and Maddox (1991). At MCV initiation, several features of the parent MCS appear, including upper-level divergence associated with an ageostrophic jet streak, mid-level convergence, and a LLJ at 850 hPa. Later in the MCV life cycle, these features weaken, but a mid-level pressure trough persists until MCV dissipation.

V. MCV TYPES

This section presents the remainder of the results of the study, summarising the repeating patterns of organisation and surface effects observed among the cases investigated. Representative cases of each type are described in detail, along with hypotheses for the physical mechanisms involved in each type.

a. MCV Types

Table 5.1 presents a list of all 45 MCV cases documented in this study, classified according to the types that are defined in this section. Note that the single MCV of the third type, occurring on 29 July 2004, is omitted from Table 5.1. The first repeating pattern of MCV organisation recognised in this study is termed the “collapsing stratiform region MCV”. Eight of these MCVs are documented during the period of study. In these MCVs, a surface mesolow develops, which will be later attributed to large-scale subsidence warming within the dissipating stratiform region of the parent MCS. The second type of MCV recorded here is named the “rear inflow jet MCV”. This type of MCV is the most common: 19 of the 45 cases studied herein adhere to this basic evolution. These MCVs are characterised by a mesolow developing due to concentrated

<i>Type One</i>	<i>Type Two</i>	<i>Type Four</i>	<i>Type Five</i>
15-16 May 2002	17 May 2002	21 May 2003	3 June 2002
24 August 2002	4-5 June 2002	30 July 2003	9-10 June 2002
23-24 May 2003	27 August 2002	28 July 2004	20-21 June 2003
4-6 June 2004	24-25 May 2003		24-25 June 2003
5 July 2004	3 June 2003		29 June-1 July 2003
9-10 August 2004	12 June 2003		11-12 May 2004
30-31 August 2004	21 June 2003		6-8 June 2004
19 May 2005	2 August 2003		19-20 June 2004
	9-10 August 2003		30 June-1 July 2004
	3-4 June 2004		1-2 July 2004
	20-21 June 2004		16-17 July 2004
	11-12 August 2004		6 August 2004
	20-21 August 2004		15-16 August 2004
	28-29 August 2004		6-7 June 2005
	13 May 2005		
	10 June 2005		
	17 June 2005		
	1-2 July 2005		
	2 July 2005		

Table 5.1: Classification of all 45 MCV cases documented in this study. Note that only one Type Three MCV was observed (29 July 2004).

subsidence warming within a descending rear inflow jet in a strong MCS, as will be shown later. The third kind of MCV seen among the cases examined is termed the “surface-penetrating MCV”. Only one of the cases documented here displays this type of pattern. In this case, the MCV appears to penetrate to the surface, leading to a large and strong surface mesolow and a well-defined surface cyclonic circulation. The last two types of MCVs contain no significant surface mesolow. The fourth type is called the “cold pool dominated MCV”, of which three are documented in Oklahoma during the period of study. The fifth and final type of MCV observed in this study is called the “remnant circulation MCV”. This type of MCV evolution appears to be relatively common; 14 of the 45 cases studied herein display this behaviour.

b. Collapsing Stratiform Region MCV

The first type of MCV observed is termed the “collapsing stratiform region MCV”, due to the apparent role of the dissipating stratiform region in the development of a surface mesolow. Several interesting features emerge in the climatology of these events. Figure 5.1 shows the mean radius of the five MCV types identified here at the four different life cycle stages (initiation, development, maturity, and dissipation). In the mean, collapsing stratiform region MCVs (Type one) appear smaller in scale than the other MCV types examined here. Figure 5.2, which shows the mean mid-level relative

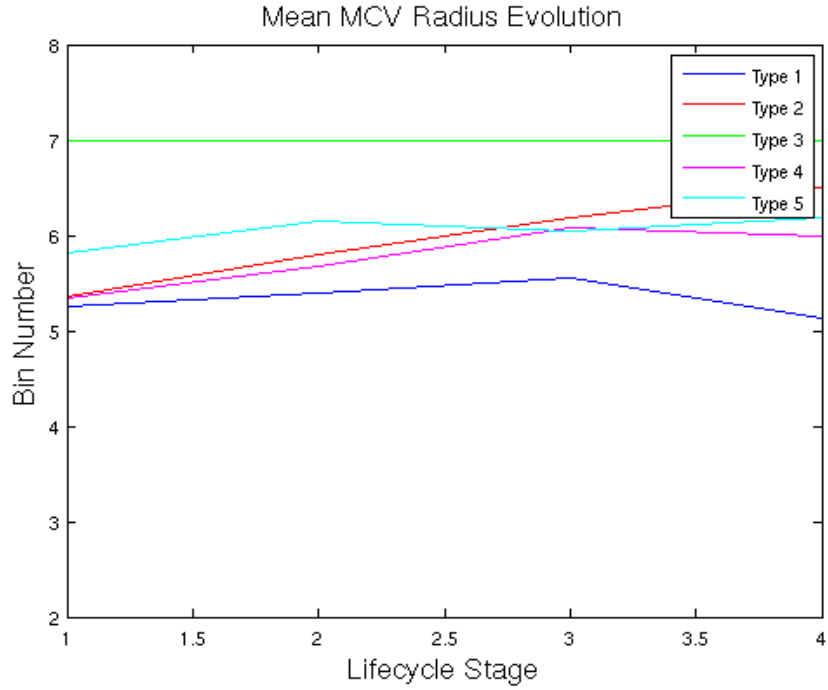


Figure 5.1: Mean MCV radius evolution by MCV type. Life cycle stage one corresponds to initiation, two: development, three: maturity, and four: dissipation. Colours indicate the five MCV types identified in this study, as described in section 5a.

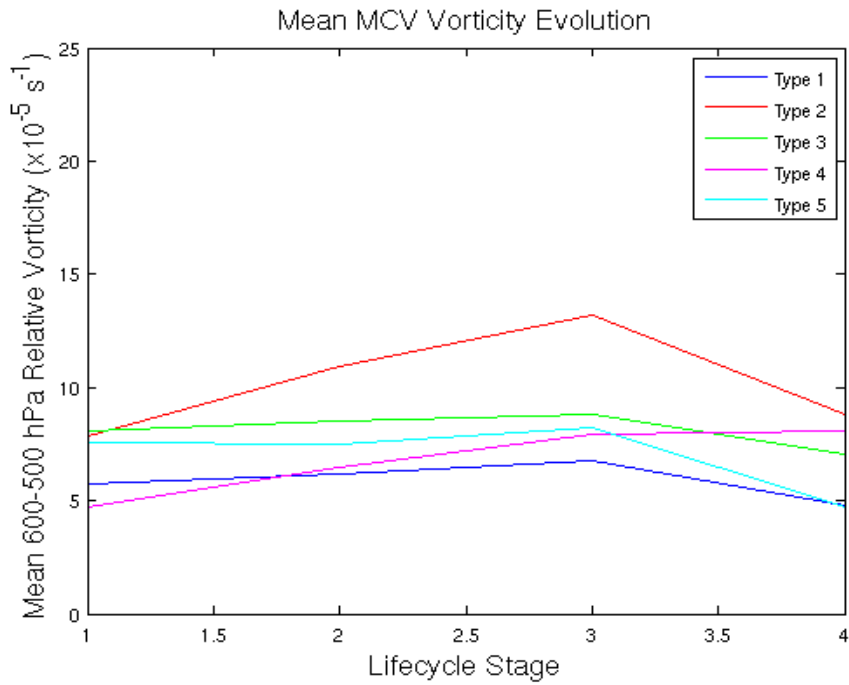


Figure 5.2: As in Figure 5.1, but mean MCV 600-500 hPa relative vorticity ($\times 10^{-5} \text{ s}^{-1}$).

vorticity at each of the four times, reveals that these MCVs are also significantly weaker than the other types. The reduced radius and intensity of these MCVs is likely related to the relatively small size of the parent MCS in each case.

The eight collapsing stratiform region MCV cases examined here all follow a similar evolution. The small initial MCS is characterised by a broad mesohigh at the surface (due to cooling from precipitation). Interestingly, the MCSs have a preference for southeastward movement (six of the eight cases move south or southeast; see Figure 5.3), and tend to exhibit a similar reflectivity structure consisting of a small, disorganised convective region, with stratiform precipitation off to the left of the system movement. This is similar to the “parallel stratiform” organisation of Parker and Johnson (2000), but the convection is not always in a well-defined line or oriented perpendicular to system motion. After the peak intensity of the MCS convection, the mesohigh, initially centred within the stratiform region, shifts towards the front of the precipitation, and then out ahead of the precipitation. Meanwhile, a mesolow begins to develop at the rear of the now-dissipating stratiform region. This behaviour has not been documented heretofore, although pre-squall mesohighs have been reported prior to bowing in the bow echo cases studied by Adams-Selin and Johnson (2008). Over the next few hours, during which the associated MCV is first detected, the stratiform region of the MCS dissipates, the mesohigh weakens, and the mesolow moves forward into the dissipating stratiform

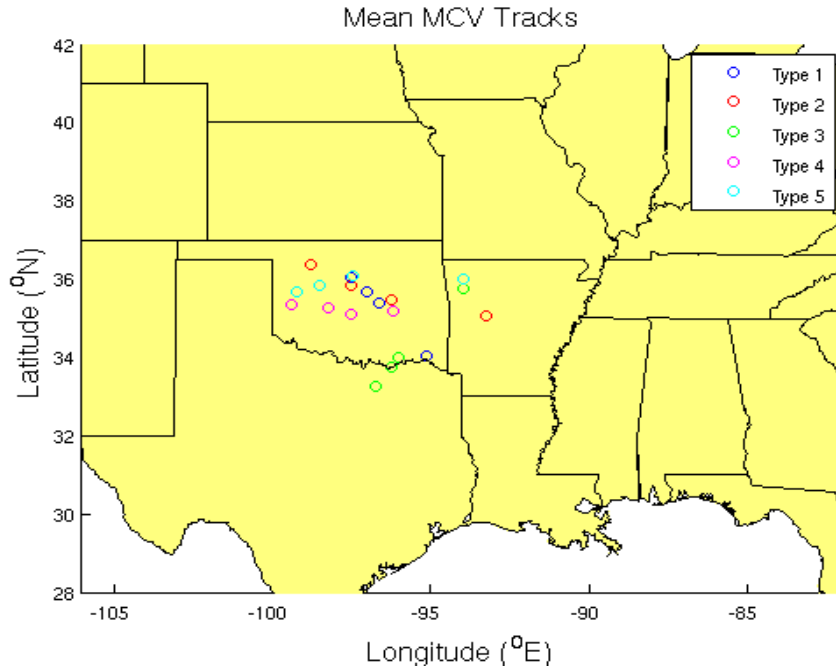


Figure 5.3: Mean MCV tracks by MCV type. All MCV tracks proceed from west to east, with four positions corresponding to the four life cycle stages. Colours indicate the five MCV types identified in this study, as described in section 5a.

region and becomes quite broad and deep. Typically, the mesolow begins to weaken after the dissipation of all precipitation associated with the MCS, although the MCV persists for a while longer. Figure 5.4 shows the mean movement of the mesolow relative to the mid-level MCV centre for these cases, compared to the other MCV types identified. The mesolow position at MCV dissipation could only be determined for one of the eight cases, so the mean position at this time is not robust. The mean mesolow position in these collapsing stratiform region MCVs does appear closer to the MCV centre than in the other MCV types. However, there is a large amount of variability in the mesolow locations from case to case. Additionally, there is some uncertainty in the

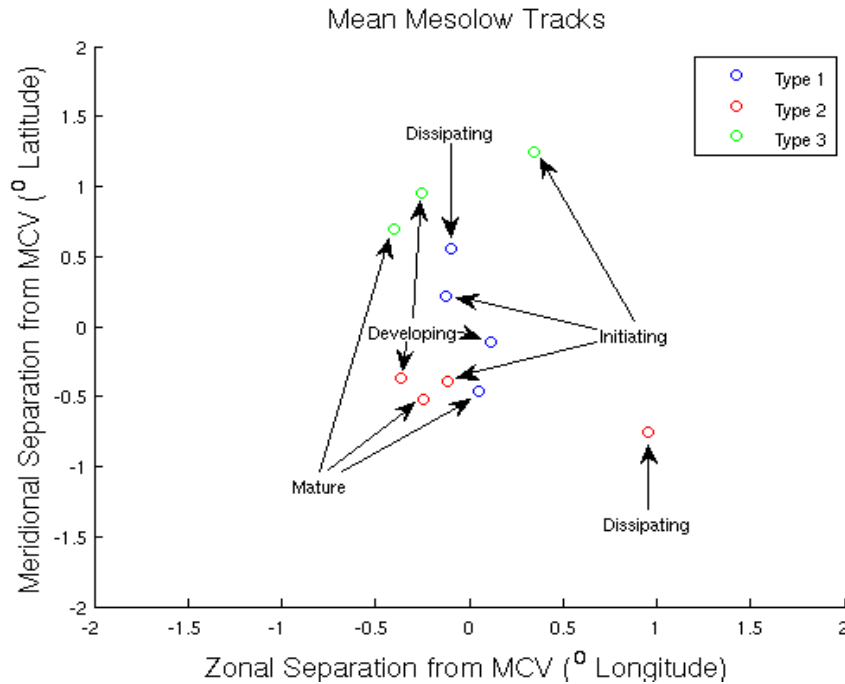


Figure 5.4: Mean mesolow tracks with respect to 600-500 hPa MCV centre, by MCV type. Colours indicate the five MCV types identified in this study, as described in section 5a.

location of the MCV centres due to the coarse resolution of the RUC analyses. These limitations preclude any statistically significant statements about the proximity of the mesolow to the mid-level vortex in these collapsing stratiform region MCVs.

The typical sequence of events followed by collapsing stratiform region MCVs is illustrated for one of the cases documented here, occurring on 9-10 August 2004. Figure 5.5 shows the composite radar reflectivity and surface pressure as the MCS is just entering northwestern Oklahoma. The radar reflectivity shows a fairly strong stratiform region centred just north of the Kansas-Oklahoma border, with a significant mesohigh

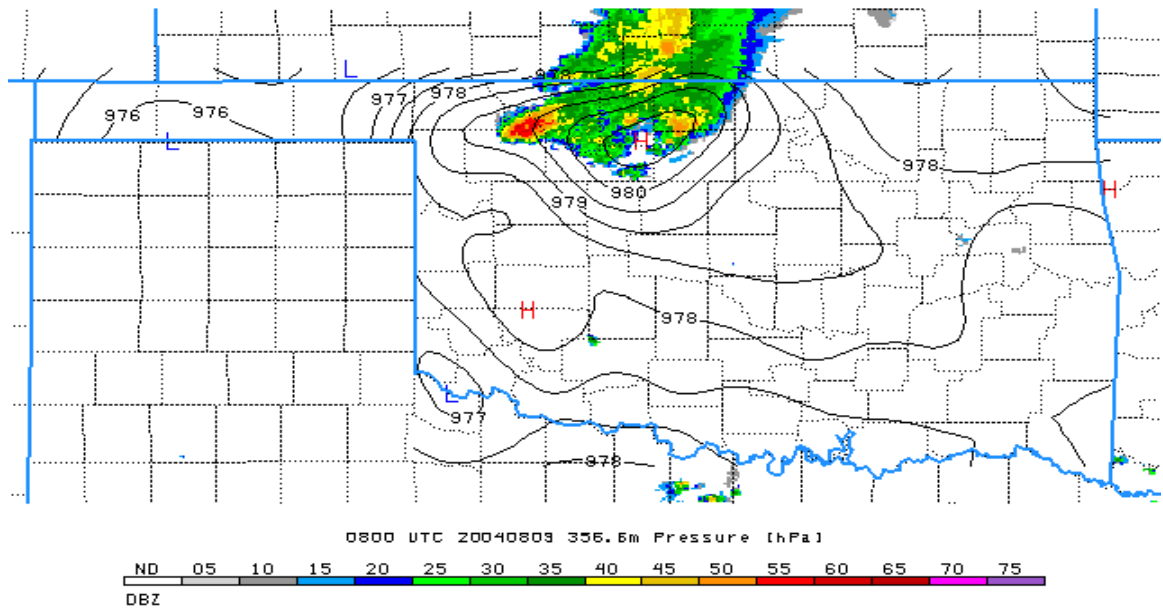


Figure 5.5: Surface pressure analysis (hPa; contour interval 0.5 hPa) of Oklahoma Mesonet overlaid on NEXRAD composite radar reflectivity (colours; dBZ) at 0800 UTC on 9 August 2004. Pressure is adjusted to 356.6 m.

located on the southern fringe of the precipitation. The convective region is confined to a single large cell on the southwestern side of the MCS. An hour later (Figure 5.6), the stratiform region is in the process of dissipating, and the mesohigh has moved farther south, while a pronounced pressure gradient is beginning to appear within the southern portion of the dissipating precipitation shield. It appears there is a mesolow located just north of the border. By 1000 UTC (Figure 5.7), the mesohigh is centred south of the remaining rain area, and a broad mesolow has developed to its north. The mesolow is

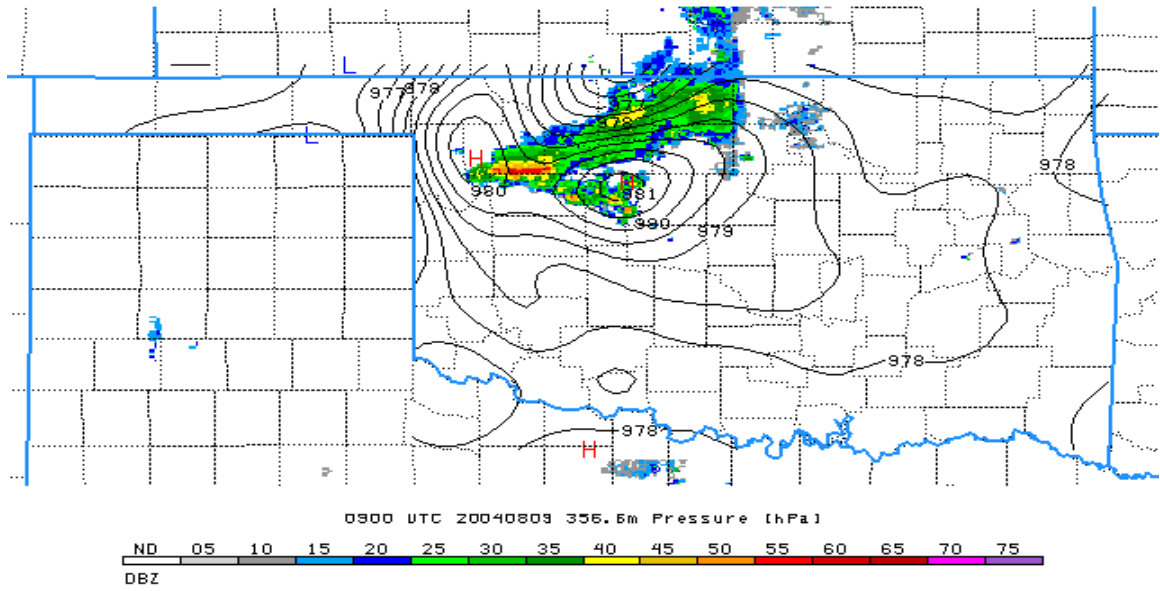


Figure 5.6: As in Figure 5.5, but at 0900 UTC on 9 August 2004.

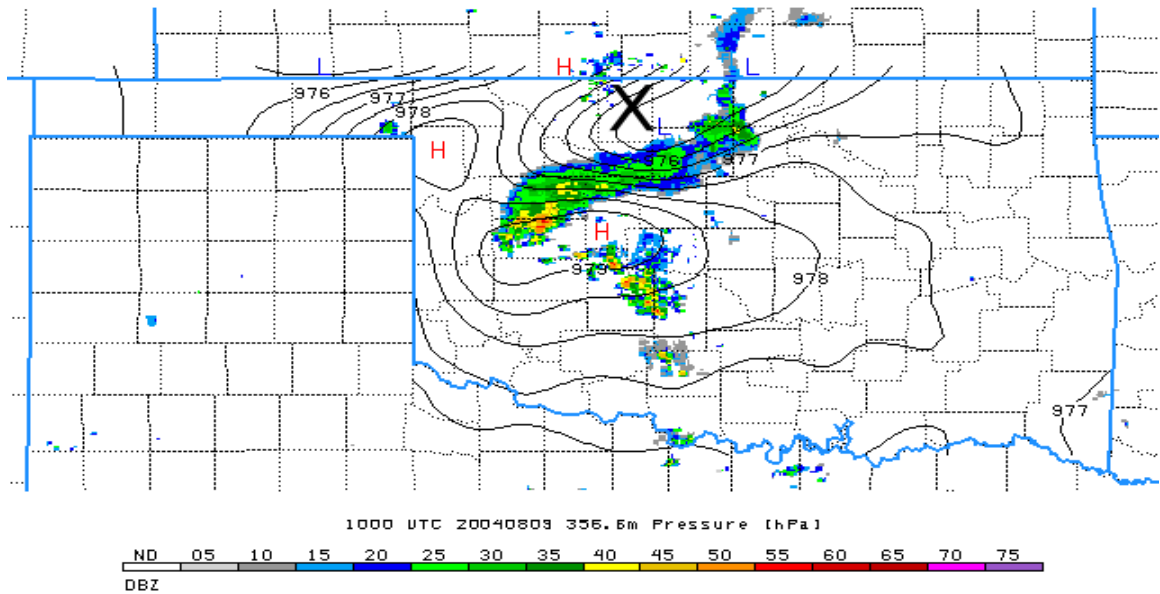


Figure 5.7: As in Figure 5.5, but at 1000 UTC on 9 August 2004. The X shows the location of the mid-level vortex.

approximately centred behind the largely dissipated stratiform region. The MCV associated with the system is first detected by the objective algorithm at this time, located directly over the southern portion of the mesolow; its position is marked in Figure 5.7. By 1100 UTC (Figure 5.8), the stratiform precipitation has completely dissipated, leaving a large and relatively deep mesolow centred in northern Oklahoma and a weakening mesohigh to its south. At later times, the mesohigh and the mesolow continue to move slowly southward, gradually weakening (not shown). The surface wind field, shown in Figure 5.9 at 1100 UTC, shows light and variable winds, with some indications of weak convergence into the mesolow.

Figure 5.10 shows a meteogram for the Breckinridge mesonet station, located just southwest of the mesolow centre at 1100 UTC. The pressure trace shows the passage of a well-defined mesolow of ~ 4 hPa depth, lasting ~ 3 h and reaching maximum depth at 1100 UTC. While the magnitude of the pressure gradient between the mesohigh and mesolow is fairly significant (~ 6 hPa $(100 \text{ km})^{-1}$), the observed winds at the surrounding mesonet stations remain quite low. This is presumably due to the transient and unbalanced nature of the pressure field, as described by Vescio and Johnson (1992). Another notable feature of Figure 5.10 is the minimal temperature and dewpoint variation during the passage of the mesolow; throughout the early part of the analysis period, the near-surface air remains relatively cool and moist. The evolution of the 9-10 August

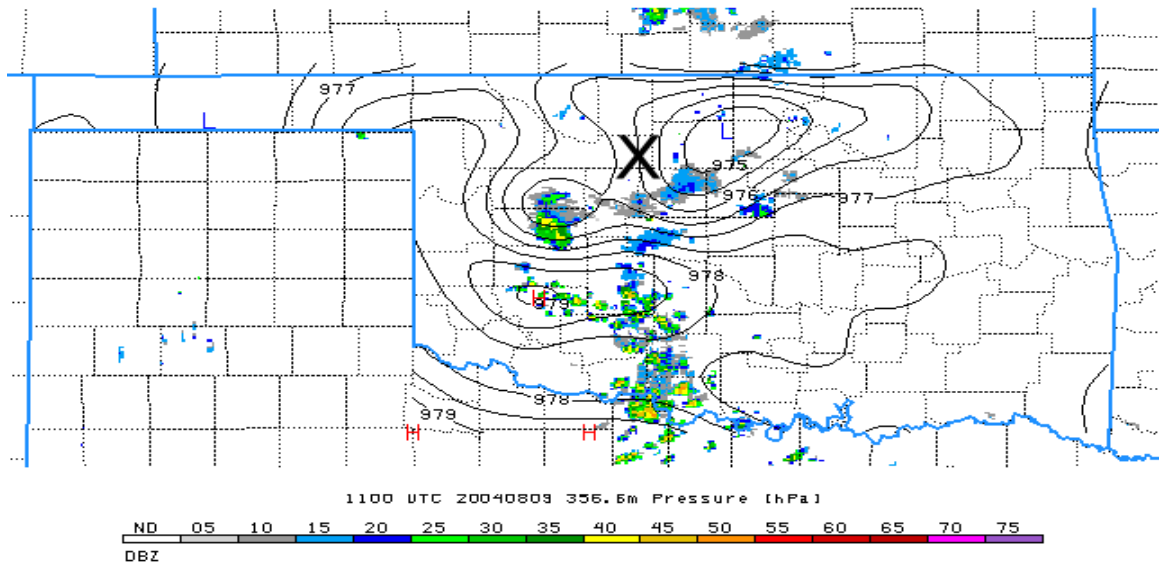


Figure 5.8: As in Figure 5.7, but at 1100 UTC on 9 August 2004.

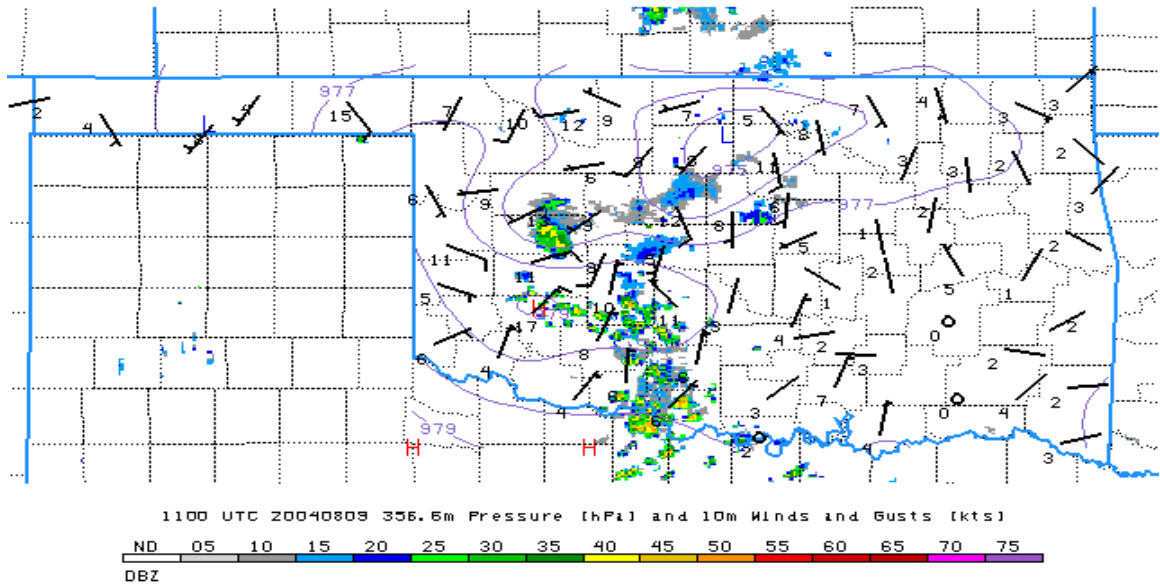


Figure 5.9: Surface pressure analysis (hPa; contour interval 1 hPa) of Oklahoma Mesonet overlaid on observed mesonet 10-m wind barbs and NEXRAD composite radar reflectivity (colours; dBZ) at 1100 UTC 9 August 2004. Pressure is adjusted to 356.6 m.

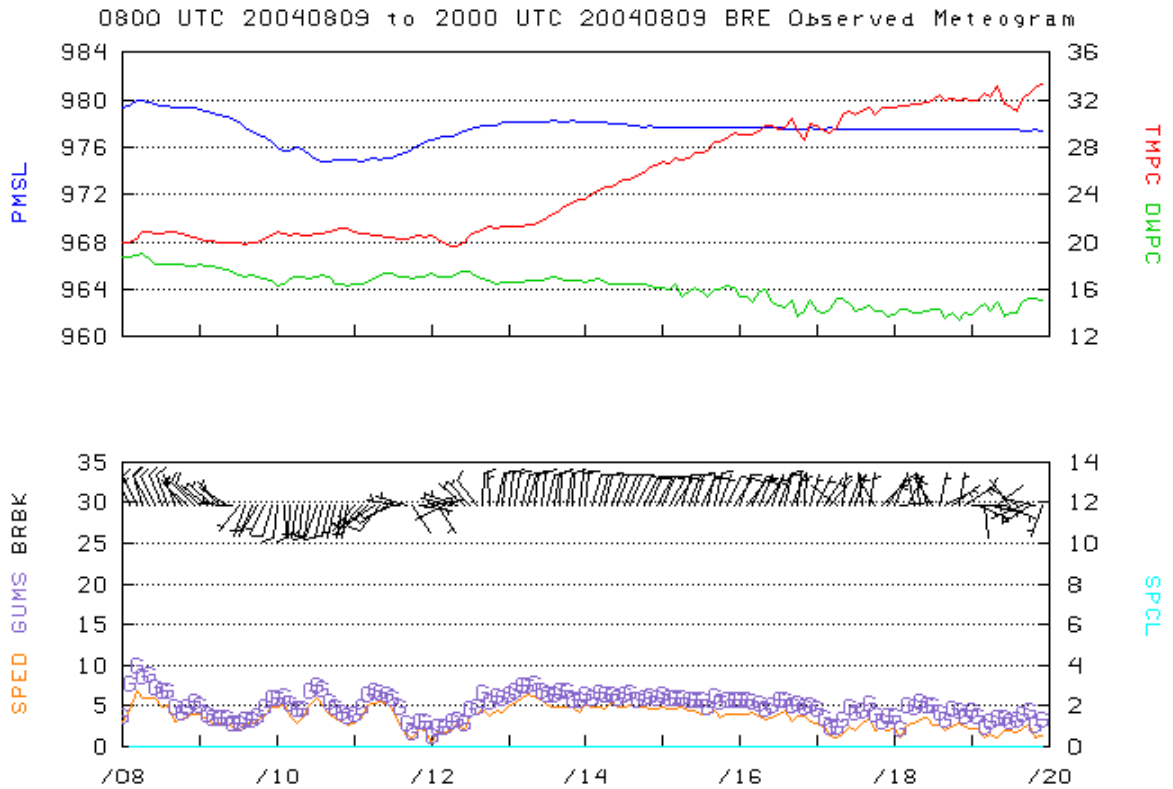


Figure 5.10: Meteogram for Breckinridge mesonet station, 0800-2000 UTC on 9 August 2004. Time runs from left to right. Upper panel displays surface pressure (blue; left axis; hPa) adjusted to 356.6 m, 1.5-m air temperature (red; right axis; °C), and 1.5-m dewpoint temperature (green; right axis; °C). Lower panel displays observed winds (black barbs), wind speed (orange; left axis; m/s), wind gusts (purple; left axis; m/s), and 5-minute rainfall (cyan; right axis; mm (5 minutes)⁻¹). See Figure 2.3 for station location (BREC).

2004 case appears very similar to that of the 23-24 June 1985 OK PRE-STORM MCS, described in detail in Johnson et al. (1989). As described in section 1c and illustrated in Figure 1.3, that case also contained a dissipating stratiform region, a mesohigh moving south of the precipitation, a strong mesolow, and a developing mid-level vortex.

Coincidentally, it occurred only ~100 km to the west of the 9-10 August 2004 case just described.

In order to investigate the causes of the surface pressure features associated with these types of MCVs, it is necessary to look above the surface. Figure 5.11 shows a time series of the observations from the Purcell, Oklahoma, wind profiler site during the 9-10 August 2004 case. The virtual temperature anomaly, depicted by colour shading, is calculated as described in section 3b. Note that the Purcell NPN site is located in south-central Oklahoma; thus the mesolow does not move overhead until ~1300 UTC, and is weaker by this time (not shown). Around the same time as the mesolow passage, the RASS virtual temperature anomalies show a well-defined, broad, and deep maximum. The warm anomaly extends from ~850 hPa up to near the top of the RASS measurements (575 hPa). The anomaly lasts ~2 h, and has a maximum perturbation of ~2 K. This virtual warming is hydrostatically consistent with relatively low pressure at the surface. Direct calculation of the hydrostatic pressure change associated with the changed RASS virtual temperature profile from 1100 to 1300 UTC below 600 hPa gives a value of -1.75 hPa. The observed pressure drop at Washington (WASH; see Figure 2.3 for location), the nearest mesonet station to the Purcell NPN site, is 1.52 hPa over the same two-hour period. This suggests (assuming no compensating temperature changes aloft) that the subsidence warming observed below 600 hPa can explain the entirety of the pressure fall.

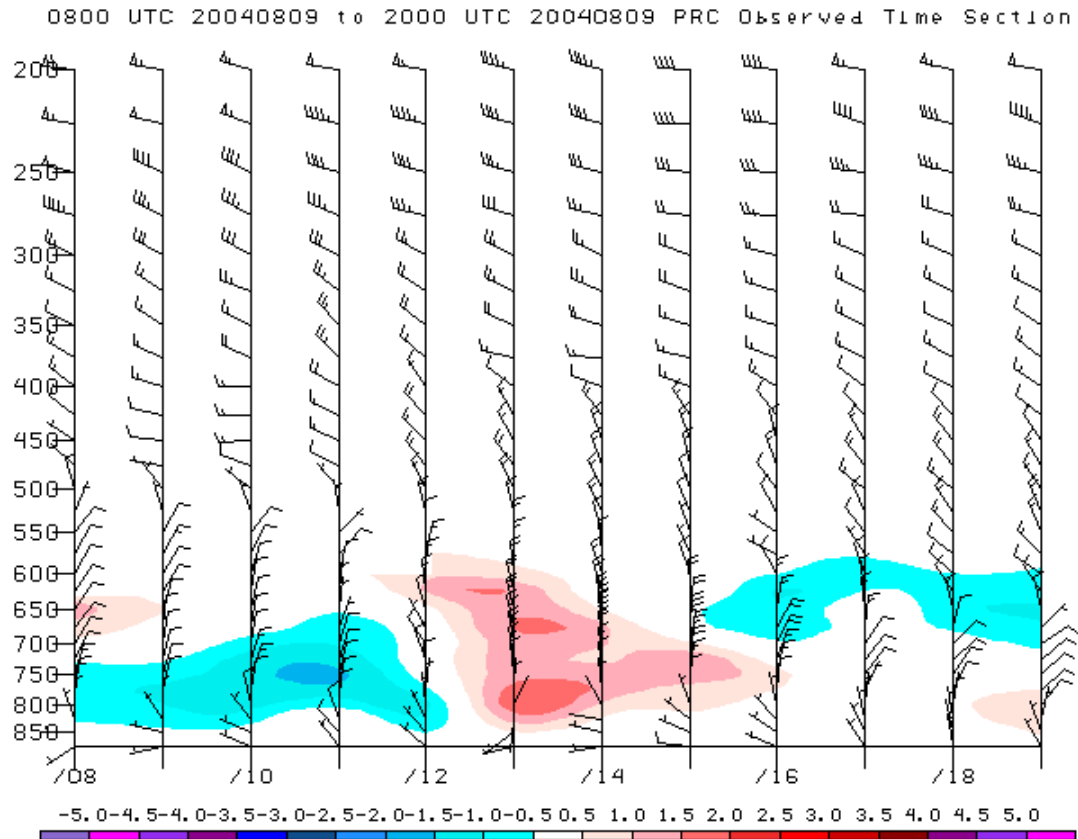


Figure 5.11: Observed time-height section for Purcell, Oklahoma, NPN site, 0800-1900 UTC on 9 August 2004. Time runs from left to right. Barbs indicate horizontal wind speed and direction. Colours indicate RASS virtual temperature anomalies (K). See Figure 2.2 for station location (PRCO2).

It seems probable that the virtual warmth is a result of broad subsidence warming, which could occur within the dissipating remnants of an MCS. After the dissipation of all the precipitation within the MCS stratiform region, continuing subsiding motion would produce adiabatic warming within a stably stratified atmosphere. Subsidence within a dissipating stratiform region would occur over a broad region, resulting in a virtual temperature pattern similar to that observed in this case. Support for this

hypothesis is presented in Figure 5.12, which shows a skew-T/log-p plot of a sounding taken from the ARM SGP site in northern Oklahoma at 1136 UTC. Note that at this time the mesolow is centred nearby. Above a low-level nocturnal inversion, there is a deep dry adiabatic layer extending up to above 700 hPa. This dry adiabatic layer resembles the “onion” soundings documented by Zipser (1977) in the trailing stratiform regions of tropical MCSs. At this time of day, this layer likely represents a region of subsidence warming, particularly considering the absence of any such well-mixed layer in the nearby 1200 UTC Norman, Oklahoma sounding (not shown). The presence of a shallow cool and moist near-surface layer agrees with the surface temperature and dewpoint observations shown in Figure 5.10.

Taken together, these observations strongly suggest that the well-defined mesolows observed in these types of MCVs are due to broad low- to mid-level subsidence warming occurring within the dissipating stratiform regions of MCSs. The frequent close proximity of the surface mesolow and the mid-level vortex (shown in Figure 5.4) suggests there could be a dynamical link between the two. From the perspective of the vorticity equation, low- to mid-level subsidence, such as that producing the mesolows in these systems, would contribute to the spin-up of vorticity by the stretching (or convergence) term. In a favourable environment of weak cyclonic vorticity, this contribution could be a major factor in producing an MCV.

Skew-T, Log(P)

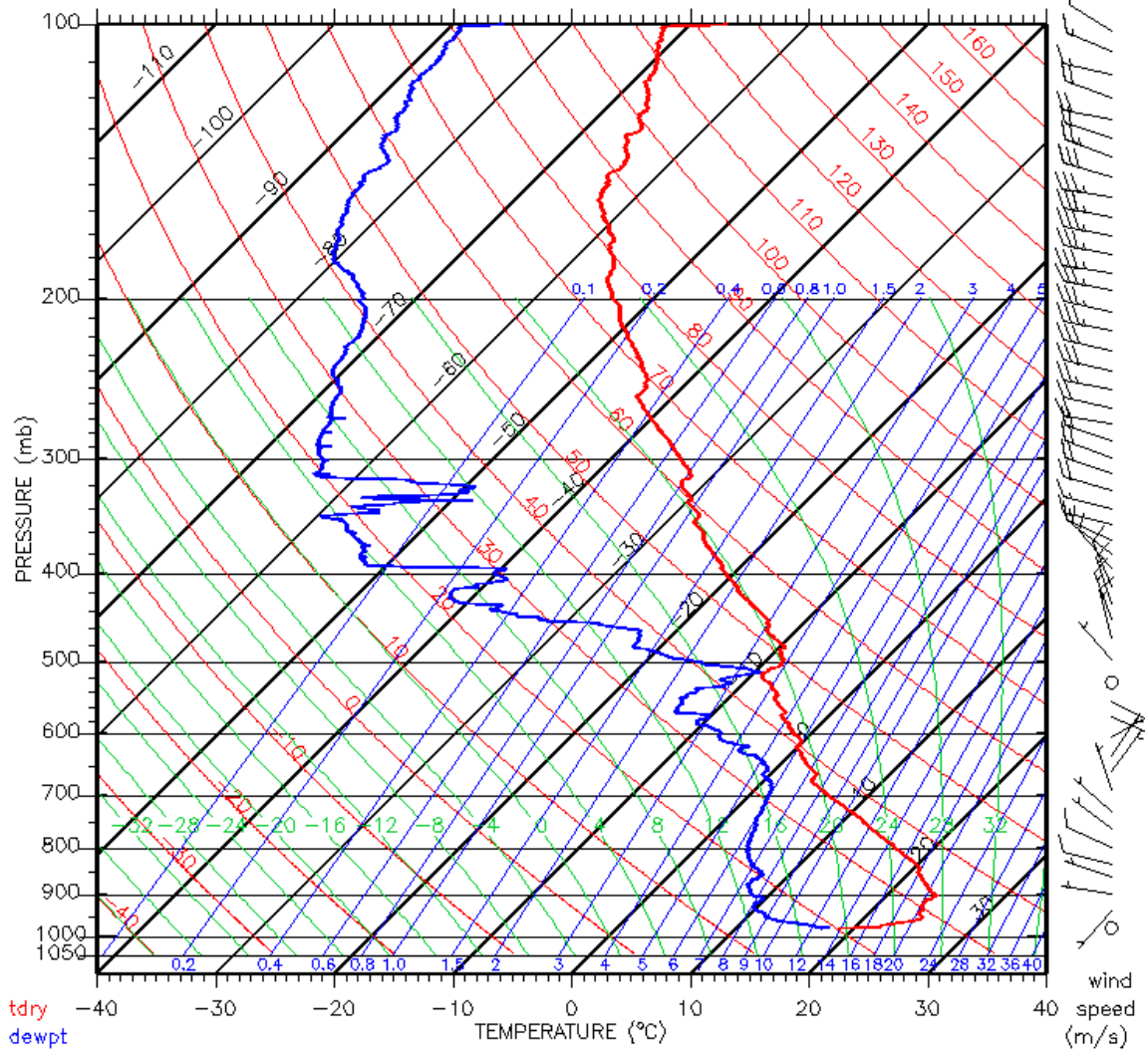


Figure 5.12: Skew-T/log-p plot of radiosonde from ARM SGP site at 1136 UTC on 9 August 2004. See Figure 2.2 for station location (co-located with NPN station LMNO2).

c. Rear Inflow Jet MCV

The second kind of MCV repeatedly seen in this study is referred to as the “rear inflow jet MCV”. These types of MCVs, several of which have been documented in previous studies (e.g., Brandes 1990, Brandes and Ziegler 1993, Knievel and Johnson 2002), generally conform to the conceptual model of Houze et al. (1989) in which the vortex spins up within the stratiform region of an asymmetric MCS (Figure 1.1). Figures 5.1 and 5.2 show that these MCVs (Type two) tend to be larger than the collapsing stratiform region MCVs, and that, on average, they are the most intense class of MCVs. The mean track of the mesolows associated with these MCVs (Figure 5.4) is located slightly to the south of the MCV centre, which is believed to be due to the mechanism for these mesolows, to be described in this section. Again, the location of the mesolow at MCV dissipation should be viewed with skepticism as it is only based on two cases.

In rear inflow jet MCVs, the parent MCS tends to be fairly large and intense. The associated MCV is generally first detected while the parent MCS remains quite vigorous. As the MCS begins to wane and the MCV intensifies during the next few hours, the surface pressure field, initially consisting of a strong surface mesohigh, begins to show a mesolow developing at the rear edge of the stratiform precipitation. The back edge of the precipitation shield sometimes becomes deformed into a well-defined rear inflow notch, with the mesolow being located at the apex of this low-reflectivity region. After this, the

parent MCS tends to dissipate, while the MCV persists for a variable amount of time. Meteograms tend to show a sharp mesolow occurring near the time of the cessation of stratiform rainfall.

The MCV of 24-25 May 2003, occurring during the BAMEX campaign, is described in detail here as a representative case of this type of MCV. Figure 5.13 shows the composite radar reflectivity and surface pressure as the parent MCS is approaching northern Oklahoma. It can be seen that the MCS is organised in a rather complex manner. There is an extensive region of stratiform rain in northeastern Oklahoma and southeastern Kansas, while on the south side of this there is a small but intense band of deep convection oriented northeast-southwest. This convective line produced a 33 m/s wind gust at the Red Rock mesonet site a few minutes before this time (see Figure 2.3 for REDR station location). At the surface, there is a well-defined mesohigh on the southwestern end of this convective line. An hour later, at 1500 UTC (Figure 5.14), the convective line has continued to surge southeastward on the western side of the large stratiform region. The reflectivity field shows a developing rear inflow notch to the north of the convection, suggesting the presence of a strong rear inflow jet impinging on the back of the stratiform region behind the convection. The surface pressure field is relatively flat within the MCS, with the exception of the mesohigh remaining at the southwestern end of the convective line. At 1600 UTC (Figure 5.15), the associated

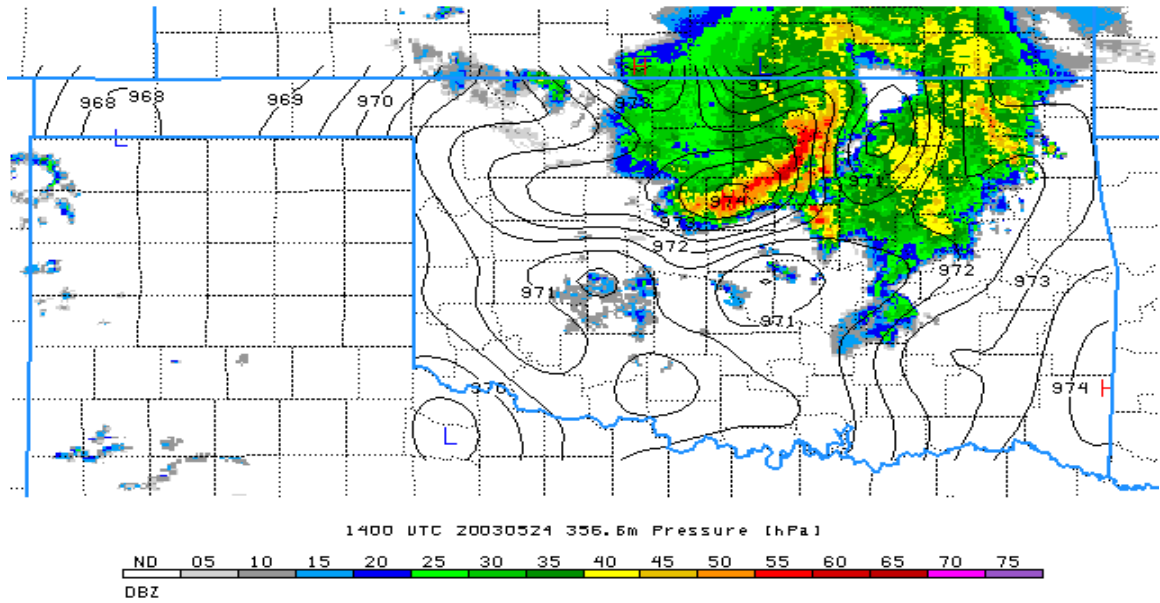


Figure 5.13: As in Figure 5.5, but at 1400 UTC on 24 May 2003.

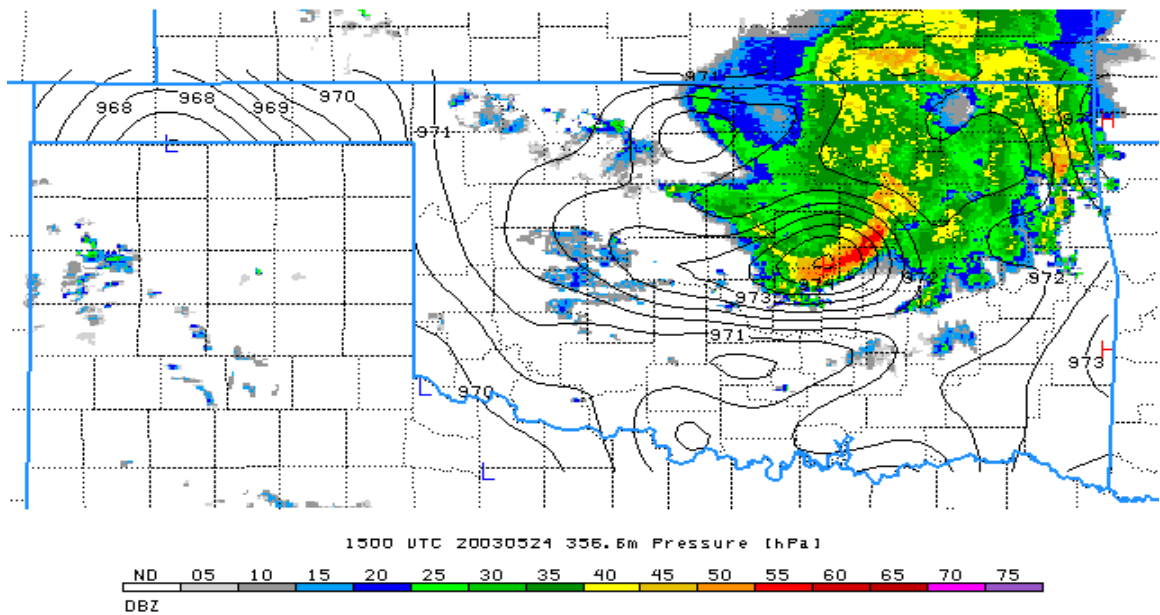


Figure 5.14: As in Figure 5.5, but at 1500 UTC on 24 May 2003.

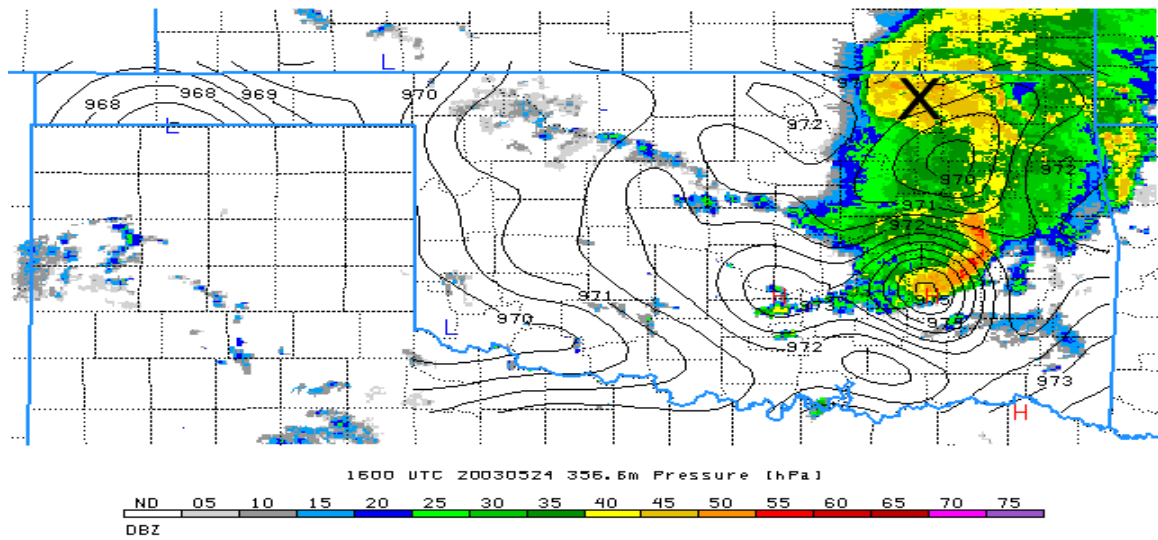


Figure 5.15: As in Figure 5.7, but at 1600 UTC on 24 May 2003.

MCV is first detected by the objective algorithm; its location is marked in the figure. By this time, the convective line is becoming weaker, while the stratiform region is taking on a cyclonically curved shape. South of the MCV, within the stratiform region, a weak mesolow has appeared. The mesolow is centred at the front of the reflectivity gradient associated with the back edge of the stratiform region. By 1700 UTC (Figure 5.16), the mesolow is quite concentrated and deep. The stratiform region appears to be eroded on its back edge to the south of the MCV, and the mesolow is located near the apex of this rear inflow notch. The presence of strong rear inflow is demonstrated in Figure 5.17, which shows the observed NPN winds at the 700 hPa level. The corresponding surface

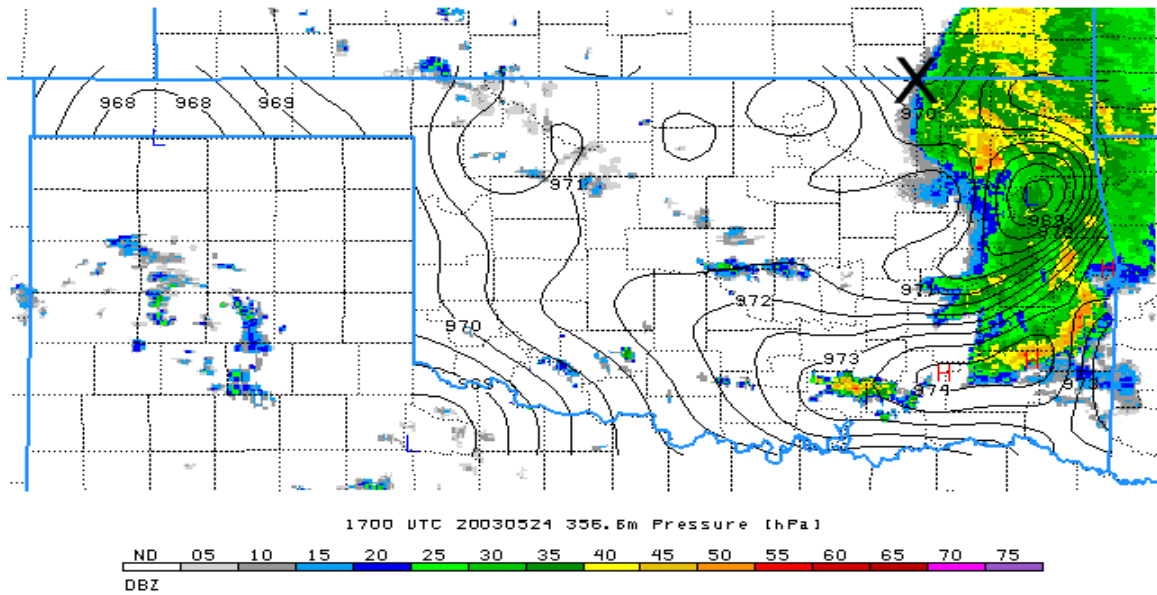


Figure 5.16: As in Figure 5.7, but at 1700 UTC on 24 May 2003.

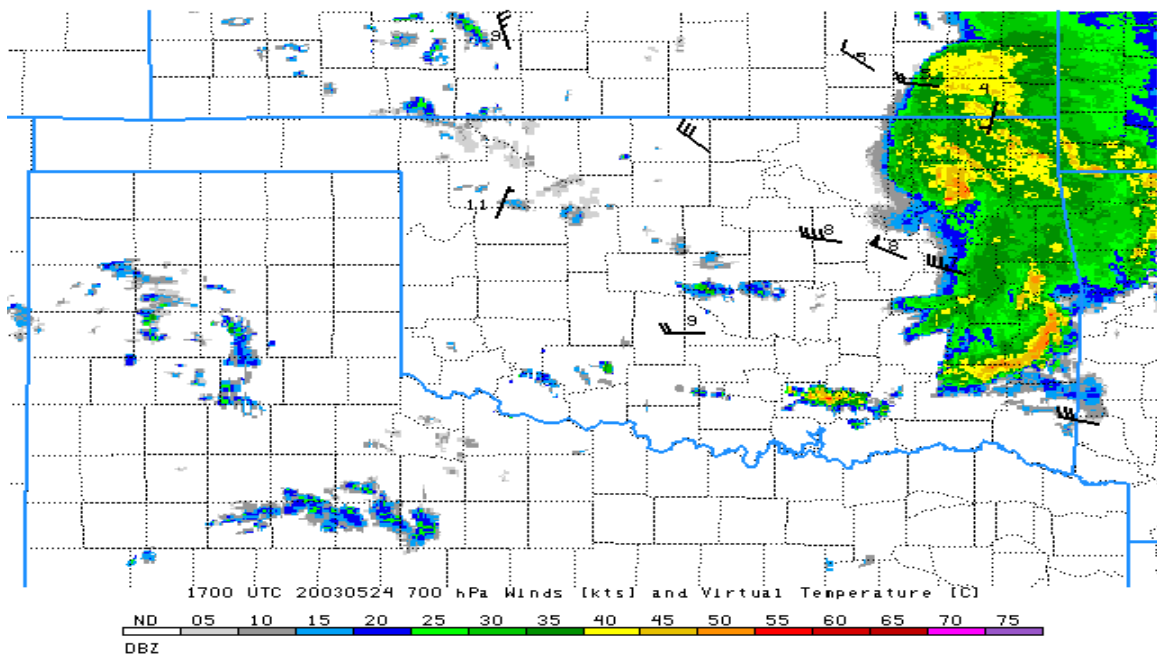


Figure 5.17: Observed NPN 700 hPa wind barbs and RASS virtual temperatures ($^{\circ}\text{C}$) overlaid on NEXRAD composite radar reflectivity (colours; dBZ) at 1700 UTC on 24 May 2003.

winds are shown in Figure 5.18; the strong rear inflow apparently does not penetrate to the surface. At later times, the MCV moves eastward into Arkansas and Missouri (not shown) as the stratiform precipitation gradually dissipates. The MCV remains detectable all the way to extreme eastern Tennessee, where it dissipates at 1500 UTC on 25 May.

Figure 5.19 shows a meteogram for the Tahlequah mesonet station, located near the centre of the mesolow at 1700 UTC. The pressure trace shows a very strong and sharp mesolow passing the station just after 1700 UTC. Meanwhile, the 1.5-m temperature and dewpoint remain nearly constant and quite close together, indicating high relative humidity. If the mesolow is a hydrostatic phenomenon, as will be argued,

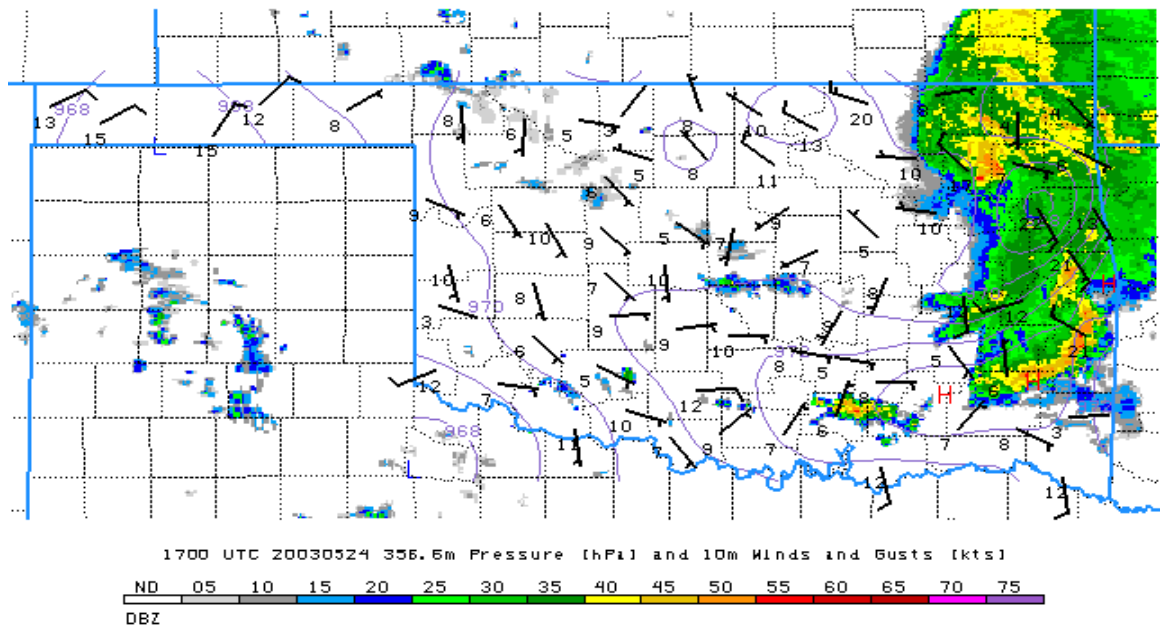


Figure 5.18: As in Figure 5.9, but at 1700 UTC on 24 May 2003.

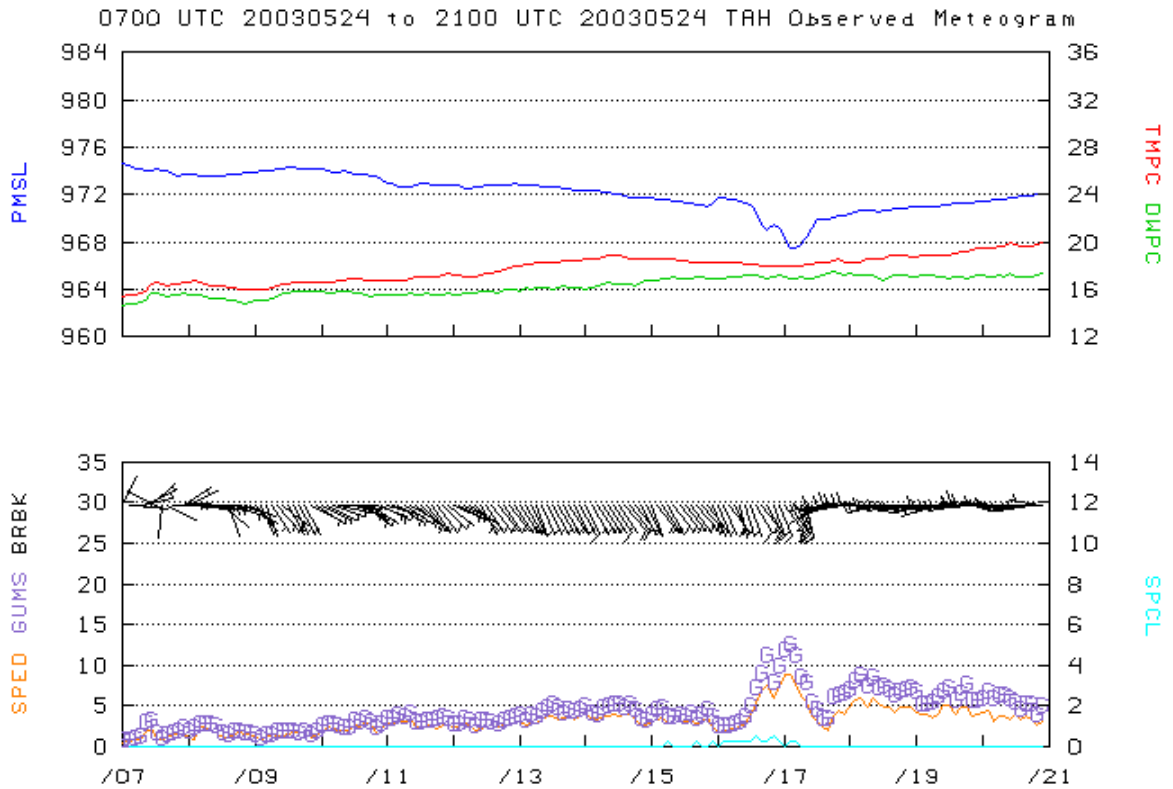


Figure 5.19: Meteogram for Tahlequah mesonet station, 0700-2100 UTC on 24 May 2003. Time runs from left to right. Upper panel displays surface pressure (blue; left axis; hPa) adjusted to 356.6 m elevation, 1.5-m air temperature (red; right axis; °C), and 1.5-m dewpoint temperature (green; right axis; °C). Lower panel displays observed winds (black barbs), wind speed (orange; left axis; m/s), wind gusts (purple; left axis; m/s), and 5-minute rainfall (cyan; right axis; mm (5 minutes)⁻¹). See Figure 2.3 for station location (TAHL).

the associated temperature perturbations must be confined to regions above the surface, similar to the collapsing stratiform region MCVs. The mesolow occurs at the same time as the cessation of the stratiform rainfall, as noted in several other studies (Johnson and Hamilton 1988, Stumpf et al. 1991). In this case, the 10-m winds respond strongly to the

pressure field, increasing in speed to ~9 m/s within the mesolow, and veering sharply from south-southeasterly to west-southwesterly soon after the mesolow passage. Perhaps this wind response is due to the great magnitude of the pressure gradient.

This case appears very similar to the OK PRE-STORM MCS of 6-7 May 1985, as described by Brandes (1990) and Brandes and Ziegler (1993). As shown in Figure 1.4 and discussed in section 1c, that case involved a strong rear inflow jet on the south side of an MCV, leading to a pronounced rear inflow notch with a strong surface mesolow at its apex. Rear inflow notches have also been documented in other MCSs containing MCVs (Smull and Houze 1985, Scott and Rutledge 1995, Chong and Bousquet 1999, Knievel and Johnson 2002).

Once again, to ascertain the reasons for the observed surface pressure features on 24 May 2003, it is necessary to examine observations aloft. Figure 5.20 shows a time-height section of NPN observations from the Haskell, Oklahoma wind profiler during the analysis period. This NPN site is located about 85 km west-southwest of the mesonet station at Tahlequah; this is close enough to observe mesoscale features relevant to the surface observations at Tahlequah. Other nearby mesonet stations, including that at Haskell, record mesolow passage near the same time, although the pressure drops are not as pronounced as at Tahlequah. Note that time runs from right to left in this figure; this is opposite from previous figures. The feature of interest is the pronounced low-level

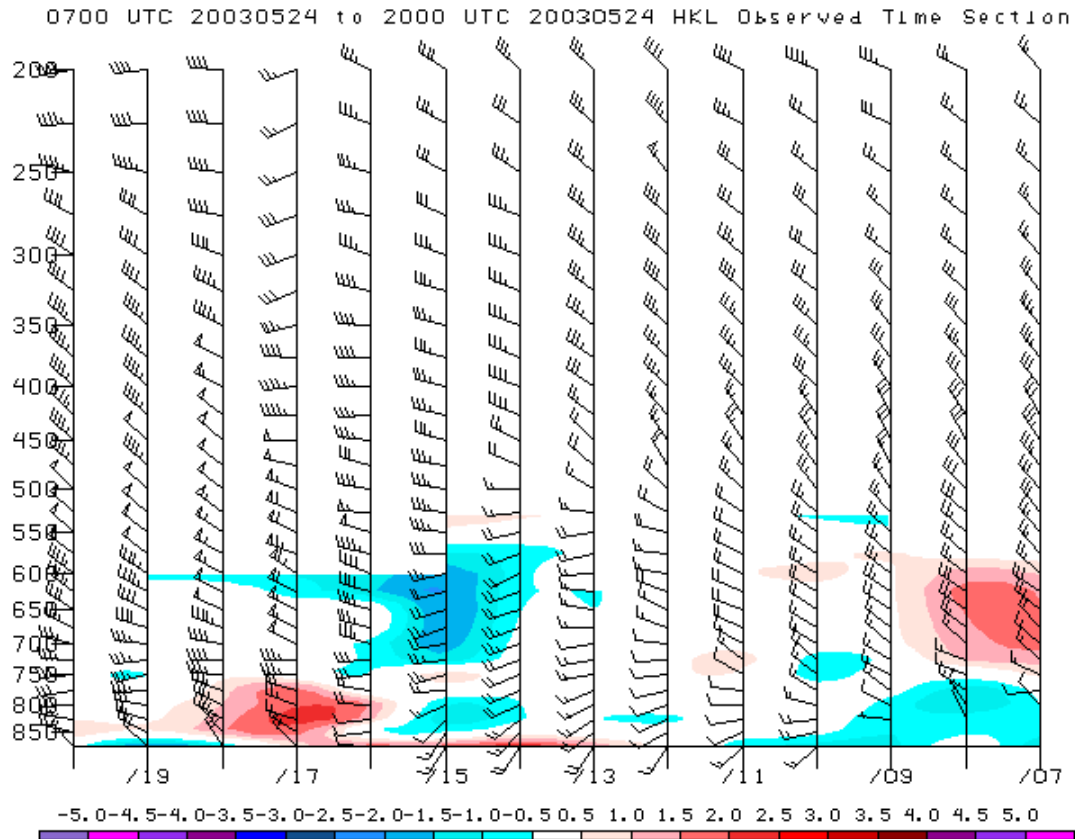


Figure 5.20: Observed time-height section for Haskell, Oklahoma, NPN site, 0700-2000 UTC on 24 May 2003. Time runs from right to left. Barbs indicate horizontal wind speed and direction. Colours indicate RASS virtual temperature anomalies (K). See Figure 2.2 for station location (HKLO2).

virtual warming that occurs over Haskell at ~1700 UTC. The virtual temperature anomaly reaches a peak of 2.24 K at 825 hPa, while positive anomalies extend up to near 750 hPa. This sharp low-level warming is believed to be a manifestation of strong subsidence warming associated with a descending rear inflow jet at the back edge of the stratiform precipitation shield. The profiler wind observations at Haskell support this, with the warming occurring at the base of relatively strong west-northwesterly flow (50

kts at 700 hPa). Note that the core of the jet rises from ~600 to ~500 hPa during 1700 to 2000 UTC, consistent with fixed-point observations of a descending jet within an eastward-moving system.

In order to confirm the primary features seen in the profiler data, Figure 5.21 shows a cross-section of this MCV based on dropsonde observations during BAMEX (from Davis and Trier 2007). This MCV happened to be the focus of IOP 1 during the BAMEX campaign, and dense aircraft observations were taken during the afternoon of 24 May. Figure 5.21 is an east-west cross-section of the system, constructed using the steady-state assumption and valid at 1930 UTC. Note that the orientation of the cross-section agrees qualitatively with a time-height section taken at a single point, with time running from right to left for an eastward-moving system (as in Figure 5.20). Encouragingly, the dropsonde observations show a very similar structure to the profiler observations, including a concentrated warm anomaly of more than 2 K centred at ~850 hPa. The virtual warmth extends up to ~600 hPa and then transitions to a cold anomaly, as in the profiler observations. Also similar to the profiler observations, a region of virtually cool air is seen a few hundred km to the east of the warm anomaly, extending over a deep layer except for a small warm pocket at ~700 hPa. The extent of the agreement between the two completely independent sets of observations is remarkable, and provides confidence in the thermal structure of this MCV.

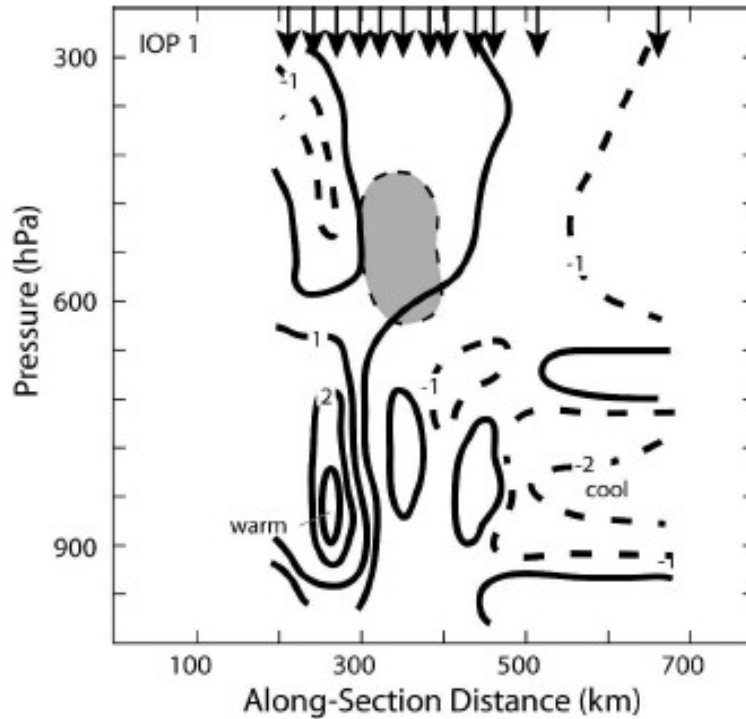


Figure 5.21: East-west cross-section of deviations from average dropsonde profile of virtual potential temperature (K; contour interval 1 K; negative contours dashed) for BAMEX IOP 1 MCV at 1930 UTC on 24 May 2003. Based on dropsonde observations (locations denoted by arrows at top). Grey shaded region represents relative vorticity greater than $1.5 \times 10^{-4} \text{ s}^{-1}$ (from Davis and Trier 2007).

These observations suggest that, in these rear inflow jet MCVs, many of which display similar structure in NPN observations (not shown), the small but intense surface mesolow is a reflection of concentrated low-level subsidence warming occurring within a descending rear inflow jet. For an MCV embedded in westerly flow, the rear inflow and related mesolow might be expected to occur preferentially on the southern side of the vortex; this does appear to be the case, as shown in Figure 5.4. It would be interesting to determine the fate of the mesolow after the dissipation of the rear inflow jet; however, in

the majority of the cases documented here, the MCVs move out of Oklahoma while the rear inflow is still quite vigorous. It is left to future studies to investigate this question.

d. Surface-penetrating MCV

The third kind of MCV seen among the cases examined is termed the “surface-penetrating MCV”. Only one of the cases documented here displays this type of pattern: that of 29 July 2004. The name chosen for this case is appropriate, because it appears to be the only case where the mid-level vortex produces a genuine surface reflection (i.e., an associated low-level vortex). Figures 5.1 and 5.2 show the radius and vorticity evolution of this MCV case, compared with the other MCV types. It can be seen that the radius of this MCV is larger than the mean radii of the other MCV classifications. Radius bin seven corresponds to an average radius of 262 km. The vorticity evolution of this case, however, is unexceptional in comparison with the other MCV types. The northeasterly track of the vortex centre in this case can be seen in Figure 5.3, and the surface mesolow track with respect to the mid-level vortex appears in Figure 5.4. The surface mesolow is initially located northeast of the mid-level vortex, and gradually shifts to the northwest of the vortex centre with time.

The MCV initiates in far northern Texas, subsequently moving northeastward through southeastern Oklahoma until its dissipation in northwestern Arkansas. The

surface mesolow remains in fairly close proximity to the mid-level vortex. The distinguishing feature of this case is the persistent and relatively large-scale surface mesolow attendant to the mid-level circulation. Figure 5.22 shows the precipitation structure and surface pressure field at 1300 UTC on 29 July 2004, as the main rain shield associated with the MCV moves northeastward into Oklahoma. The mid-level MCV centre is just south of the analysis domain at this time. Note that the rain area appears quite disorganised; the strongest radar echoes in the composite reflectivity only reach 40 dBZ, and these regions are distributed throughout the precipitation region. The precipitation appears to be completely stratiform in nature, with the possible exception of some convective showers on the northwestern periphery of the circulation. The MCS which apparently generated the MCV occurred in north-central Texas on the previous afternoon, dissipating before this time. The pressure field at this time shows a large and broad mesolow just southwest of the precipitation shield. An hour later (Figure 5.23), the mesolow has consolidated further, and the entire rain shield is beginning to rotate cyclonically around the mesolow. This rotation is clearly seen when subsequent 15-minute radar images are animated on the computer screen. By 1500 UTC (Figure 5.24), the system has continued to drift slowly north-northeastward into Oklahoma, with the mesolow remaining well-defined. The mesolow and MCV continue drifting through eastern Oklahoma over the next several hours (Figure 5.25), with the mesolow beginning

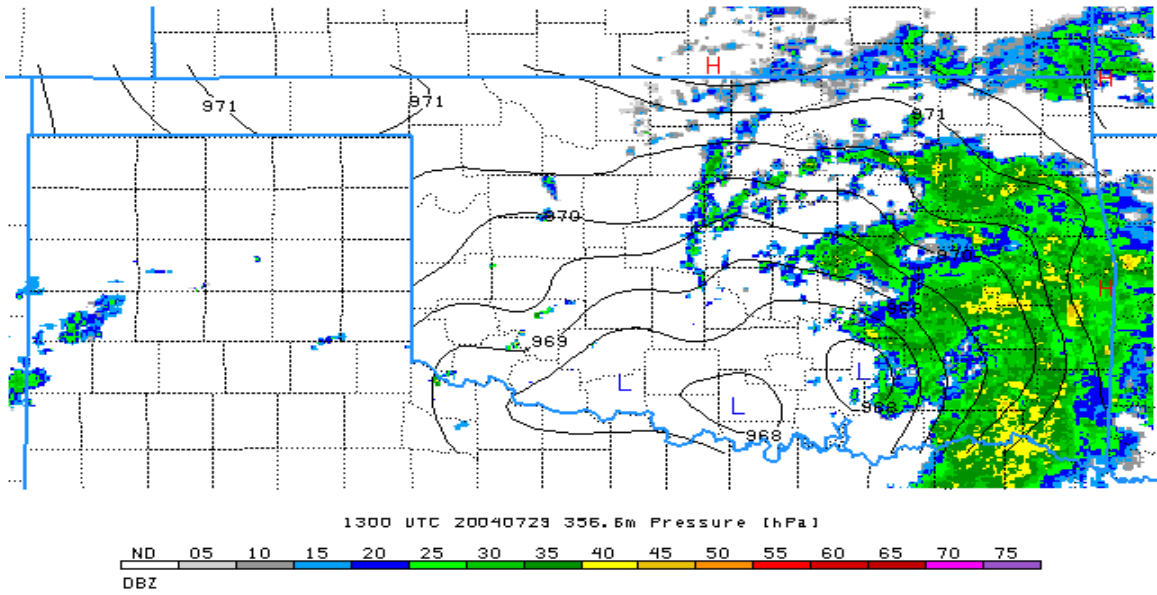


Figure 5.22: As in Figure 5.5, but at 1300 UTC on 29 July 2004.

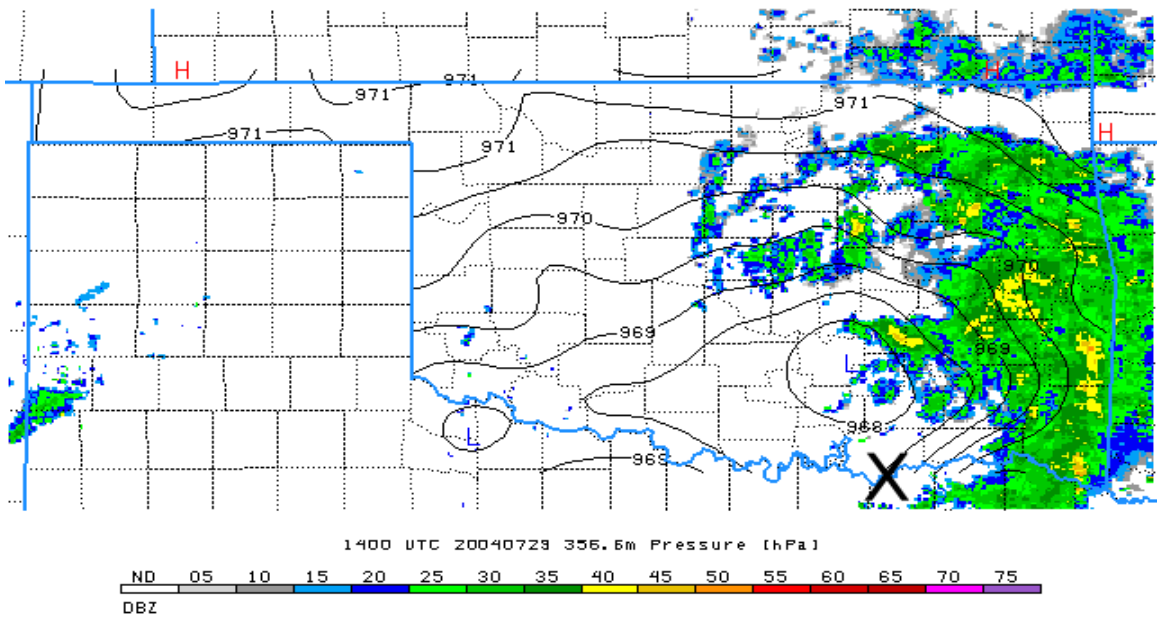


Figure 5.23: As in Figure 5.7, but at 1400 UTC on 29 July 2004.

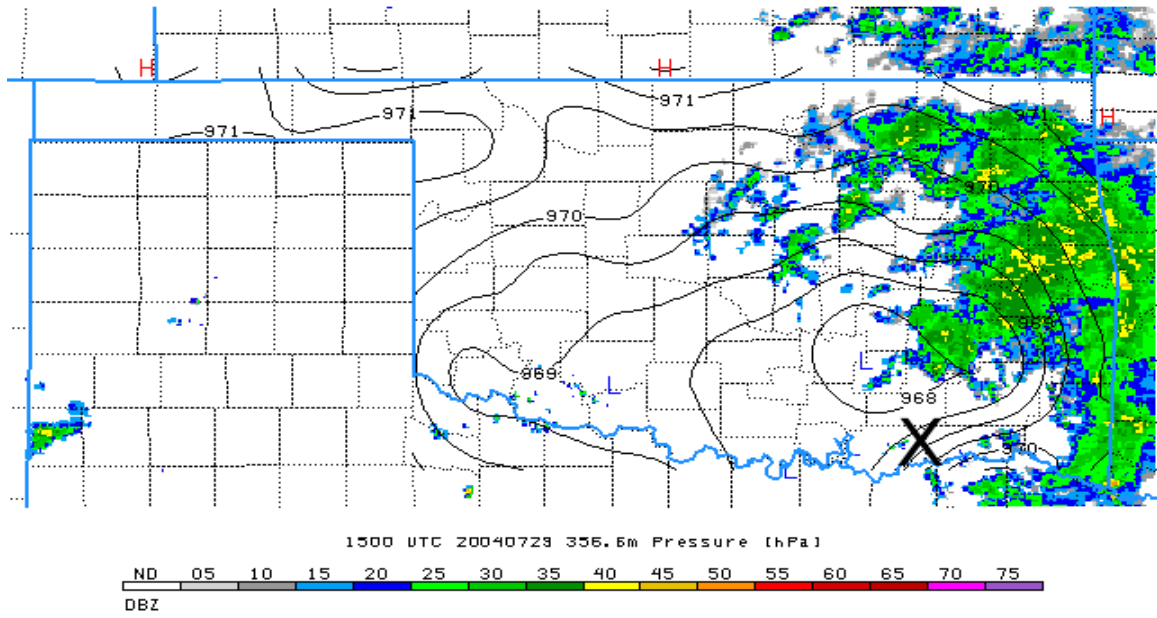


Figure 5.24: As in Figure 5.7, but at 1500 UTC on 29 July 2004.

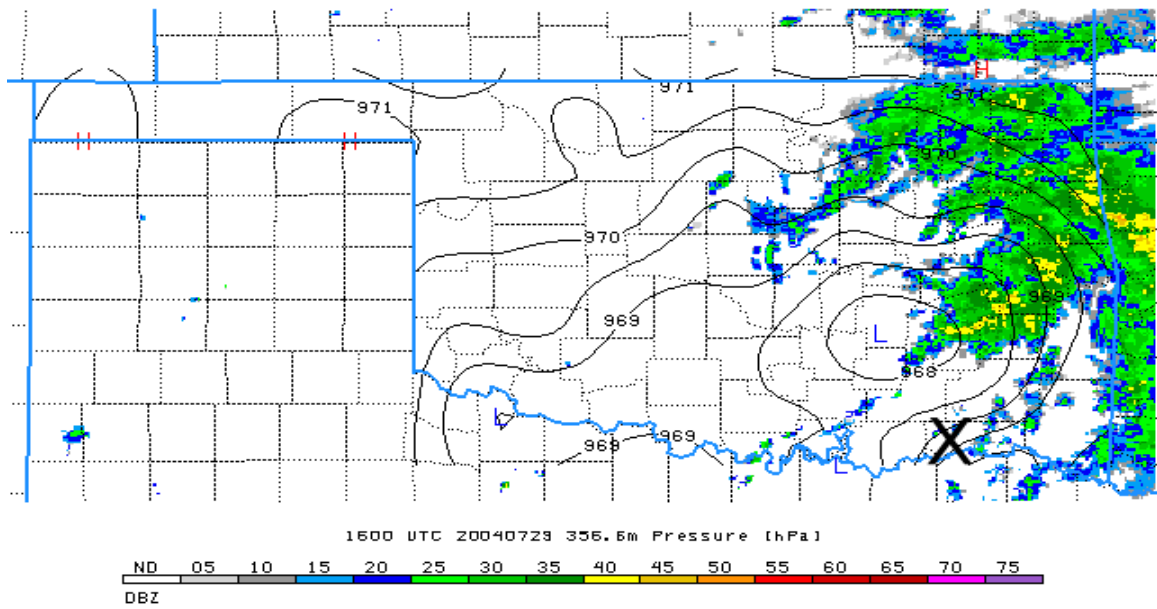


Figure 5.25: As in Figure 5.7, but at 1600 UTC on 29 July 2004.

to weaken and lag behind the MCV in the early afternoon. The MCV finally dissipates at 2200 UTC. It should be noted that, throughout the analysis period, the observed surface winds, although light, form a closed cyclonic circulation, with a centre of rotation collocated with the mesolow (Figure 5.26).

The surface weather effects of this MCV can be seen in the meteogram for the mesonet station at McAlester, displayed in Figure 5.27. The pressure trace reveals that the mesolow is very broad and shallow; the decrease in pressure commences ~7 h before the lowest pressure is observed at ~1630 UTC, and the following pressure rise lasts for

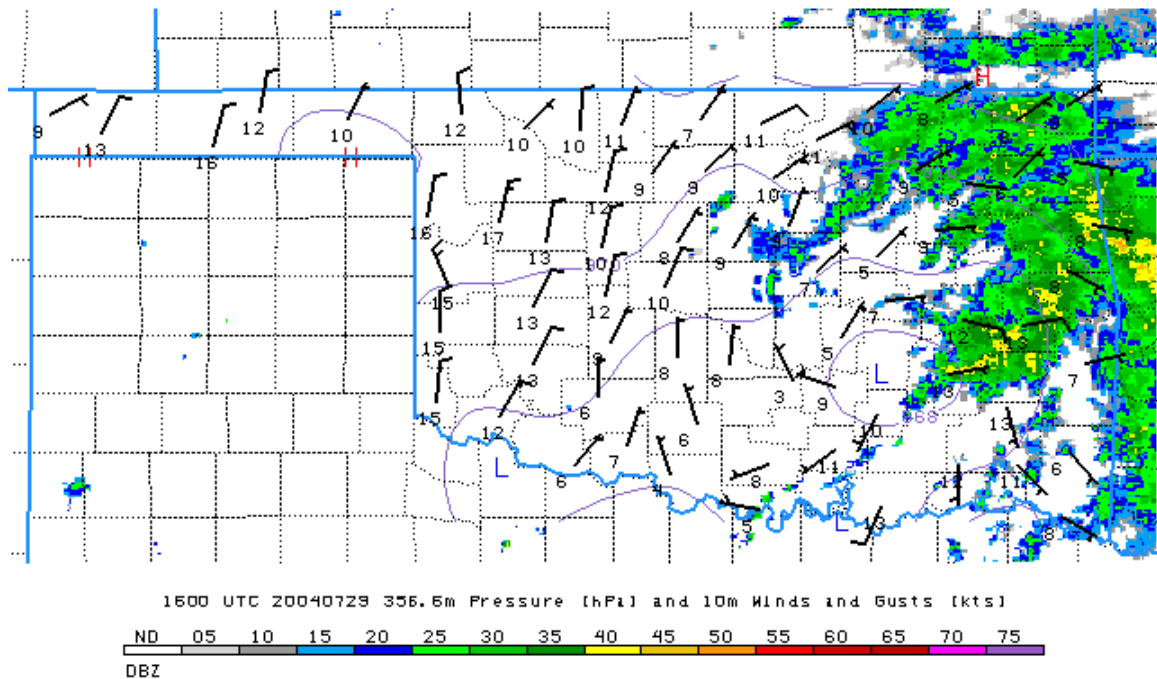


Figure 5.26: As in Figure 5.9, but at 1600 UTC on 29 July 2004.

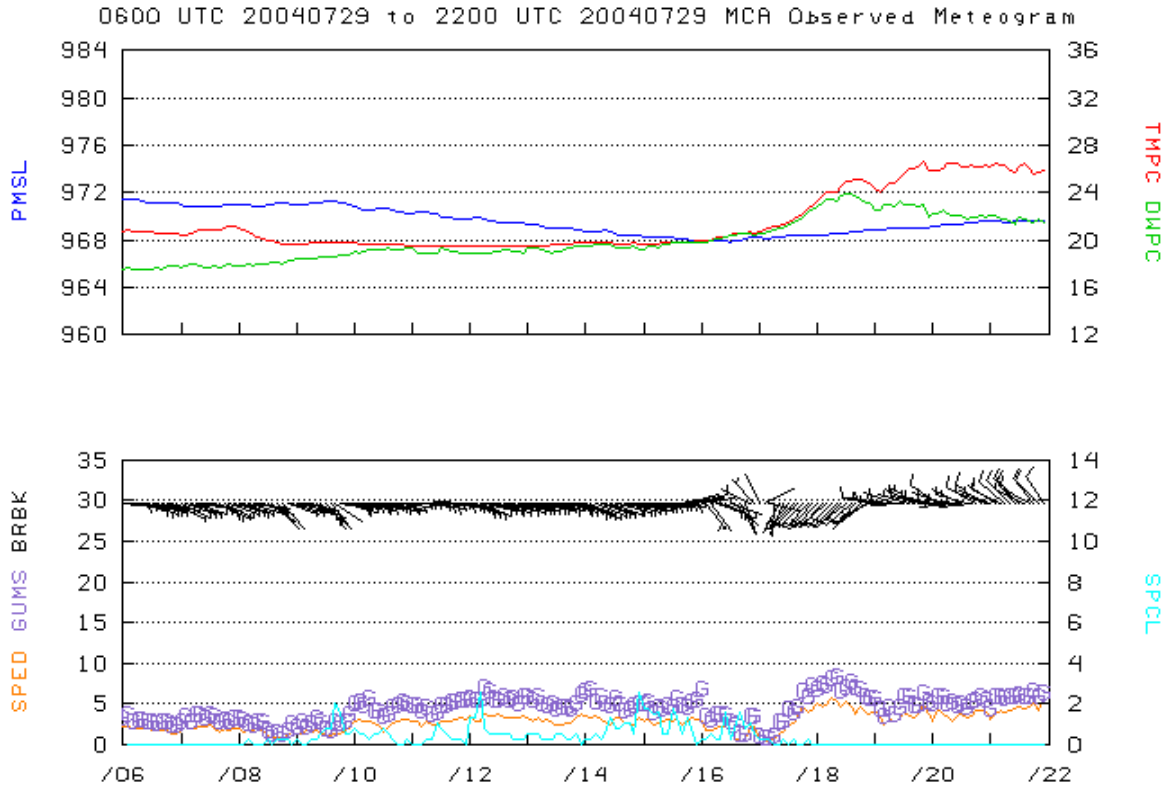


Figure 5.27: Meteoqram for McAlester mesonet station, 0600-2200 UTC on 29 July 2004. Time runs from left to right. Upper panel displays surface pressure (blue; left axis; hPa) adjusted to 356.6 m elevation, 1.5-m air temperature (red; right axis; °C), and 1.5-m dewpoint temperature (green; right axis; °C). Lower panel displays observed winds (black barbs), wind speed (orange; left axis; m/s), wind gusts (purple; left axis; m/s), and 5-minute rainfall (cyan; right axis; mm (5 minutes)⁻¹). See Figure 2.3 for station location (MCAL).

hours. However the minimum observed pressure is only ~2 hPa lower than the background pressure. It is also interesting that the near-surface air is very nearly saturated, with dewpoint depressions of <1°C for much of the mesolow passage. The MCV appears to occur within a fairly significant north-south temperature gradient, with

the temperature rising $\sim 4^{\circ}\text{C}$ over ~ 2 h; this temperature gradient seems to be associated with a weak surface warm front. While the winds clearly show the passage of a cyclonic circulation at ~ 1630 UTC, the wind speeds remain generally below 5 m/s. Also note that a ten-hour period of stratiform rainfall occurs prior to the passage of the surface mesolow.

Figure 5.28 shows a time-height section of profiler and RASS observations from the NPN site at Purcell, Oklahoma. Note that in this figure the virtual temperature anomaly contour interval has been decreased by a factor of five from that in previous figures, in order to illustrate the patterns associated with the very weak temperature variations seen in this case. The weakness of the virtual temperature anomalies in this case is notable; during the passage of the MCV (~ 1100 - 1900 UTC), the warm anomaly reaches a peak of 0.72 K at 650 hPa (at 1500 UTC). Note as well that the warm anomaly is relatively shallow, and there appear to be cool anomalies above and below. Overall, it appears that the virtual temperature profile is only weakly perturbed in the vicinity of the MCV. It may be significant that the warm anomaly occurs near the time that the MCV is closest (~ 1400), and that a relatively deep cool anomaly occurs before the arrival of the MCV.

Unfortunately, the six RASS observation sites are too sparsely distributed to enable a detailed three-dimensional analysis of the temperature perturbations associated

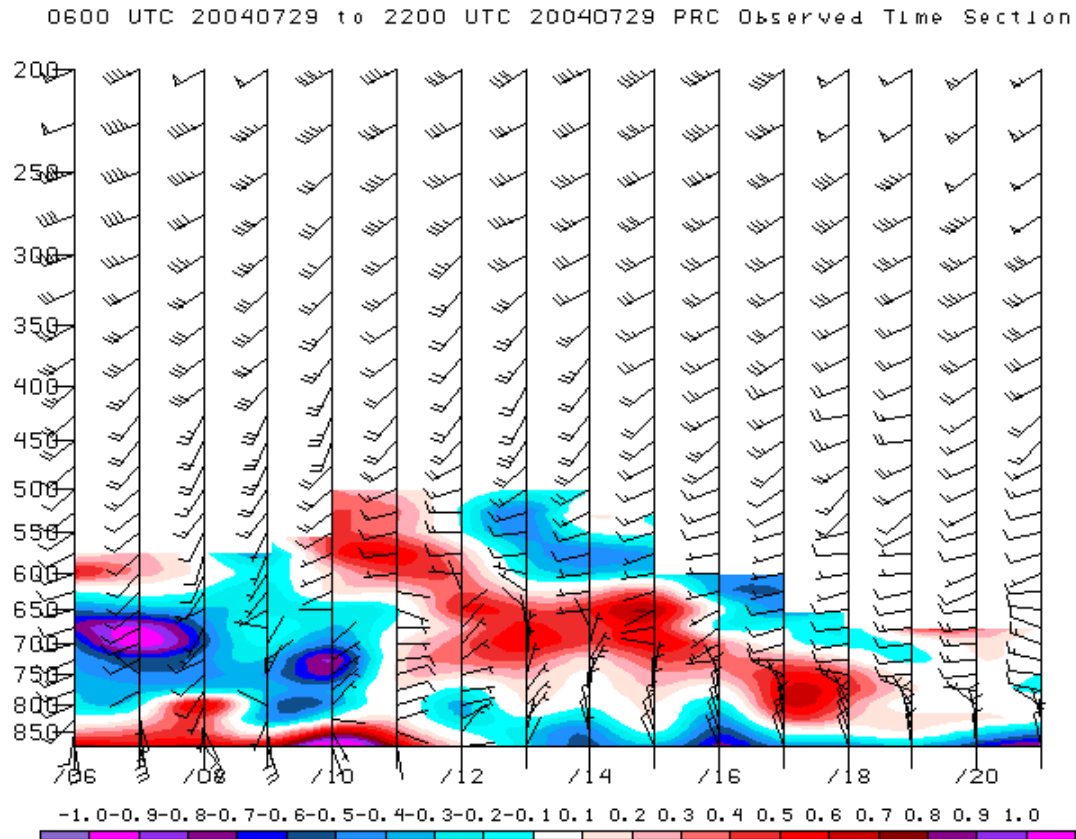


Figure 5.28: Observed time-height section for Purcell, Oklahoma, NPN site, 0600-2100 UTC on 29 July 2004. Time runs from left to right. Barbs indicate horizontal wind speed and direction. Colours indicate RASS virtual temperature anomalies (K). See Figure 2.2 for station location (PRCO2).

with this MCV. However, the RUC analysis can provide a basic overview of the system's vertical structure. Figure 5.29 shows a north-south cross-section of PV through the MCV centre at 1200 UTC, based on the RUC analysis at that time. The MCV is represented as a large and relatively deep PV tower, nearly vertically aligned. The PV tower appears directly over the surface mesolow at this time ($\sim 34.2^\circ\text{N}$; not shown), which is itself embedded within the surface frontal zone. PV of >1 PVU extends up to ~ 450 hPa, and

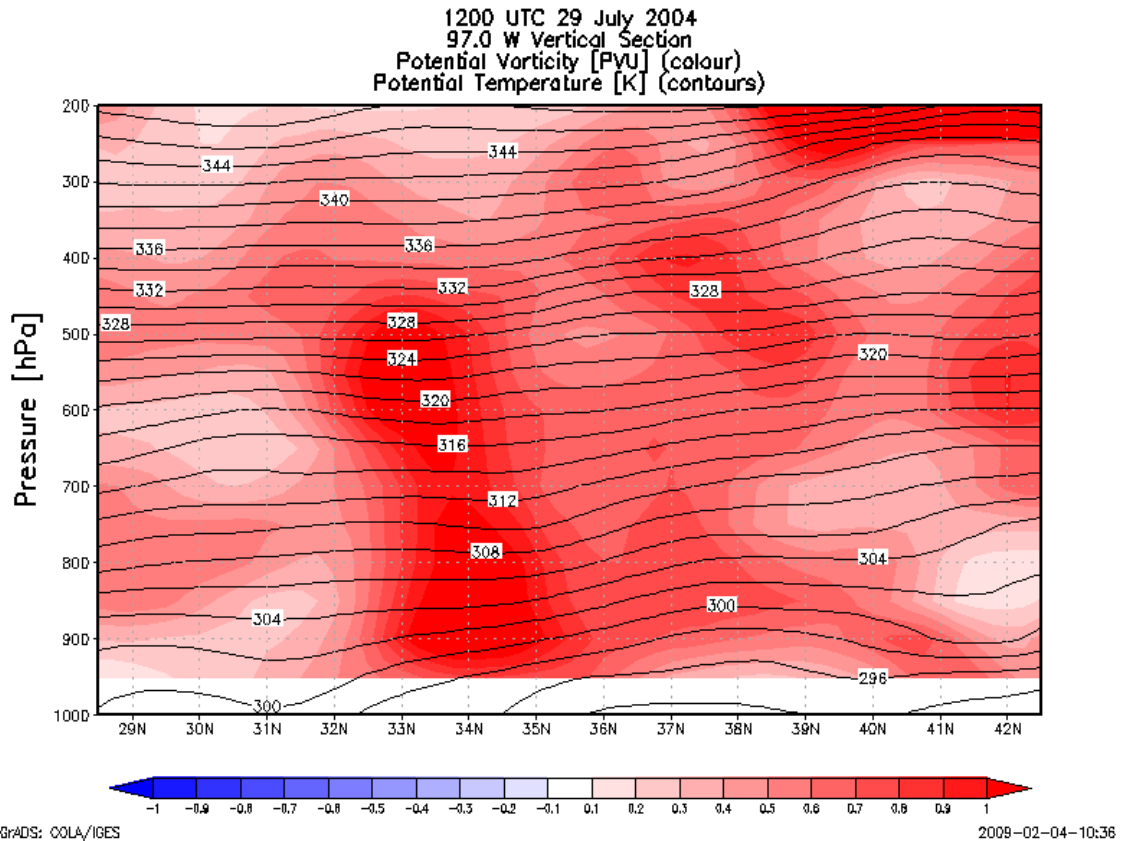


Figure 5.29: RUC cross-section of potential temperature (K; contour interval 2 K) and potential vorticity (colours; PVU) through MCV along 97°W at 1200 UTC on 29 July 2004.

the PV tower is ~200 km in diameter. The isentropes, overlaid on the PV field in Figure 5.29, show a slight depression within the PV tower from 800 to 500 hPa. However, this warm core does not appear to penetrate to the surface.

An examination of the MCV cases during BAMEX discussed by Davis and Trier (2007) reveals a very similar MCV to the present case, occurring during IOP 8 on 11 June 2003. Figure 5.30 shows east-west cross-sections of this MCV, in terms of relative

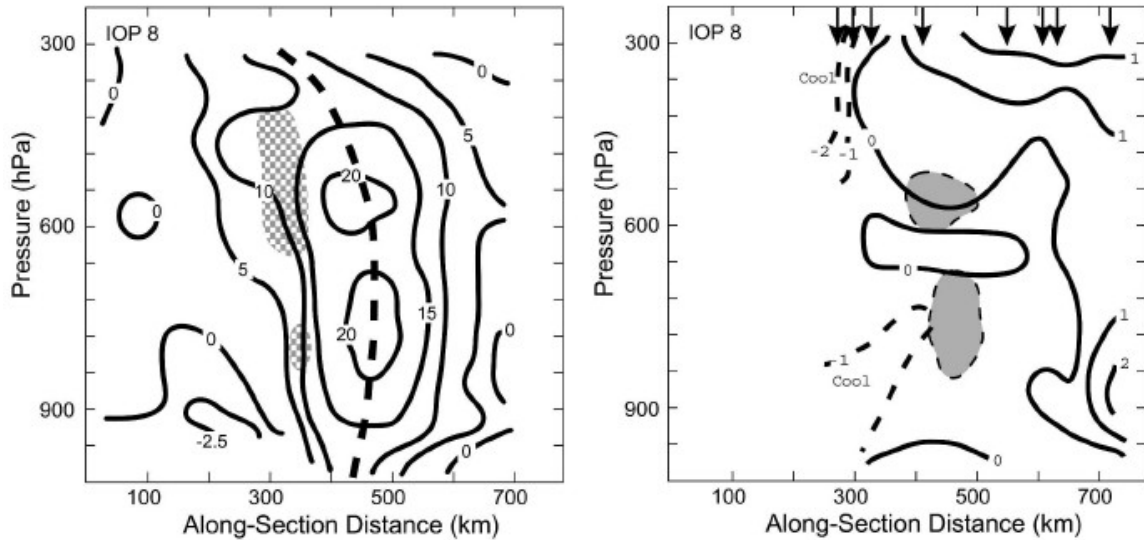


Figure 5.30: East-west cross-section of (left) relative vorticity ($\times 10^{-5} \text{ s}^{-1}$; contour interval $5 \times 10^{-5} \text{ s}^{-1}$) and (right) deviations from average dropsonde profile of virtual potential temperature (K; contour interval 1 K; negative contours dashed) for BAMEX IOP 8 MCV at 1730 UTC on 11 June 2003. In left panel, heavy dashed line represents vortex axis, and stippled region represents standard deviation of relative vorticity greater than half of the maximum value. In right panel, grey shaded region represents relative vorticity greater than $2 \times 10^{-4} \text{ s}^{-1}$. Virtual potential temperature deviations based on dropsonde observations (locations denoted by arrows at top; from Davis and Trier 2007).

vorticity and virtual potential temperature anomaly. The relative vorticity cross-section shows a coherent and vertically stacked vortex, with strong vorticity ($> 1.5 \times 10^{-4} \text{ s}^{-1}$) extending up to $\sim 400 \text{ hPa}$. While relative vorticity is not equivalent to PV, the shape and depth of the relative vorticity maximum is remarkably similar to the PV tower seen in the 29 July 2004 case (Figure 5.29). Another similarity emerges in the right-hand panel of Figure 5.30, which shows that the virtual potential temperature anomalies in the vicinity of this BAMEX MCV are minimal. The occurrence of such an MCV during the

BAMEX campaign, displaying marked similarities to the case documented here, supports the classification of these MCVs in their own category.

The question arises as to what mechanism is responsible for the development of low pressure at the surface in these interesting cases. The presence of a warm front in the 29 July 2004 case may suggest baroclinic forcing as an explanation for the surface cyclone; however, such an extratropical cyclone would possess significant vertical tilt, with the surface low occurring downstream of the mid-level PV maximum. Such tilt is not seen here. The vertical coherence of the cyclonic PV anomaly in these cases, as well as the proximity of the surface mesolow to the centre of the PV tower, suggests that the mesolow may be due to a developing, deep warm core within the MCV. Such a warm core could be produced by the diabatic heating occurring within the persistent precipitation shield in the vicinity of the MCV. In the 29 July 2004 case, the precipitation shield itself, occurring on the east side of the vortex, is likely due to the balanced lifting mechanism proposed by Raymond and Jiang (1990) acting on the north-south temperature gradient associated with the warm front. The extension of the MCV to the surface in these cases is likely enabled by the relative lack of a surface-based cold pool, which could occur in a very moist environment. The 29 July 2004 case does occur within an anomalously moist environment; according to the RUC analyses, the precipitable water in the vicinity of the vortex reaches a maximum of ~5.75 cm. This

mechanism of surface low development due to the strengthening and deepening of a warm core has been documented in prior studies of MCVs (Fritsch et al. 1994; Rogers and Fritsch 2001; Trier and Davis 2002).

e. Cold Pool Dominated MCV

The fourth type of MCV observed in this study is termed the “cold pool dominated MCV”. Three of these MCVs are documented in Oklahoma during the period of study. The mean radius and relative vorticity evolution of these cases is seen in Figures 5.1 and 5.2, respectively. It can be seen that these MCVs have near-average radii and relative vorticity. Like most of the other types, the individual cases move generally eastward, as seen in Figure 5.3. The distinguishing feature of these cases is the presence of significant reflectivity (i.e., an active MCS) during part of the MCV lifetime, but the absence of any significant surface mesolow.

The evolution of these cases is illustrated here based on a representative case from 30 July 2003. The MCS which produces this MCV initiates along the Cheyenne Ridge, in the high plains of southeastern Wyoming, in the late morning of 29 July. The convection is initially disorganised, moving southeastward in a large cluster of small cells. In the evening, as the convection moves through southwestern Kansas, a stratiform region begins to develop to the west of the active convection. The MCV is first detected

within this stratiform region at 0600 on 30 July. Figure 5.31 shows the surface pressure and composite reflectivity in the early morning of 30 July, as the MCS is entering northwestern Oklahoma. It can be seen that the pressure gradients are fairly weak; the main feature is the mesohigh centred within the stratiform region. Two hours later (Figure 5.32), the MCS continues slowly moving through northern Oklahoma. By this time, relatively high pressure extends throughout the MCS and its immediate vicinity; this is due to the widespread presence of low-level cool air. During the next few hours (Figures 5.33-5.35), the convection weakens, followed by the dissipation of the stratiform precipitation, as the MCV continues moving through Oklahoma. The surface pressure field remains relatively flat, with no mesolow forming near or within the dissipating MCS. The surface temperature field at 1700 UTC (the time of MCV dissipation; Figure 5.36) shows that a pool of cold air persists beneath the dissipating MCS. Such a cold pool would act to raise the surface pressure hydrostatically. It would also restrict the downward development of a warm core within the MCV, another possible mechanism for mesolow formation.

f. Remnant Circulation MCV

The fifth and final type of MCV observed in this study is called the “remnant circulation MCV”. This type of MCV evolution appears to be relatively common; 14 of

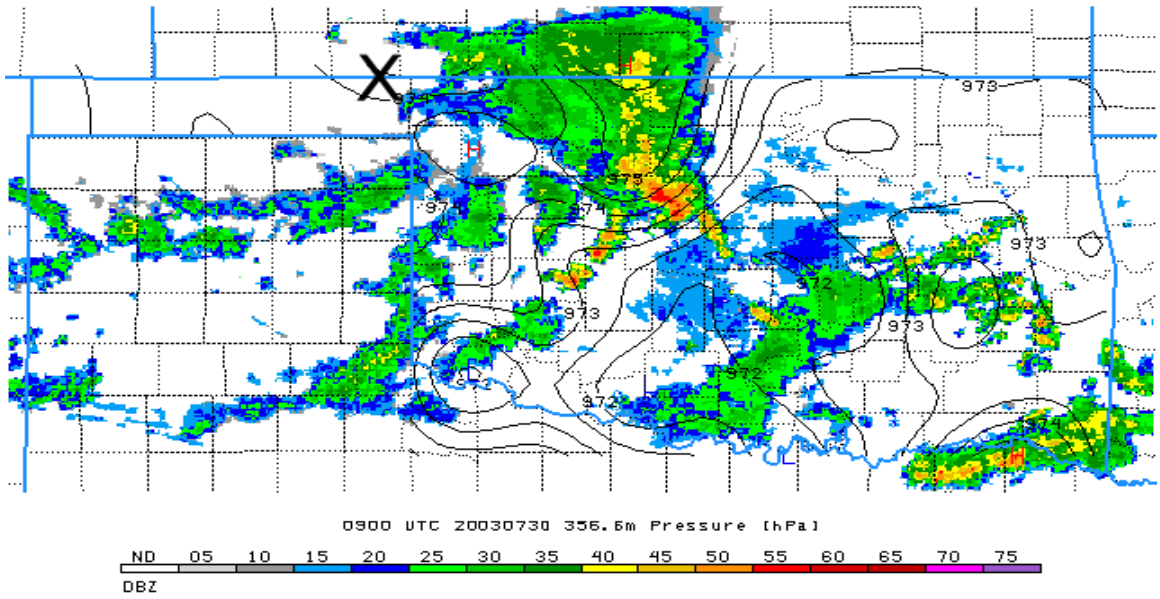


Figure 5.31: As in Figure 5.7, but at 0900 UTC on 30 July 2003.

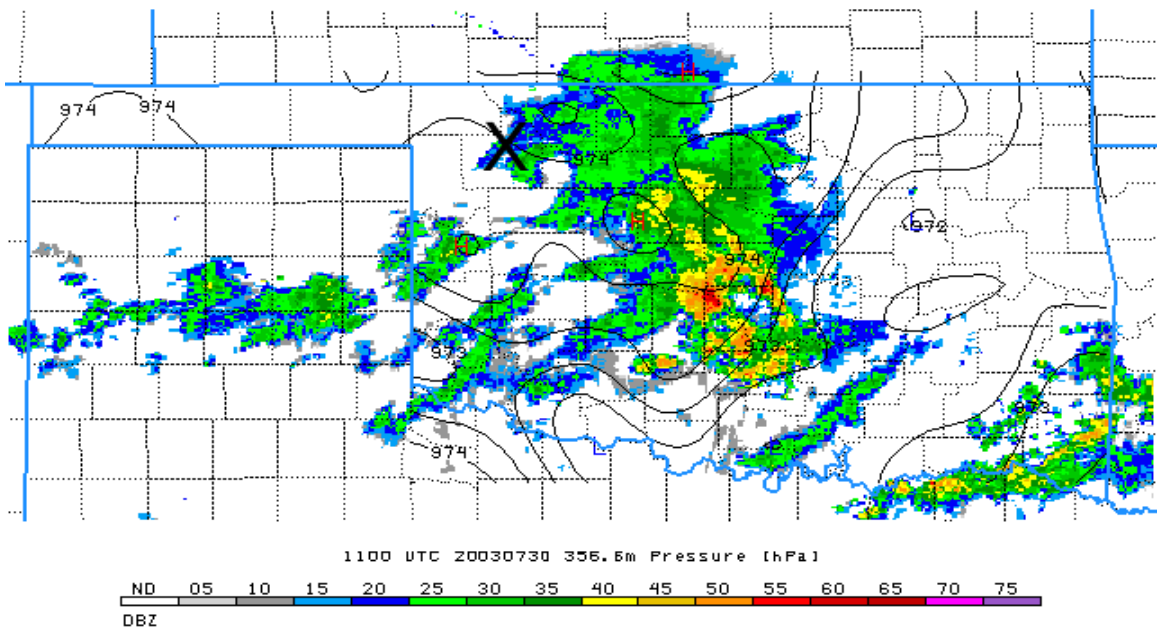


Figure 5.32: As in Figure 5.7, but at 1100 UTC on 30 July 2003.

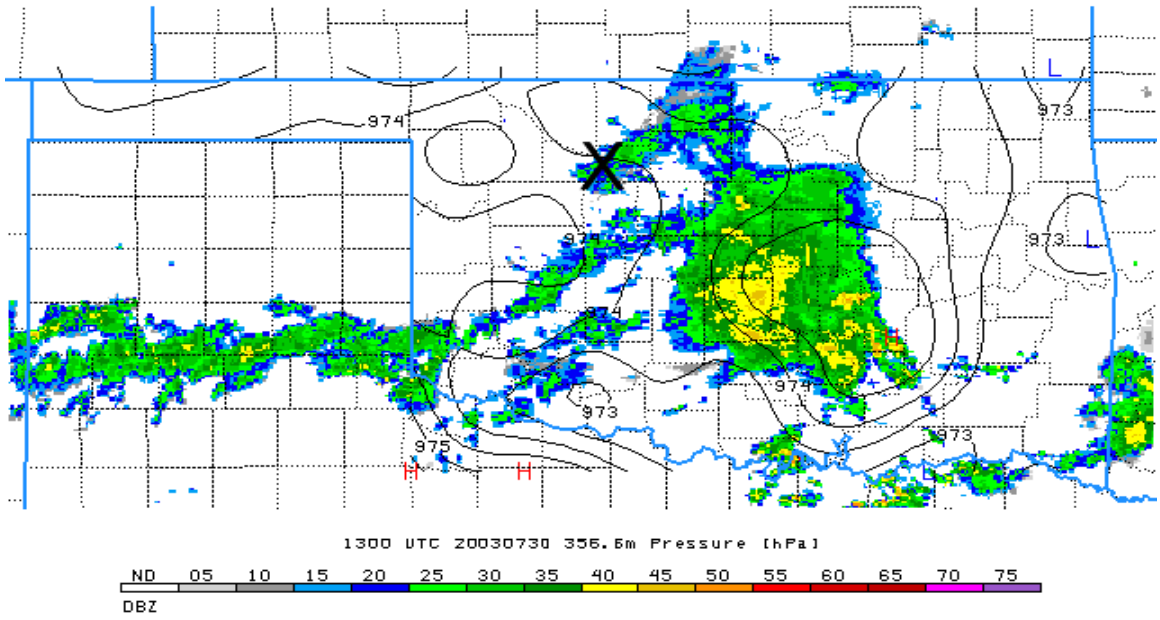


Figure 5.33: As in Figure 5.7, but at 1300 UTC on 30 July 2003.

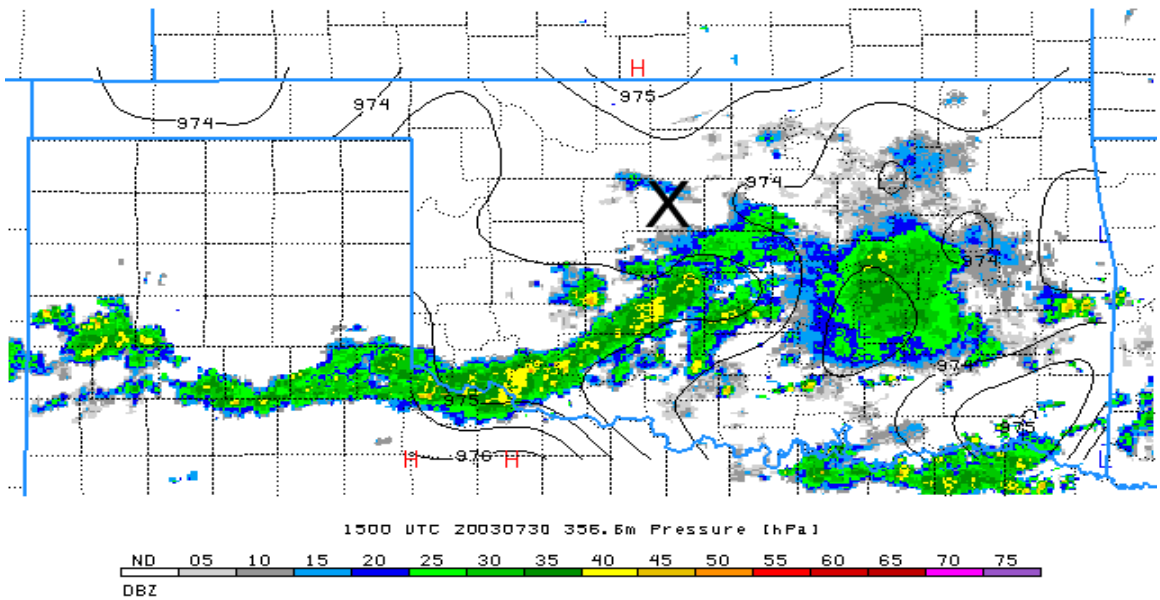


Figure 5.34: As in Figure 5.7, but at 1500 UTC on 30 July 2003.

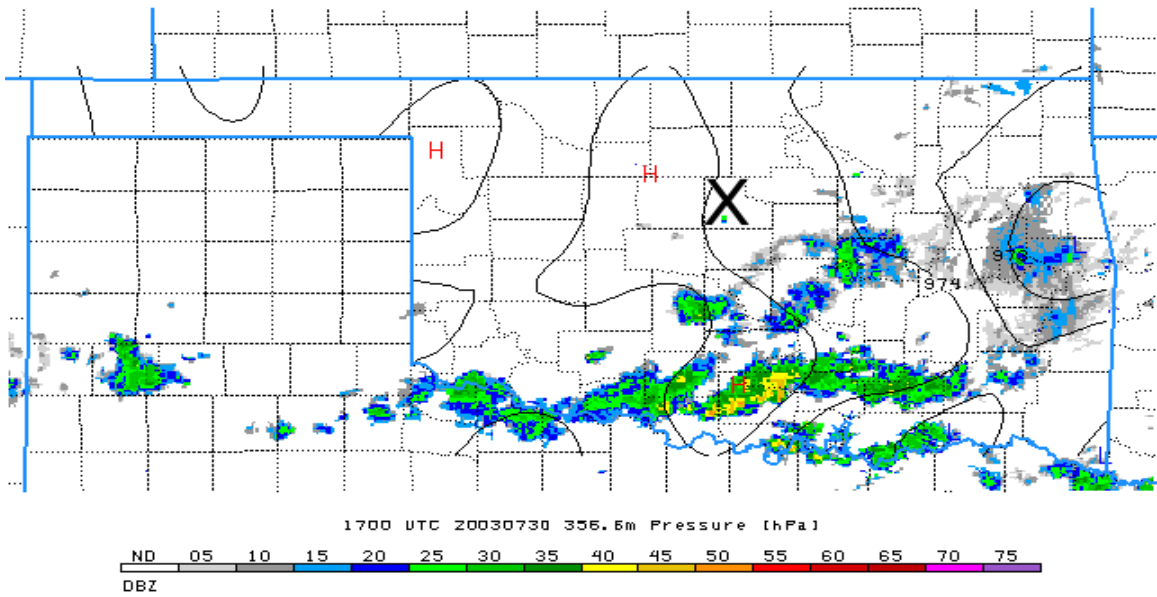


Figure 5.35: As in Figure 5.7, but at 1700 UTC on 30 July 2003.

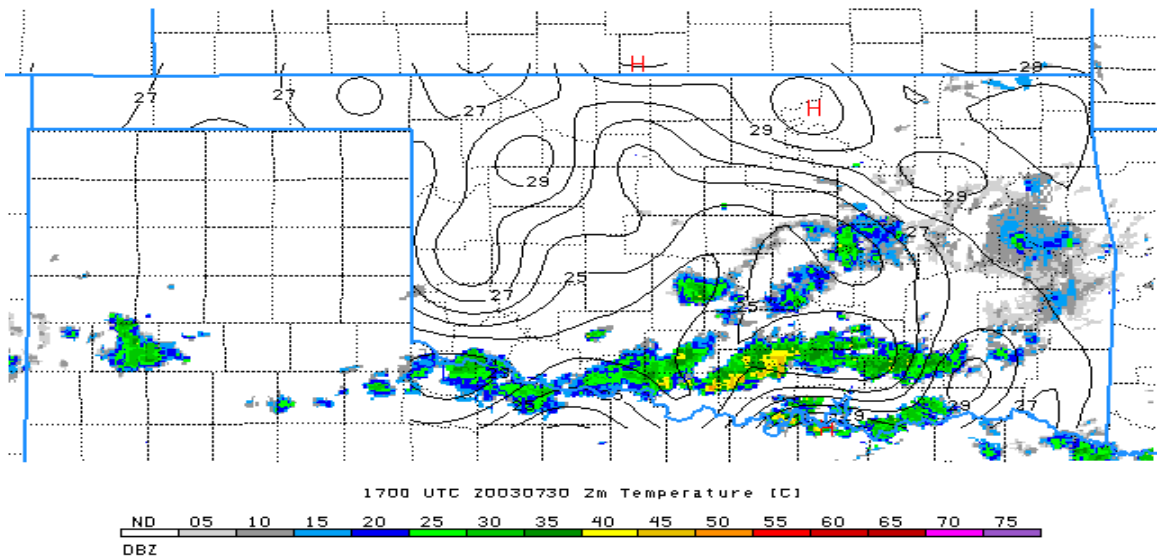


Figure 5.36: 2-m air temperature analysis ($^{\circ}\text{C}$; contour interval 1°C) of Oklahoma Mesonet overlaid on NEXRAD composite radar reflectivity (colours; dBZ) at 1700 UTC on 30 July 2003.

the 45 cases studied herein display this behaviour. Once again, Figures 5.1-5.3 show the mean radius, relative vorticity, and track evolution of these cases. These MCVs do not stand out from the rest of the distribution in any of these metrics. These cases are marked by a lack of precipitation in the vicinity of the MCV, as well as the absence of a surface mesolow. Generally, the MCVs initiate near the time of dissipation of the parent MCS, and last for a widely variable amount of time after the parent MCS has dissipated. Often, remnant mid-level cloudiness is apparent in the vicinity of the vortices upon examination of satellite imagery. The surface pressure field is usually characterised by a constant synoptic-scale pressure gradient, with no reflection of the mid-level vortex. Interestingly, 11 of the 14 remnant circulation MCVs studied here generate secondary convection at some point before their dissipation. These 11 cases represent more than half of all 17 cases that produce secondary convection in this study.

Figures 5.37-5.40 show the pressure and reflectivity evolution of one of these cases, that of 20-21 June 2003. In this case, the MCV is first detected at 1000 UTC 20 June, within the dissipating stratiform region of a rapidly weakening leading-line/trailing-stratiform MCS in the Texas panhandle. By the time the MCV enters Oklahoma at 1500 UTC (Figure 5.37), very little remains of the precipitation related to the parent MCS. The surface pressure gradient is quite weak. Over the next three hours (Figures 5.38-5.40), there is not much change. During this time, the MCV is moving slowly

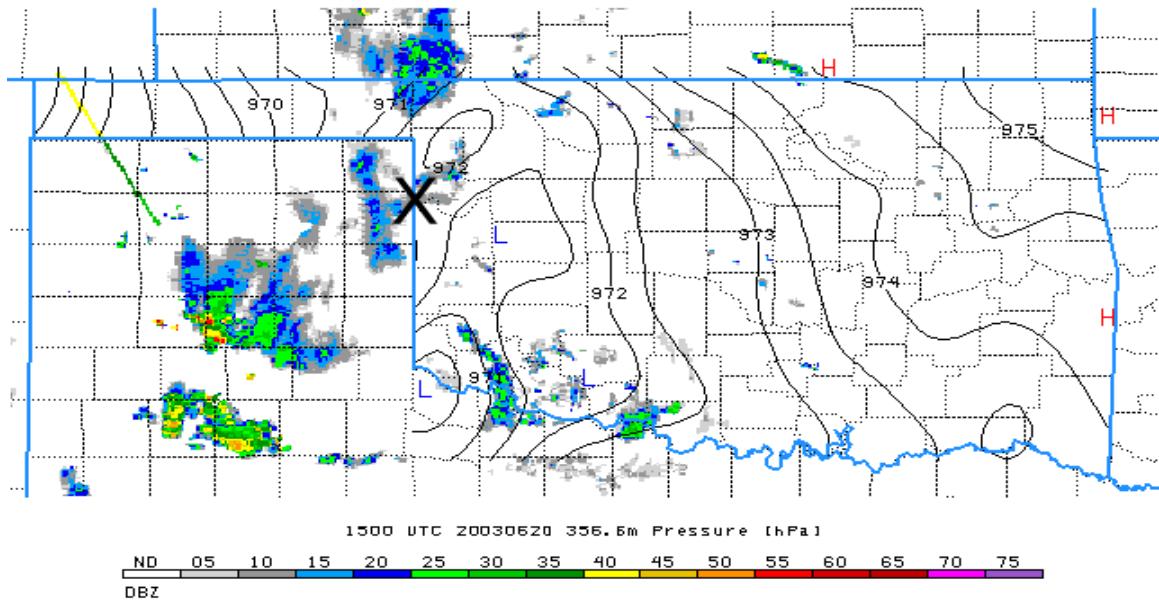


Figure 5.37: As in Figure 5.7, but at 1500 UTC on 20 June 2003.

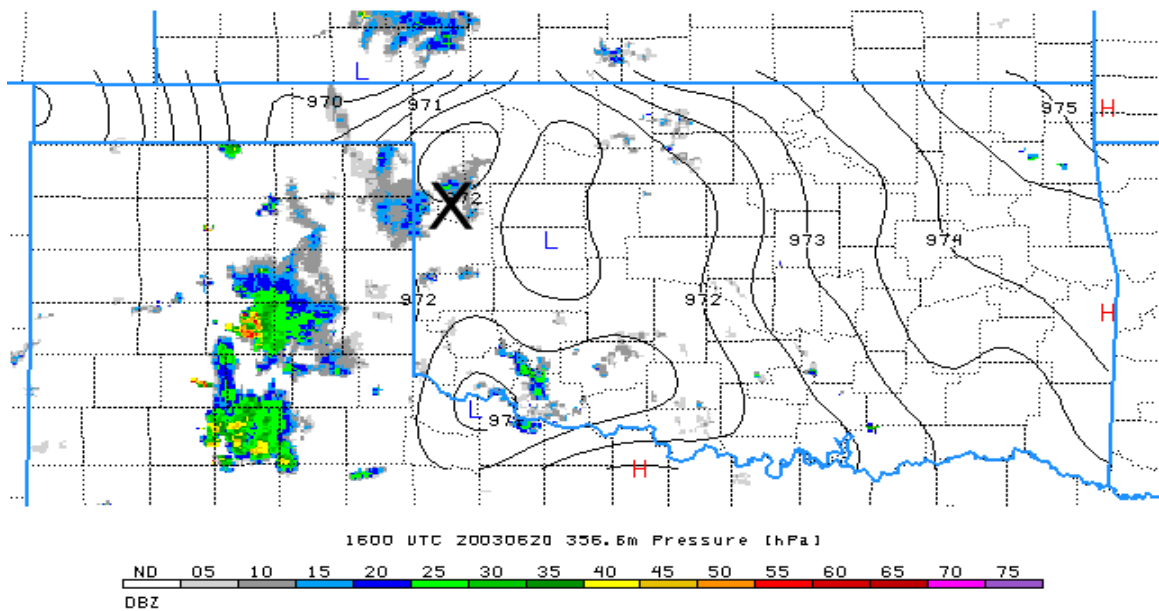


Figure 5.38: As in Figure 5.7, but at 1600 UTC on 20 June 2003.

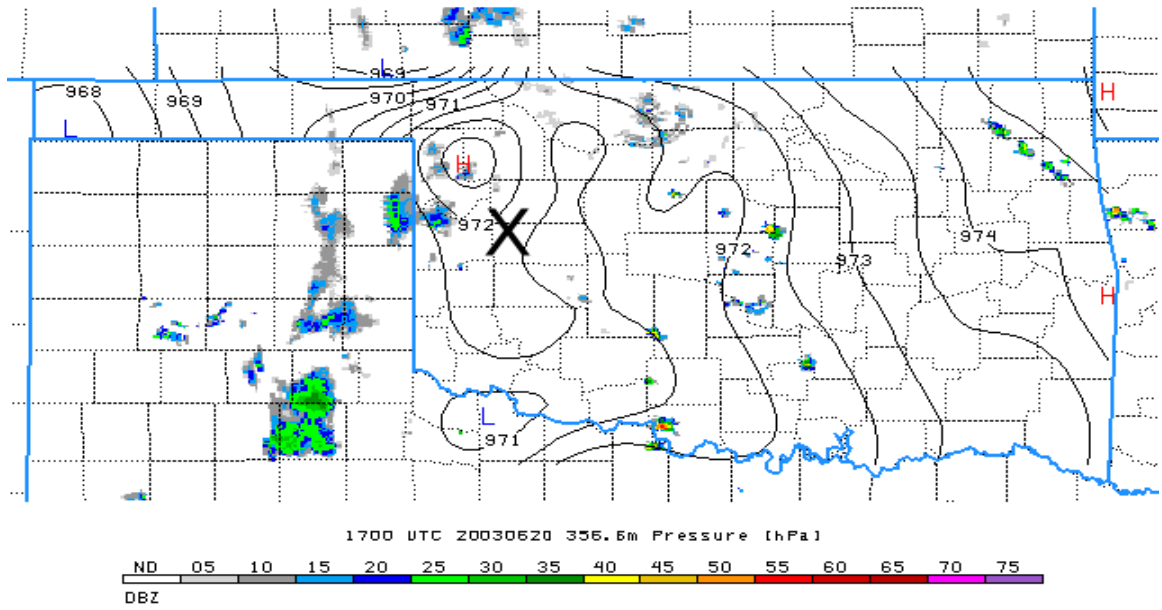


Figure 5.39: As in Figure 5.7, but at 1700 UTC on 20 June 2003.

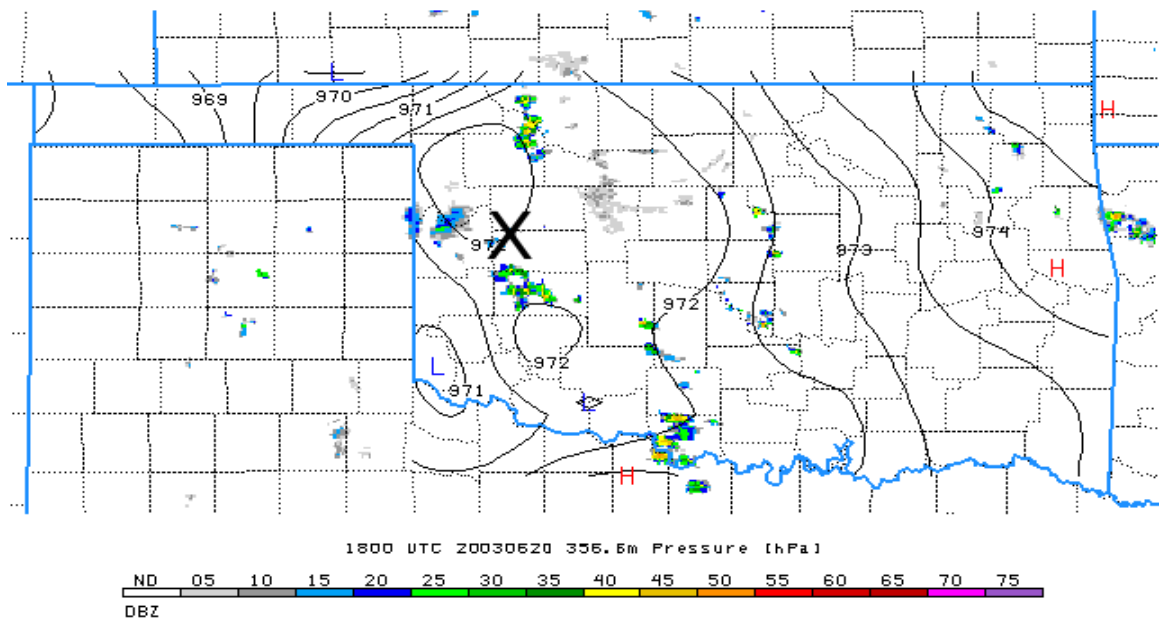


Figure 5.40: As in Figure 5.7, but at 1800 UTC on 20 June 2003.

southeastward through western Oklahoma, but there is no trace of the vortex at the surface. The surface pressure field consists of a nearly uninterrupted eastward-directed pressure gradient. A time series of observations from the Vici wind profiler observations (Figure 5.41) shows the wind field and the thermal structure associated with the MCV, which passes near this station at ~2200 UTC. At low levels, the winds remain south-southeasterly throughout the analysis period, only showing the presence of a vortex at the mid levels. Meanwhile, the virtual temperature anomalies are very weak and disorganised. This case is representative of many of this type of MCV. It appears that the development of a surface mesolow associated with an MCV requires at least some precipitation in the vicinity of the vortex. In the absence of this precipitation, there will not be strong subsidence to generate warming in unsaturated downdraughts (such as seen in the collapsing stratiform region and rear inflow jet MCVs), nor will there be diabatic heating to generate a deep warm core (as seen in the deep surface-penetrating MCV).

g. Summary

Five distinct repeating patterns of precipitation organisation and surface pressure features appear among the 45 mid-latitude MCVs analysed in this study. Three of these patterns involve the development of well-defined surface mesolows; the other two patterns lack any significant surface mesolows. Collapsing stratiform region MCVs and

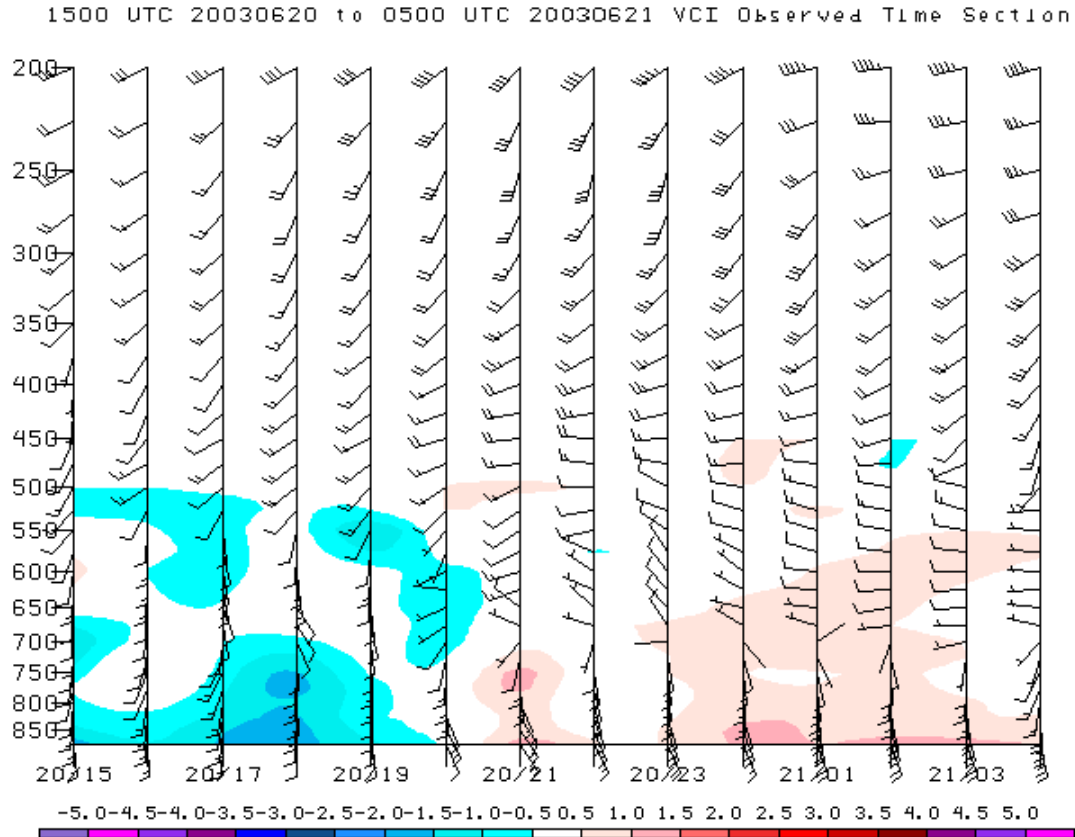


Figure 5.41: Observed time-height section for Vici, Oklahoma, NPN site, 1500 UTC 20 June through 0400 UTC 21 June 2003. Time runs from left to right. Barbs indicate horizontal wind speed and direction. Colours indicate RASS virtual temperature anomalies (K). See Figure 2.2 for station location (VCIO2).

rear inflow jet MCVs appear to produce surface mesolows due to the mechanism of subsidence warming. In collapsing stratiform region MCVs, the warming occurs over a broad region due to the dissipation of the stratiform region of the parent MCS. In rear inflow jet MCVs, the warming is more concentrated, and occurs within a descending rear inflow jet. Evidence of subsidence warming is seen in radiosonde and RASS observations in these cases. The final MCV type containing a well-defined surface

mesolow is termed the surface-penetrating MCV. In these cases, the surface low appears related to the presence of a deep warm core within the MCV. This warm core produces a hydrostatic pressure fall at the surface; thus, these cases can be described as MCVs which penetrate to the surface. In some cases, MCVs contain significant precipitation but no well-defined surface mesolow; these cases are classified as cold pool dominated MCVs. Surface pressure falls do not occur, due to the strength of the low-level cold air and mesohigh. The fifth type of MCV is the remnant circulation MCV, in which the vortex contains little or no precipitation in its vicinity, and the surface pressure and flow fields are undisturbed by the MCV.

V. DISCUSSION

This study has documented both a climatology of MCVs over Oklahoma and the surrounding region and the relationship between MCVs and their surface pressure fields. This section summarises some of the more significant results, and highlights their applicability with regard to continuing research on mesoscale meteorology.

In terms of the climatological characteristics of mid-latitude MCVs, this study has firmly established the close association of MCVs with MCSs. The initiation of MCVs is tied to the early morning maximum extent of MCCs and MCSs in the central USA, and several common features appear both in composites of mature MCC structure and of initiating MCV structure. It has been hypothesised (Velasco and Fritsch 1987) that MCVs are a fundamental component of MCC structure; this remains to be confirmed by future studies. At the present time, the observational network, even within focussed field campaigns, remains too limited to detect MCVs within MCCs with total efficiency, particularly considering the large range of MCV sizes and intensities documented here. On the other hand, it has been pointed out that the MCC size and duration thresholds introduced by Maddox (1980) are somewhat arbitrary, and important dynamical features of MCCs (including MCVs) are often present in smaller and shorter-lived MCSs;

examples of such cases have been shown in this study. Notwithstanding remaining avenues of research in this area, it is at least clear that MCVs are generated by regions of organised convection with associated stratiform precipitation.

As in a previous climatology of MCVs based on the RUC model (Davis et al. 2002), it is found that true MCVs only account for ~20% of the mid-level mesoscale vortices occurring during the summertime over the Great Plains downstream of the Rocky Mountains. Davis et al. (2002) have suggested that many of the other vortices may be topographically generated due to their concentration in the immediate lee of the Rocky Mountains. These “dry vortices” are also widespread in the domain delineated in this study. It is possible that other mechanisms, such as local instabilities of the mean flow, could produce these localised relative vorticity maxima.

Distributions of the structural characteristics of the MCVs documented here, particularly vortex radius and intensity, show considerable breadth. Vortex radius (determined within the limitations of the RUC grid) ranges from ~150 to ~250 km, with a median radius of 224 km. This is slightly larger than the 185 km median radius found by Davis et al. (2002). Similarly, vortex intensity varies by more than an order of magnitude, from $2 \times 10^{-5} \text{ s}^{-1}$ to $2.3 \times 10^{-4} \text{ s}^{-1}$. The median intensity is $\sim 1.15 \times 10^{-4} \text{ s}^{-1}$. These radius and intensity values could prove useful for verifying the realism of simulated MCVs, in both NWP and GCM applications. Similarly, the distribution of MCV

longevities, ranging up to 54 h, can provide a basis for validating the life cycles of simulated MCVs. The frequency of secondary convection (a second cycle of deep convective activity during the MCV lifetime) associated with the MCV circulations in this study is ~40%, which agrees reasonably well with 46% from Davis et al. (2002). The median lifetime of MCVs which trigger secondary convection is ~10 h greater than the lifetime of MCVs with no secondary convection; this result is in qualitative agreement with theories regarding MCV intensification by secondary convection (e.g., Rogers and Fritsch 2001).

The synoptic-scale environment of the MCVs recorded here is representative of the general situation favouring MCVs in the central USA (Bartels and Maddox 1991). In the mean, that environment consists of west-northwesterly flow downstream of a mid-level ridge and upstream of a mid-level trough. Features related to the structure of the parent MCS or MCC, such as an upper-level ageostrophic jet streak and associated divergence, as well as mid-level convergence and ascent within the MCV stratiform region, tend to be strongest at the initiating stage of the MCV, and weaken at later stages. This is due to the typical waning of convection and dissipation of precipitation after the generation of the MCV. On average, there does not appear to be a strong signal of the presence of an MCV in the synoptic-scale environment after the dissipation of the parent MCS. The single notable feature at the mid levels is the development of a pronounced

mesoscale trough in the height field, which remains significant throughout the lifetime of the composite MCV.

The appearance of a mid-level mesoscale trough can be understood from both hydrostatic and dynamic perspectives. Such a feature would be produced by warming at higher levels in the atmosphere. This warming is achieved initially by latent heating within the parent MCS; the balanced nature of the resulting MCV (i.e., the radius of the vortex being larger than the Rossby radius of deformation) keeps this warm core intact within the vortex for a long period of time. Dynamically, the increase of latent heating with height in the stratiform region of an MCS will lead to a positive midtropospheric PV anomaly (Raymond and Jiang 1990; Hertenstein and Schubert 1991). While it is likely that MCVs of varying strengths also have coherent mid-level warm cores of varying persistence and intensity, the appearance of this feature in the composite suggests that this is a common feature of MCVs.

Additional interesting features appear in the composite in the lower levels of the atmosphere. The appearance of the LLJ is noticeable at 850 hPa. The LLJ is most intense at the MCV initiating stage, weakening and veering at later times in the MCV life cycle. This is likely unrelated to the actual evolution of the MCV, and is rather a result of the preferential initiation of MCVs in the early morning hours, at a time when the LLJ is climatologically at its strongest. Previous studies have suggested that the LLJ may

often play a role in flash flood situations involving MCVs (Bosart and Sanders 1981; Davis and Trier 2002; Schumacher and Johnson 2008). The LLJ acts to transport high equivalent potential temperature air into the vicinity of the vortex; this air is then lifted, which destabilises the environment and results in localised deep convection. Lifting mechanisms can include low-level gravity waves, density currents, or balanced lifting within the thermal structure of the MCV.

The most important contribution of this study is the classification of MCVs into several types involving recurring patterns of organisation and surface effects. In the majority of the cases documented here, MCVs particularly represent one of five types: the collapsing stratiform region MCV, the rear inflow jet MCV, the surface-penetrating MCV, the cold pool dominated MCV, and the remnant circulation MCV. The remainder of this section describes these five types, and presents conceptual models of two of the three MCV types containing significant surface mesolows. Only one surface-penetrating MCV was observed; thus, despite its many interesting features and potential relevance to tropical cyclogenesis, a conceptual model is not developed based upon this single case.

The eight collapsing stratiform region MCVs documented here display the strongest similarities of all the MCV types. Figure 6.1 shows a basic conceptual model of the evolution of the collapsing stratiform region MCV. The left panel represents the mature stage of the parent MCS; these MCSs often display a very specific organisation of

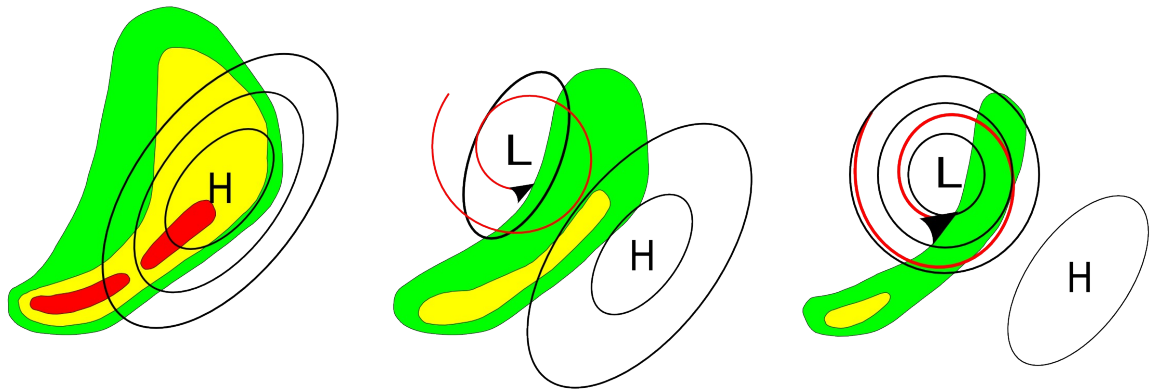


Figure 6.1: Conceptual model of the evolution of collapsing stratiform region MCVs. Time runs from left to right. Colours represent composite radar reflectivity. Green indicates 30-40 dBZ, yellow indicates 40-50 dBZ, and red indicates >50 dBZ. Thin black lines represent surface isobars (contour interval 0.5 hPa). “H” indicates centre of mesohigh, and “L” indicates centre of mesolow. Red spiral indicates developing mid-level vortex. The evolution is with respect to a system moving towards the right.

precipitation consisting of a weak convective line (variably oriented, but on average shifted $\sim 45^\circ$ relative to the direction of motion) with a small stratiform region to the left of the system motion. At this stage, the surface pressure field is characterised by a broad mesohigh within the precipitation. The mesohigh is generally centred near the leading edge of the precipitation, between the stratiform and convective regions. The central panel of Figure 6.1 shows an intermediate stage in the evolution of the system, on average about two hours later than the previous panel. By this time, the convection has weakened, the stratiform region is beginning to dissipate, a small mesolow appears at the

rear of the stratiform region, and the surface mesohigh is beginning to move out ahead of the precipitation and weaken. The mid-level vortex generally becomes sufficiently intense to be first detected by the objective algorithm a few hours after this time. The right panel in Figure 6.1 shows the final stage in the evolution of these MCVs, occurring about another two hours later. By this time, the broadening and deepening mesolow has moved into the dissipating remnants of the stratiform region, and the weak mesohigh has almost disappeared. In seven of the eight cases, the mid-level MCV is first detected by the objective algorithm before, or less than two hours after, this time. The formation of both the MCV and the surface mesolow occur during the weakening stage of the parent MCS. As was shown in Figures 4.15 and 5.4, the surface mesolow in these types of MCVs tends to be quite close to the mid-level vortex; the extent of the collocation is slightly greater than in the other MCV types. However, the difference is not statistically significant, and it is difficult to draw conclusions about the relative locations of the MCV and mesolow due to the coarse grid of the RUC analyses.

All eight collapsing stratiform region MCVs contain a developing mesolow towards the rear of the stratiform region as it dissipates, which then broadens and deepens as the precipitation diminishes and the parent MCS weakens. This indicates that the evolution of the precipitation structure of these systems influences the evolution of the surface pressure field. As demonstrated in a modeling study by Gallus (1996),

microphysical processes alone are capable of producing a realistic mesolow associated with a weakening region of stratiform precipitation. Additional numerical simulations would likely further elucidate the specific mechanisms connected with this association. Another curious feature of these MCVs is the movement of the mesohigh out ahead of the precipitation. Similar behaviour has recently been observed associated with bowing line segments within linear MCSs (Adams-Selin and Johnson 2008). It is not clear whether the same mechanisms are acting in these collapsing stratiform region MCVs.

It was noted in section 5b that collapsing stratiform region MCVs tend to be smaller and weaker than the other types. These characteristics are a possible explanation for the lack of rear inflow jets and associated wake lows within these MCVs. In these cases, the surface mesolow does appear at least indirectly related to the development of the MCV: it is likely that both develop as a result of relatively deep low- to mid-level subsidence. The compression warming which occurs within this subsidence region as the precipitation dissipates (see later stages in Figure 6.1) is responsible, hydrostatically, for the reduced pressure at the surface. The column stretching implied by this subsidence would favour the concentration of mid-level relative vorticity. This sequence of events was suggested by Johnson et al. (1989) as an explanation for the surface observations obtained in the 23-24 June 1985 OK PRE-STORM MCS, which clearly contained a collapsing stratiform region MCV.

Rear inflow jet MCVs are the second MCV type containing marked surface pressure perturbations. In these cases, the development of low surface pressure seems to occur due to the well-documented wake low mechanism, whereby a rear inflow jet flowing into an MCS stratiform region descends strongly, producing a concentrated region of subsidence warming at low levels where the precipitation has evaporated (Johnson and Hamilton 1988). Figure 6.2 shows a conceptual diagram of the evolution of these MCVs, based on the 19 cases of this type documented during this study. The left panel of Figure 6.2 represents the mature stage of the parent MCS. These MCSs show a wide variety of organisations, but one of the most frequent is the leading-line trailing-stratiform MCS (Parker and Johnson 2000). The surface pressure field at this time consists of a broad mesohigh within the precipitation. The middle panel of Figure 6.2 shows a later stage of development, on average about two hours later. By this time, the precipitation structure is starting to take on pronounced asymmetry, with the southern portion of the stratiform region beginning to erode due to the development of rear inflow on the south side of the incipient MCV. A small mesolow appears behind this eroded portion of the stratiform region. On average, the MCV is first detected by the objective algorithm near this time. The final stage, depicted in the right panel of Figure 6.2, occurs on average about two hours after the intermediate stage. By this time, the convective line has weakened and the stratiform region has been largely shunted to the left. The MCV is

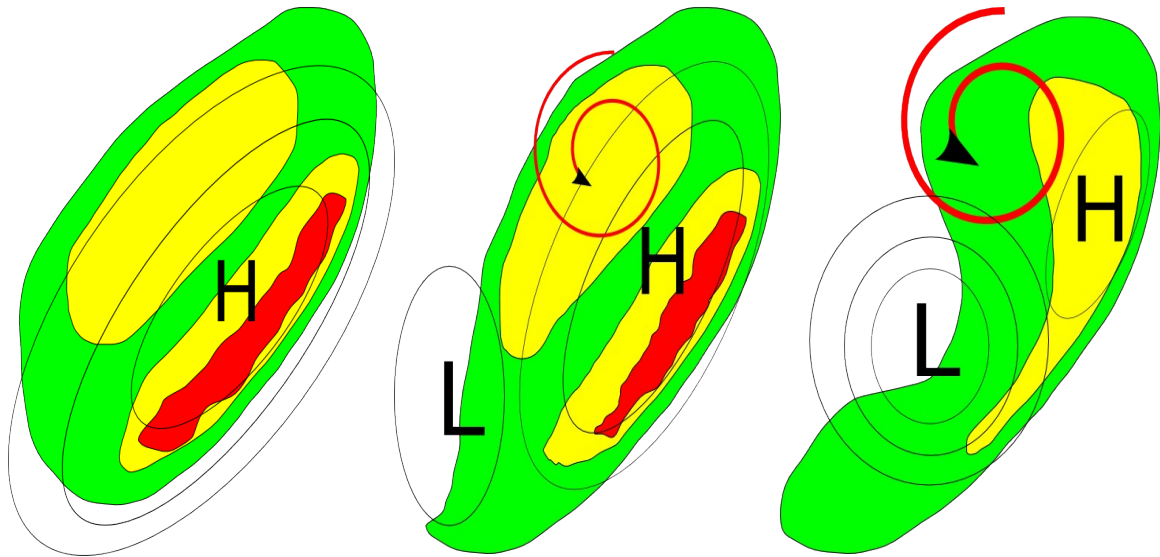


Figure 6.2: As in Figure 6.1, but of the evolution of rear inflow jet MCVs.

intensifying in the remaining portion of the stratiform region. Meanwhile, a concentrated and intense mesolow has formed just behind the eroded southern portion of the stratiform region. Often, this mesolow forms near the apex of a reflectivity notch in the back edge of the precipitation.

The organisation of many of these rear inflow jet MCVs (and, to a lesser extent, that of the collapsing stratiform region MCVs) strongly resembles an asymmetric squall line (Houze et al. 1990), but with an embedded MCV in the northern portion of the system, as introduced by Houze et al. (1989; see Figure 1.1b). A similar asymmetric precipitation structure has been documented among the OK PRE-STORM MCSs by Loehrer and Johnson (1995; see their Figure 22b), but with a mesolow occurring behind the trailing stratiform region on the north side of the system rather than on the south side

(as shown in Figure 6.1). Mesolows do occur in this position in two of the MCVs examined here; these MCVs are classified as rear inflow jet MCVs due to the positioning of the mesolow just behind the stratiform precipitation. This subset of the rear inflow jet MCVs may have distinct features, and merits further study.

The role of the MCV in these cases is somewhat obscure; perhaps it influences the positioning and strength of the rear inflow jet. Brandes (1990) argued that the MCV within the 6-7 May 1985 OK PRE-STORM MCS enhanced the rear inflow on its southern side; this MCV displayed many similarities to the rear inflow jet MCVs described in this study. In that case, as well as in the cases documented here, the location of the mesolow appears to be determined by the location of the rear inflow jet with respect to the stratiform region. The mesolow does not form directly beneath the MCV (see Figure 4.15); rather, it forms directly beneath the descending rear inflow jet, which tends to be on the southern side of the MCV.

The deep surface-penetrating MCV observed in this study, on 29 July 2004, has several unique characteristics compared with the other MCV types. The breadth and persistence of the mesolow suggest that different dynamics are active than in the other cases. Upper-air observations from the NPN do not reveal any obvious low-level warming such as would be expected in the vicinity of MCVs of the first two types. However, analyses from the RUC model do indicate a relatively deep warm core at the

mid levels, associated with a coherent tower of high PV. The surface mesolow is apparently a hydrostatic result of the mesoscale warm core associated with the MCV. It is not immediately obvious why the warm core is so much stronger in this case than in other cases; perhaps it is related to the longevity of the associated precipitation shield and its associated diabatic heating. Moderate rainfall occurs on the eastern flank of the MCV throughout its lifetime, and rainfall occurs associated with the parent MCS throughout the previous day. While the warm core does not appear to extend to the surface, it is also apparent that there is no well-defined surface cold pool. The weakness of the cold pool may be the defining feature allowing such a strong mesolow to form. The situation is complicated by the apparent presence of a warm front beneath the MCV; however, the weakness of the front, together with the circular shape of the mesolow and the associated cyclonic surface wind circulation, suggest that it is not playing a major role in the development of the mesolow.

It is tempting to compare the surface-penetrating MCV with an incipient tropical cyclone. The similarities are considerable: there is a closed surface circulation with a well-defined low pressure centre, a coherent and deep tower of high PV extending into the mid to upper troposphere, and an extremely moist environment. The lack of any significant organisation of the precipitation field, as well as the weakness of the surface wind field, may be related to the fact that the system is in its early stages of development.

Soundings taken in the environment of the 29 July 2004 MCV reveal that the atmosphere is nearly saturated, with a nearly moist adiabatic lapse rate. Figure 6.3 shows the 1200 UTC radiosonde taken from Fort Worth, Texas. This sounding contains a precipitable water value of 5.45 cm. In the lowest ~80 hPa, though, there is a nearly isothermal layer; this layer effectively caps the atmosphere to surface-based convection. This shallow layer of cool air is likely responsible for the lack of organised surface-based convection near the centre of circulation, such as one would expect within a developing tropical cyclone. The lack of strong surface fluxes from an underlying warm ocean could explain the persistence of the cool layer and the failure of tropical cyclogenesis (Fritsch et al. 1994). While the low-level cold air is not as deep or extensive as is typical of MCS cold pools, and it is apparently weak enough to allow a well-defined surface reflection of the mid-level warm core, this cool layer prevents surface-based convection from developing within the circulation. Surface fluxes from a warm ocean surface would further weaken the cold pool, and would likely allow the MCV to transition to a true tropical cyclone (Rogers and Fritsch 2001). A recent study by Emanuel et al. (2008) suggests another means by which MCVs could become genuinely surface-based. Addressing the frequently observed regeneration of tropical cyclones over the hot deserts of northern Australia several days after landfall, Emanuel et al. (2008) find that the extreme heat flux from the hot and wet soil can become sufficient to maintain a cyclone of minimal

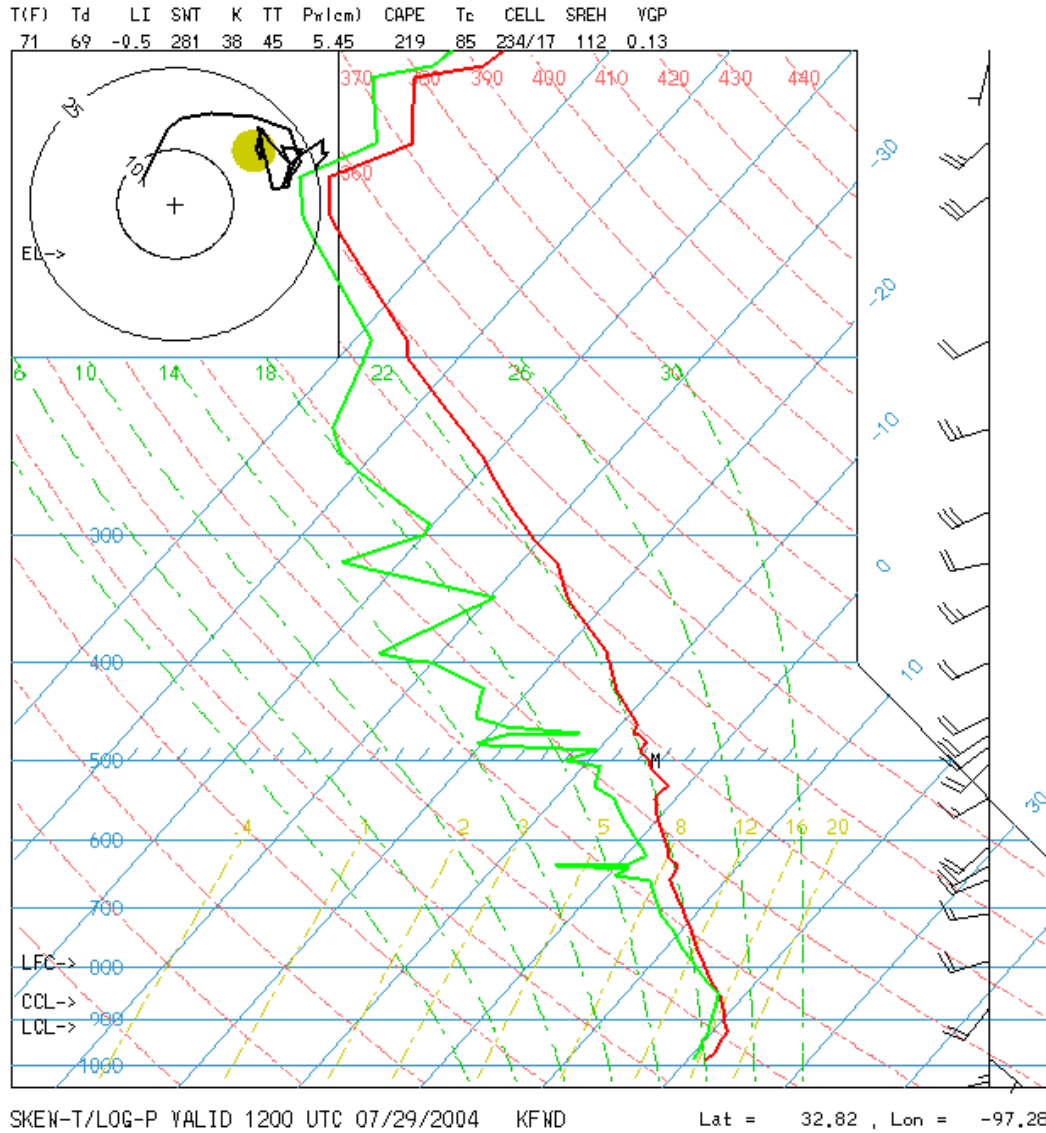


Figure 6.3: Skew-T/log-p plot of radiosonde from Dallas-Fort Worth (KFWD) at 1200 UTC on 29 July 2004.

hurricane intensity. Numerical simulations would enable these hypotheses to be tested in the 29 July 2004 case, using a variety of surface flux sensitivity experiments.

The final two types of MCVs documented in this study represent the vortices which fail to develop significant surface pressure perturbations. The mesolow

development mechanisms active in the previous cases are not present in these MCVs for a variety of possible reasons. The cold pool dominated MCVs contain significant precipitation, but it is likely that the deep and extensive surface cold pool masks any potential pressure perturbations due to warming aloft. The remnant circulation MCVs lack significant precipitation in their vicinity; precipitation is required for the hypothesised mesolow development mechanisms active in the other MCV types.

Several important limitations to this classification of the MCVs should be kept in mind when considering these results. The main potential issue is the limited extent of the study domain (i.e., the state of Oklahoma). Nearly all of the 45 MCVs documented here moved outside of the state at some point during their life cycle; during these times it was impossible to determine the surface pressure field associated with the vortices. Thus, aspects of the MCV types that deal with the evolution of the surface pressure field are based only on the period during which the MCV is within the Oklahoma Mesonet. In some cases, it is possible that MCVs transition between types during different stages of their life cycle. This limitation introduces some uncertainty into the classifications. However, the availability of radar reflectivity data over a much larger region does allow tracking of the precipitation structure of the vortices outside of Oklahoma. In the majority of the cases documented here, it is believed that MCVs particularly resemble one of the five types throughout their life cycle. It should also be kept in mind that the

detection of the MCVs by the objective algorithm is wholly based on their presence in the RUC analyses.

It is beyond the scope of this study to determine the reasons for the different developmental evolution of the different MCV types. It is left to future research, both observational and modelling work, to confirm the processes described in this study, and to seek an explanation for the variety of precipitation structures and surface pressure patterns observed. The improved understanding resulting from this research will allow for a more coherent and full understanding of the complete life cycles of MCSs, and will ultimately lead to improved forecasting of hazardous convective weather.

VI. CONCLUSIONS

This study has described a number of characteristics of mid-latitude MCVs based on a fairly large sample of cases (45) observed over the state of Oklahoma during four years. MCV case detection was achieved with an objective algorithm developed to operate on hourly analyses from the operational RUC model, as described by Davis et al. (2002). The use of this algorithm has allowed a meaningful comparison of the derived climatological aspects of MCVs with the Davis et al. (2002) study. It was found that MCVs are a mesoscale phenomenon, having a typical radius of ~200 km, and achieving their maximum relative vorticity (of $\sim 1 \times 10^{-5} \text{ s}^{-1}$) in the mid troposphere (from 600 to 500 hPa). As found in previous studies, the longevity of the MCVs varies widely, with some systems only detected for one hour, and others lasting for more than 48 h. The vortices arise from MCSs displaying a large variety of organisations; however, all parent MCSs contained significant stratiform precipitation. The frequency of secondary convection (a second period of deep convective activity during the MCV life cycle) associated with the MCVs was found to be ~40%, consistent with previous studies. MCVs with secondary convection are more likely to be long-lived than MCVs generating no secondary convection.

A composite of the synoptic-scale environment of the MCV cases reveals that MCVs tend to initiate within mature, nocturnal MCCs and MCSs. Features common to composites of both initiating MCVs and mature MCCs include an ageostrophic upper-level jet streak and associated divergence, mid-level convergence and ascent within the precipitation system, and a south-southwesterly LLJ. The initiation of the MCVs thus appears tied to the diurnal cycle. Cross-sections of PV through the composite MCV reveal that the vortex circulation is, on average, confined to the mid levels. The concentration of PV in the MCV interior is due to both the locally high relative vorticity and the high static stability arising from strong diabatic heating. The development of a system-scale warm core is seen in the gradual depression of the mid- to upper-level isentropes within the cyclonic PV anomaly.

Five repeating patterns of precipitation structure and surface pressure evolution have been identified based on the cases considered here. *Collapsing stratiform region MCVs* (comprising eight cases, or 18% of the total) are smaller and weaker than the average of the MCV population, and their parent MCSs often display a peculiar precipitation structure and a tendency for southeastward movement. These MCVs form within the dissipating stratiform regions of relatively small MCSs, and their formation is coincident with surface mesolow development in the centre of the dissipating stratiform region. Evidence has been presented supporting the idea that the surface mesolow is a

result of broad subsidence warming within a large downdraught after the dissipation of the precipitation. It is also likely that the spin-up of the MCV is enhanced by the stretching term due to this low- to mid-level subsidence. These results imply that forecasters should be vigilant for MCV development, which may influence convective potential in the region over the next ~24 h, when a broad and deep mesolow forms within the collapsing stratiform region of an MCS.

Rear inflow jet MCVs (19 cases, or 42% of the MCVs) are generally produced by large and intense MCSs. These MCSs tend to adhere to the asymmetric squall line structure (Houze et al. 1990), with a mid-level circulation embedded in the northern portion of the system (Houze et al. 1989). The rear inflow, which develops in response to the strong latent heating, flows into the MCS stratiform region (Pandya and Durran 1996), eventually descending towards the surface. This descending rear inflow jet can lead to pronounced subsidence warming in areas where the evaporation of precipitation is insufficient to offset the dry adiabatic warming due to compression. As the MCS begins to weaken and the stratiform region is eroded from the rear, a strong mesolow forms due to low-level subsidence warming at the back edge of the stratiform rainfall. The MCV first appears near this time. The MCV may play a role in directing and intensifying the rear inflow current in these systems. The strong surface pressure gradients associated with wake lows are generally not associated with severe surface winds, but there are

exceptions (Johnson et al. 1996). Additionally, strong low-level wind shear is often found in the vicinity of these mesolows, and can pose a major aviation hazard (Johnson 2001). Thus, perhaps the detection of an MCV within a large and vigorous MCS could alert forecasters to the possibility of wake low development and the associated hazards.

Surface penetrating MCVs, of which only one is documented in this study, occur within exceptionally moist environments; this factor limits the extent and strength of the surface-based cold pool due to the parent MCS. When this situation occurs coincident with a persistent and large region of latent heating due to stratiform precipitation, an MCV with a relatively deep warm core can form in the mid to upper levels. The weak surface cold pool allows a large and strong surface mesolow to develop in response to the warming aloft; however, the cool near-surface air also prevents surface-based convection from forming near the mesolow. The development of such convection near the circulation centre would likely be a first step towards tropical cyclogenesis were such systems to occur over a warm ocean.

Cold pool dominated MCVs (3 cases, or 7% of the MCVs) lack any significant surface pressure perturbations despite having widespread precipitation. The lack of mesolows in these MCVs appears to be due to deep and extensive low-level cold pools.

Remnant circulation MCVs (14 cases, or 31% of the MCVs) are characterised by a lack of precipitation in the vicinity of the vortex; such MCVs generally produce no

effect on the surface pressure, and the low-level synoptic-scale flow remains uninterrupted.

Several avenues of future research are suggested by the findings of this study. Further observations of MCVs are needed; specifically, high-resolution upper-air observations, such as can be obtained with dropsonde-equipped aircraft during field campaigns, would be helpful in diagnosing the detailed structure of MCVs. It would also be interesting to compare MCV climatologies from different locations around the world. Numerical simulations of MCV evolution in a variety of environments could confirm the mesolow formation mechanisms proposed in this study. In addition, such simulations may elucidate the underlying causes for the wide variety of MCV structures and evolutions observed. Specific remaining questions include the effects of the environment, including wind shear, in determining MCV evolution, the role of surface fluxes on the downward penetration of MCVs, and the influence of MCV-induced mesolows upon secondary convection.

The goal of this study is to contribute to the small but growing body of research on the dynamics of MCVs. Remarkably little is known about the details of these systems, despite their demonstrated importance to convective initiation, flash flooding, and warm season precipitation predictability. This study could provide a basis for further investigations on many aspects of MCVs, particularly those making use of increasingly

sophisticated numerical models, and it is anticipated that continuing research in this area will eventually lead to marked improvements in warm season forecast skill in the mid latitudes.

REFERENCES

- Adams-Selin, R. D., and R. H. Johnson, 2008: Investigation of mesoscale surface pressure and temperature features associated with bow echoes. *Mon. Wea. Rev.*, in press.
- Bartels, D. L., and R. A. Maddox, 1991: Midlevel cyclonic vortices generated by mesoscale convective systems. *Mon. Wea. Rev.*, **119**, 104-118.
- , J. M. Brown, and E. I. Tollerud, 1997: Structure of a midtropospheric vortex induced by a mesoscale convective system. *Mon. Wea. Rev.*, **125**, 193-211.
- Benjamin, S. G., D. Dévényi, S. S. Weygandt, K. J. Brundage, J. M. Brown, G. A. Grell, D. Kim, B. E. Schwartz, T. G. Smirnova, T. L. Smith, and G. S. Manikin, 2004: An hourly assimilation-forecast cycle: The RUC. *Mon. Wea. Rev.*, **132**, 495-518.
- Bernstein, B. C., and R. H. Johnson, 1994: A dual-Doppler radar study of an OK PRE-STORM heat burst event. *Mon. Wea. Rev.*, **122**, 259-273.
- Biggerstaff, M. I., and R. A. Houze, Jr., 1991: Midlevel vorticity structure of the 10-11 June 1985 squall line. *Mon. Wea. Rev.*, **119**, 3066-3079.
- Bister, M., and K. A. Emanuel, 1997: The genesis of Hurricane Guillermo: TEXMEX analyses and a modeling study. *Mon. Wea. Rev.*, **125**, 2662-2682.
- Bosart, L. F., 1986: Kinematic vertical motion and relative vorticity profiles in a long-lived midlatitude convective system. *J. Atmos. Sci.*, **43**, 1297-1299.
- , and F. Sanders, 1981: The Johnstown flood of July 1977: A long-lived convective system. *J. Atmos. Sci.*, **38**, 1616-1642.
- Bousquet, O., and M. Chong, 2000: The oceanic mesoscale convective system and associated mesovortex observed 12 December 1992 during TOGA-COARE. *Quart. J. Roy. Meteor. Soc.*, **126**, 189-211.
- Brandes, E. A., 1990: Evolution and structure of the 6-7 May 1985 mesoscale convective system and associated vortex. *Mon. Wea. Rev.*, **118**, 109-127.
- , and C. L. Ziegler, 1993: Mesoscale downdraft influences on vertical vorticity in a mature mesoscale convective system. *Mon. Wea. Rev.*, **121**, 1337-1353.
- Braun, S. A., and R. A. Houze, Jr., 1997: The evolution of the 10-11 June 1985 PRE-STORM squall line: Initiation, development of rear inflow, and dissipation. *Mon. Wea. Rev.*, **125**, 478-504.

- Brown, J. M., 1979: Mesoscale unsaturated downdrafts driven by rainfall evaporation: A numerical study. *J. Atmos. Sci.*, **36**, 313-338.
- , K. R. Knupp, and F. Caracena, 1982: Destructive winds from shallow, high-based cumulonimbus. Preprints, *12th Conf. on Severe Local Storms*, San Antonio, TX, Amer. Meteor. Soc., 272-275.
- Brunk, I. W., 1949: The pressure pulsation of 11 April 1944. *J. Meteor.*, **6**, 181-187.
- , 1953: Squall lines. *Bull. Amer. Meteor. Soc.*, **34**, 1-9.
- Charba, J., 1974: Application of gravity current model to analysis of squall-line gust front. *Mon. Wea. Rev.*, **102**, 140-156.
- , and Y. Sasaki, 1971: Structure and movement of the severe thunderstorms of 3 April 1964 as revealed from radar and surface meso-network data analysis. *J. Meteor. Soc. Japan*, **49**, 191-214.
- Chen, G. T.-J., and C.-Y. Liang, 1992: A midlevel vortex observed in the Taiwan Area Mesoscale Experiment (TAMEX). *J. Meteor. Soc. Japan*, **70**, 25-41.
- Chen, S.-J., and L. D. Dell'Osso, 1984: Numerical prediction of the heavy rainfall vortex over the eastern Asia monsoon region. *J. Meteor. Soc. Japan*, **62**, 730-747.
- Chen, S. S., and W. M. Frank, 1993: A numerical study of the genesis of extratropical convective mesovortices. Part I: Evolution and dynamics. *J. Atmos. Sci.*, **50**, 2401-2426.
- Chong, M., and O. Bousquet, 1999: A mesovortex within a near-equatorial mesoscale convective system during TOGA COARE. *Mon. Wea. Rev.*, **127**, 1145-1156.
- , and D. Hauser, 1989: A tropical squall line observed during the COPT 81 experiment in West Africa. Part II: Water budget. *Mon. Wea. Rev.*, **117**, 728-744.
- , and -----, 1990: A tropical squall line observed during the COPT 81 experiment in West Africa. Part III: Heat and moisture budgets. *Mon. Wea. Rev.*, **118**, 1696-1706.
- , P. Amayenc, G. Scialom, and J. Testud, 1987: A tropical squall line observed during the COPT 81 experiment in West Africa. Part I: Kinematic structure inferred from dual-Doppler radar data. *Mon. Wea. Rev.*, **115**, 670-694.
- Conzemius, R. J., R. W. Moore, M. T. Montgomery, and C. A. Davis, 2007: Mesoscale convective vortex formation in a weakly sheared moist neutral environment. *J. Atmos. Sci.*, **64**, 1443-1466.
- Cotton, W. R., R. L. George, P. J. Wetzell, and R. L. McAnelly, 1983: A long-lived mesoscale convective complex. Part I: The mountain-generated component. *Mon. Wea. Rev.*, **111**, 1893-1918.

- , M.-S. Lin, R. L. McAnelly, and C. J. Tremback, 1989: A composite model of mesoscale convective complexes. *Mon. Wea. Rev.*, **117**, 765-783.
- Cram, T. A., M. T. Montgomery, and R. F. A. Hertenstein, 2002: Early evolution of vertical vorticity in a numerically simulated idealized convective line. *J. Atmos. Sci.*, **59**, 2113-2127.
- Cunning, J. B., 1986: The Oklahoma-Kansas Preliminary Regional Experiment for STORM-Central. *Bull. Amer. Meteor. Soc.*, **67**, 1478-1486.
- Davis, C. A., and S. B. Trier, 2002: Cloud-resolving simulations of mesoscale vortex intensification and its effect on a serial mesoscale convective system. *Mon. Wea. Rev.*, **130**, 2839-2858.
- , and -----, 2007: Mesoscale convective vortices observed during BAMEX. Part I: Kinematic and thermodynamic structure. *Mon. Wea. Rev.*, **135**, 2029-2049.
- , and M. L. Weisman, 1994: Balanced dynamics of mesoscale vortices produced in simulated convective systems. *J. Atmos. Sci.*, **51**, 2005-2030.
- , D. A. Ahijevych, and S. B. Trier, 2002: Detection and prediction of warm season midtropospheric vortices by the Rapid Update Cycle. *Mon. Wea. Rev.*, **130**, 24-42.
- , and Coauthors, 2004: The Bow Echo and MCV Experiment: Observations and opportunities. *Bull. Amer. Meteor. Soc.*, **85**, 1075-1093.
- Dell'Osso, L. D., and S.-J. Chen, 1986: Numerical experiments on the genesis of vortices over the Qinghai-Tibet plateau. *Tellus*, **38A**, 236-250.
- Emanuel, K. E., J. Callaghan, and P. Otto, 2008: A hypothesis for the redevelopment of warm-core cyclones over northern Australia. *Mon. Wea. Rev.*, **136**, 3863-3872.
- Fankhauser, J. C., 1974: The derivation of consistent fields of wind and geopotential height from mesoscale rawinsonde data. *J. Appl. Meteor.*, **13**, 637-646.
- Feteris, P. J., 1961: The influence of the circulation around cumulonimbus clouds on the surface humidity pattern. *Swiss Aero Rev.*, **36**, 626-630.
- , 1978: Comments on "Formation of mesolows or pressure troughs in advance of cumulonimbus clouds". *Mon. Wea. Rev.*, **106**, 1031-1034.
- Fortune, M. A., 1980: Properties of African squall lines inferred from time-lapse satellite imagery. *Mon. Wea. Rev.*, **108**, 153-168.
- , W. R. Cotton, and R. L. McAnelly, 1992: Frontal-wave-like evolution in some mesoscale convective complexes. *Mon. Wea. Rev.*, **120**, 1279-1300.
- Freeman, J. C., Jr., 1950: Map analysis in the vicinity of a pressure jump. *Bull. Amer. Meteor. Soc.*, **31**, 324-325.
- Fritsch, J. M., and C. F. Chappell, 1980a: Numerical prediction of convectively driven

- mesoscale pressure systems. Part I: Convective parameterization. *J. Atmos. Sci.*, **37**, 1722-1733.
- , and -----, 1980b: Numerical prediction of convectively driven mesoscale pressure systems. Part II: Mesoscale model. *J. Atmos. Sci.*, **37**, 1734-1762.
- , J. D. Murphy, and J. S. Kain, 1994: Warm core vortex amplification over land. *J. Atmos. Sci.*, **51**, 1780-1807.
- Fujita, T. T., 1951: Microanalytical study of thunder-nose. *Geophys. Mag. Tokyo*, **22**, 78-88.
- , 1955: Result of detailed synoptic studies of squall lines. *Tellus*, **7**, 405-436.
- , 1959: Precipitation and cold air production in mesoscale thunderstorm systems. *J. Meteor.*, **16**, 454-466.
- , and R. M. Wakimoto, 1981: Five scales of airflow associated with a series of downbursts on 16 July 1980. *Mon. Wea. Rev.*, **109**, 1438-1456.
- Galarneau, T. J., and L. F. Bosart, 2005: An examination of the long-lived MCV of 10-13 June 2003. Preprints, *11th Conf. on Mesoscale Processes*, Albuquerque, NM, Amer. Meteor. Soc., 5-7.
- Gallus, W. A., Jr., 1996: The influence of microphysics in the formation of intense wake lows: A numerical modeling study. *Mon. Wea. Rev.*, **124**, 2267-2281.
- Gamache, J. F., and R. A. Houze, Jr., 1982: Mesoscale air motions associated with a tropical squall line. *Mon. Wea. Rev.*, **110**, 118-135.
- , and -----, 1985: Further analysis of the composite wind and thermodynamic structure of the 12 September GATE squall line. *Mon. Wea. Rev.*, **113**, 1241-1259.
- Garratt, J. R., and W. L. Physick, 1983: Low-level wind response to mesoscale pressure systems. *Bound.-Layer Meteor.*, **27**, 69-87.
- Goff, R. C., 1976: Vertical structure of thunderstorm outflows. *Mon. Wea. Rev.*, **104**, 1429-1440.
- Haertel, P. T., and R. H. Johnson, 1998: The dynamics of surface pressure within squall systems. Preprints, *19th Conf. on Severe Local Storms*, Minneapolis, MN, Amer. Meteor. Soc., 392-394.
- , and -----, 2000: The linear dynamics of squall line mesohighs and wake lows. *J. Atmos. Sci.*, **57**, 93-107.
- Hales, J. E., 1990: An examination of the development and role of a mesoscale vorticity center in the Council Bluffs tornado on 15 July 1988. Preprints, *16th Conf. on Severe Local Storms*, Kananaskis Park, AB, Canada, Amer. Meteor. Soc., 446-

449.

- Hane, C. E., C. J. Kessinger, and P. S. Ray, 1987: The Oklahoma squall line of 19 May 1977. Part II: Mechanisms for maintenance of the region of strong convection. *J. Atmos. Sci.*, **44**, 2866-2883.
- Harr, P. A., and R. L. Elsberry, 1996: Structure of a mesoscale convective system embedded in Typhoon Robyn during TCM-93. *Mon. Wea. Rev.*, **124**, 634-652.
- , -----, and J. C. L. Chan, 1996a: Transformation of a large monsoon depression to a tropical storm during TCM-93. *Mon. Wea. Rev.*, **124**, 2625-2643.
- , M. S. Kalafsky, and R. L. Elsberry, 1996b: Environmental conditions prior to formation of a midget tropical cyclone during TCM-93. *Mon. Wea. Rev.*, **124**, 1693-1710.
- Hawblitzel, D. P., F. Zhang, Z. Meng, and C. A. Davis, 2007: Probabilistic evaluation of the dynamics and predictability of the mesoscale convective vortex of 10-13 June 2003. *Mon. Wea. Rev.*, **135**, 1544-1563.
- Hertenstein, R. F. A., and W. H. Schubert, 1991: Potential vorticity anomalies associated with squall lines. *Mon. Wea. Rev.*, **119**, 1663-1672.
- Houze, R. A., Jr., 1977: Structure and dynamics of a tropical squall-line system. *Mon. Wea. Rev.*, **105**, 1540-1567.
- , and A. K. Betts, 1981: Convection in GATE. *Rev. Geophys. Space Phys.*, **19**, 541-576.
- , and E. N. Rappaport, 1984: Air motions and precipitation structure of an early summer squall line over the eastern tropical Atlantic. *J. Atmos. Sci.*, **41**, 553-574.
- , S. A. Rutledge, M. I. Biggerstaff, and B. F. Smull, 1989: Interpretation of Doppler weather radar displays of midlatitude mesoscale convective systems. *Bull. Amer. Meteor. Soc.*, **70**, 608-619.
- , B. F. Smull, and P. Dodge, 1990: Mesoscale organization of springtime rainstorms in Oklahoma. *Mon. Wea. Rev.*, **118**, 613-654.
- Hoxit, L. R., C. F. Chappell, and J. M. Fritsch, 1976: Formation of mesolows or pressure troughs in advance of cumulonimbus clouds. *Mon. Wea. Rev.*, **104**, 1419-1428.
- , -----, and -----, 1977: Reply and corrigendum. *Mon. Wea. Rev.*, **105**, 1063-1066.
- Huang, F.-J., 1986: A composite analysis of the southwest vortex. *Sci. Atmos. Sin.*, **10**, 402-408.
- , and H.-D. Xiao, 1989: Mesoscale characteristics of a heavy precipitation event produced by a southwest-vortex. *Meteorology*, **15**, 3-8.

- Jiang, H., and D. J. Raymond, 1995: Simulation of a mature mesoscale convective system using a non-linear balance model. *J. Atmos. Sci.*, **52**, 161-175.
- Johnson, B. C., 1983: The heat burst of 29 May 1976. *Mon. Wea. Rev.*, **111**, 1776-1792.
- Johnson, R. H., 2001: Surface mesohighs and mesolows. *Bull. Amer. Meteor. Soc.*, **82**, 13-31.
- , and D. L. Bartels, 1992: Circulations associated with a mature-to-decaying midlatitude mesoscale convective system. Part II: Upper-level features. *Mon. Wea. Rev.*, **120**, 1301-1320.
- , and W. A. Gallus, Jr., 1988: The wake structure of an intense midlatitude squall line in OK PRE-STORM. Preprints, *Eighth Conf. on Numerical Weather Prediction and 15th Conf. on Severe Local Storms*, Baltimore, MD, Amer. Meteor. Soc., 229-232.
- , and P. J. Hamilton, 1988: The relationship of surface pressure features to the precipitation and airflow structure of an intense midlatitude squall line. *Mon. Wea. Rev.*, **116**, 1444-1472.
- , and M. E. Nicholls, 1983: A composite analysis of the boundary layer accompanying a tropical squall line. *Mon. Wea. Rev.*, **111**, 308-319.
- , S. Chen, and J. J. Toth, 1989: Circulations associated with a mature-to-decaying midlatitude mesoscale convective system. Part I: Surface features—heat bursts and mesolow development. *Mon. Wea. Rev.*, **117**, 942-959.
- , E. R. Hilgendorf, and K. C. Crawford, 1996: Study of midwestern mesoscale convective systems using new operational networks. Preprints, *18th Conf. on Severe Local Storms*, San Francisco, CA, Amer. Meteor. Soc., 308-312.
- Johnston, E. C., 1982: Mesoscale vorticity centers induced by mesoscale convective complexes. Preprints, *Ninth Conf. On Weather Analysis and Forecasting*, Seattle, WA, Amer. Meteor. Soc., 196-200.
- Jou, B. J.-D., and C.-K. Yu, 1993: Structure of a tropical convective system and associated vortex: A TAMEX case study. *Proc. 26th Int. Radar Conf.*, Norman, OK, Amer. Meteor. Soc., 65-67.
- Keenan, T. D., and S. A. Rutledge, 1993: Mesoscale characteristics of monsoonal convection and associated stratiform precipitation. *Mon. Wea. Rev.*, **121**, 352-374.
- Kessinger, C. J., P. S. Ray, and C. E. Hane, 1987: The Oklahoma squall line of 19 May 1977. Part I: A multiple Doppler analysis of convective and stratiform structure. *J. Atmos. Sci.*, **44**, 2840-2864.
- Kieu, C. Q., and D.-L. Zhang, 2008: Genesis of Tropical Storm Eugene (2005) from merging vortices associated with ITCZ breakdowns. Part I: Observational and

- modeling analyses. *J. Atmos. Sci.*, **65**, 3419-3439.
- Kirk, J. R., 2003: Comparing the dynamical development of two mesoscale convective vortices. *Mon. Wea. Rev.*, **131**, 862-890.
- , 2007: A phase-plot method for diagnosing vorticity concentration mechanisms in mesoscale convective vortices. *Mon. Wea. Rev.*, **135**, 801-820.
- Kniewel, J. C., and R. H. Johnson, 1998: Pressure transients within MCS mesohighs and wake lows. *Mon. Wea. Rev.*, **126**, 1907-1930.
- , and -----, 2002: The kinematics of a midlatitude, continental mesoscale convective system and its mesoscale vortex. *Mon. Wea. Rev.*, **130**, 1749-1770.
- , and -----, 2003: A scale-discriminating vorticity budget for a mesoscale vortex in a midlatitude, continental mesoscale convective system. *J. Atmos. Sci.*, **60**, 781-794.
- , D. S. Nolan, and J. P. Kossin, 2004: Imbalance in a mesoscale vortex within a midlatitude, continental mesoscale convective system. *J. Atmos. Sci.*, **61**, 1827-1832.
- Kuettner, J. P., D. E. Parker, D. R. Rodenhuis, H. Hoerber, H. Kraus, and S. G. H. Philander, 1974: GATE: Final international scientific plans. *Bull. Amer. Meteor. Soc.*, **55**, 711-744.
- Kuo, Y.-H., and G. T.-J. Chen, 1990: The Taiwan Area Mesoscale Experiment (TAMEX): An overview. *Bull. Amer. Meteor. Soc.*, **71**, 488-503.
- , L. Cheng, and R. A. Anthes, 1986: Mesoscale analyses of Sichuan flood catastrophe, 11-15 July 1981. *Mon. Wea. Rev.*, **114**, 1984-2003.
- , -----, and J.-W. Bao, 1988: Numerical simulation of the 1981 Sichuan flood. Part 1: Evolution of a mesoscale southwest vortex. *Mon. Wea. Rev.*, **116**, 2481-2504.
- Laing, A. G., and J. M. Fritsch, 1993a: Mesoscale convective complexes over the Indian monsoon region. *J. Climate*, **6**, 911-919.
- , and -----, 1993b: Mesoscale convective complexes in Africa. *Mon. Wea. Rev.*, **121**, 2254-2263.
- Leary, C. A., 1979: Behavior of the wind field in the vicinity of a cloud cluster in the intertropical convergence zone. *J. Atmos. Sci.*, **36**, 631-639.
- , and E. N. Rappaport, 1987: The life cycle and internal structure of a mesoscale convective complex. *Mon. Wea. Rev.*, **115**, 1503-1527.
- Levine, J., 1942: Effect of vertical accelerations on pressure during thunderstorms. *Bull. Amer. Meteor. Soc.*, **23**, 52-61.

- Litta, A. J., B. Chakrapani, and K. Mohankumar, 2007: Mesoscale simulation of an extreme rainfall event over Mumbai, India, using a high-resolution MM5 model. *Meteor. Appl.*, **14**, 291-295.
- Loehrer, S. M., and R. H. Johnson, 1995: Surface pressure and precipitation life cycle characteristics of PRE-STORM mesoscale convective systems. *Mon. Wea. Rev.*, **123**, 600-621.
- Ma, K.-Y., and L. F. Bosart, 1987: A synoptic overview of a heavy rain event in southern China. *Wea. Forecasting*, **2**, 89-112.
- Maddox, R. A., 1980: Mesoscale convective complexes. *Bull. Amer. Meteor. Soc.*, **61**, 1374-1387.
- , 1983: Large-scale meteorological conditions associated with midlatitude, mesoscale convective complexes. *Mon. Wea. Rev.*, **111**, 1475-1493.
- Magor, B. W., 1958: A meso-low associated with a severe storm. *Mon. Wea. Rev.*, **86**, 81-90.
- Mal, S., and Y. P. Rao, 1945: Effect of vertical accelerations on pressure during thunderstorms. *Quart. J. Roy. Meteor. Soc.*, **71**, 419-421.
- Mapes, B. E., and R. A. Houze, Jr., 1995: Diabatic divergence profiles in western Pacific mesoscale convective systems. *J. Atmos. Sci.*, **52**, 1807-1828.
- Marwitz, J. D., 1972: Non-hydrostatic pressures in severe thunderstorms. Preprints, *Eighth Conf. on Severe Local Storms*, Denver, CO, Amer. Meteor. Soc., 14-17.
- May, P. T., J. H. Mather, G. Vaughan, C. Jakob, G. M. McFarquhar, K. N. Bower, and G. G. Mace, 2008: The Tropical Warm Pool International Cloud Experiment. *Bull. Amer. Meteor. Soc.*, **89**, 629-645.
- McNulty, R. P., 1991: Downbursts from innocuous clouds: An example. *Wea. Forecasting*, **6**, 148-154.
- McPherson, R. A., and Coauthors, 2007: Statewide monitoring of the mesoscale environment: A technical update on the Oklahoma Mesonet. *J. Atmos. Oceanic Technol.*, **24**, 301-321.
- Menard, R. D., and J. M. Fritsch, 1989: A mesoscale convective complex-generated inertially stable warm core vortex. *Mon. Wea. Rev.*, **117**, 1237-1261.
- , J. H. Merritt, J. M. Fritsch, and P. A. Hirschberg, 1986: Mesoanalysis of a convectively generated, inertially stable mesovortex. Preprints, *11th Conf. on Weather Forecasting and Analysis*, Kansas City, MO, Amer. Meteor. Soc., 194-199.
- , D. L. Sims, and J. M. Fritsch, 1988: Case example of the effect of a wake low on

- subsequent convective events. Preprints, *15th Conf. on Severe Local Storms*, Baltimore, MD, Amer. Meteor. Soc., 225-228.
- Miller, D., and J. M. Fritsch, 1991: Mesoscale convective complexes in the western Pacific region. *Mon. Wea. Rev.*, **119**, 2978-2992.
- Miller, M. J., and A. K. Betts, 1977: Traveling convective storms over Venezuela. *Mon. Wea. Rev.*, **105**, 833-848.
- Montgomery, M. T., and J. Enagonio, 1998: Tropical cyclogenesis via convectively forced vortex Rossby waves in a three-dimensional quasigeostrophic model. *J. Atmos. Sci.*, **55**, 3176-3207.
- Mueller, C. K., and R. E. Carbone, 1987: Dynamics of a thunderstorm outflow. *J. Atmos. Sci.*, **44**, 1879-1898.
- Murphy, J. D., and J. M. Fritsch, 1989: Multiple production of mesoscale convective systems by a convectively-generated mesoscale vortex. Preprints, *12th Conf. on Weather Analysis and Forecasting*, Monterey, CA, Amer. Meteor. Soc., 68-73.
- Nachamkin, J. E., R. L. McAnelly, and W. R. Cotton, 1994: An observational analysis of a developing mesoscale convective complex. *Mon. Wea. Rev.*, **122**, 1168-1188.
- Nastrom, G. D., and T. E. VanZandt, 1996: Biases due to gravity waves in wind profiler measurements of winds. *J. Appl. Meteor.*, **35**, 243-257.
- Newton, C. W., 1950: Structure and mechanism of the prefrontal squall line. *J. Meteor.*, **7**, 210-222.
- Nicholls, M. E., R. H. Johnson, and W. R. Cotton, 1988: The sensitivity of two-dimensional simulations of tropical squall lines to environmental profiles. *J. Atmos. Sci.*, **45**, 3625-3649.
- North, E. M., A. M. Peterson, and H. D. Parry, 1973: RASS, a remote sensing system for measuring low-level temperature profiles. *Bull. Amer. Meteor. Soc.*, **54**, 912-919.
- Nuss, W. A., and D. W. Titley, 1994: Use of multiquadratic interpolation for meteorological objective analysis. *Mon. Wea. Rev.*, **122**, 1611-1631.
- Ogura, Y., and M.-T. Liou, 1980: The structure of a midlatitude squall line: A case study. *J. Atmos. Sci.*, **37**, 553-567.
- Olsson, P. Q., and W. R. Cotton, 1997a: Balanced and unbalanced circulations in a primitive equation simulation of a midlatitude MCC. Part I: The numerical simulation. *J. Atmos. Sci.*, **54**, 457-478.
- , and -----, 1997b: Balanced and unbalanced circulations in a primitive equation simulation of a midlatitude MCC: Part II: Analysis of balance. *J. Atmos. Sci.*, **54**, 479-497.

- Pandya, R. E., and D. R. Durran, 1996: The influence of convectively generated thermal forcing on the mesoscale circulation around squall lines. *J. Atmos. Sci.*, **53**, 2924-2951.
- , -----, and M. L. Weisman, 2000: The influence of convective thermal forcing on the three-dimensional circulation around squall lines. *J. Atmos. Sci.*, **57**, 29-45.
- Parker, M. D., and R. H. Johnson, 2000: Organizational modes of midlatitude mesoscale convective systems. *Mon. Wea. Rev.*, **128**, 3413-3436.
- Purdom, J. F. W., 1973: Meso-highs and satellite imagery. *Mon. Wea. Rev.*, **101**, 180-181.
- Raymond, D. J., and H. Jiang, 1990: A theory for long-lived mesoscale convective systems. *J. Atmos. Sci.*, **47**, 3067-3077.
- Reasor, P. D., M. T. Montgomery, and L. F. Bosart, 2005: Mesoscale observations of the genesis of Hurricane Dolly (1996). *J. Atmos. Sci.*, **62**, 3151-3171.
- Ritchie, E. A., and G. J. Holland, 1997: Scale interactions during the formation of Typhoon Irving. *Mon. Wea. Rev.*, **125**, 1377-1396.
- , -----, and J. Simpson, 1995: Contributions by mesoscale convective systems to the development of Tropical Cyclone Oliver. Preprints, *21st Conf. on Hurricanes and Tropical Meteorology*, Miami, FL, Amer. Meteor. Soc., 570-572.
- Rogers, R. F., and J. M. Fritsch, 2001: Surface cyclogenesis from convectively driven amplification of midlevel mesoscale convective vortices. *Mon. Wea. Rev.*, **129**, 605-637.
- Roux, F., J. Testud, M. Payen, and B. Pinty, 1984: West African squall-line thermodynamic structure retrieved from dual-Doppler radar observations. *J. Atmos. Sci.*, **41**, 3104-3121.
- , -----, B. Pinty, and J. P. Chalon, 1982: Dual-Doppler radar and surface network observations of a West-African squall line during the "COPT 81" experiment. Preprints, *Conf. Cloud Physics*, Chicago, IL, Amer. Meteor. Soc., 547-550.
- Rutledge, S. A., E. A. Williams, and T. D. Keenan, 1992: The Down Under Doppler and Electricity Experiment (DUNDEE): Overview and preliminary results. *Bull. Amer. Meteor. Soc.*, **73**, 3-16.
- Sanders, F., 1977: Comments on "Formation of mesolows or pressure troughs in advance of cumulonimbus clouds". *Mon. Wea. Rev.*, **105**, 1061-1063.
- Sawyer, J. S., 1946: Cooling by rain as the cause of the pressure rise in convective squalls. *Quart. J. Roy. Meteor. Soc.*, **72**, 168.
- Schaffer, W., 1947: The thunderstorm high. *Bull. Amer. Meteor. Soc.*, **28**, 351-355.

- Schumacher, R. S., and R. H. Johnson, 2008: Mesoscale processes contributing to extreme rainfall in a midlatitude warm-season flash flood. *Mon. Wea. Rev.*, **136**, 3964-3986.
- Scott, J. D., and S. A. Rutledge, 1995: Doppler radar observations of an asymmetric mesoscale convective system and associated vortex couplet. *Mon. Wea. Rev.*, **123**, 3437-3457.
- Simpson, J., E. A. Ritchie, G. J. Holland, J. Halverson, and S. Stewart, 1997: Mesoscale interactions in tropical cyclone genesis. *Mon. Wea. Rev.*, **125**, 2643-2661.
- Skamarock, W. C., M. L. Weisman, and J. B. Klemp, 1994: Three-dimensional evolution of simulated long-lived squall lines. *J. Atmos. Sci.*, **51**, 2563-2584.
- Smith, W. P., and R. L. Gall, 1989: Tropical squall lines of the Arizona monsoon. *Mon. Wea. Rev.*, **117**, 1553-1569.
- Smull, B. F., and R. A. Houze, Jr., 1985: A midlatitude squall line with a trailing region of stratiform rain: Radar and satellite observations. *Mon. Wea. Rev.*, **113**, 117-133.
- , and D. P. Jorgensen, 1990: Pressure and buoyancy perturbations near an intense wake low in a midlatitude mesoscale convective system. *Preprints, Fourth Conf. on Mesoscale Processes*, Boulder, CO, Amer. Meteor. Soc., 214-215.
- , -----, and C. E. Hane, 1991: Comparison of retrieved pressure and buoyancy perturbations with in situ observations of an intense wake low in a midlatitude mesoscale convective system. *Preprints, 25th Int. Conf. on Radar Meteorology*, Paris, France, Amer. Meteor. Soc., 135-138.
- Sommeria, G., and J. Testud, 1984: COPT 81: A field experiment designed for the study of dynamics and electrical activity of deep convection in continental tropical regions. *Bull. Amer. Meteor. Soc.*, **65**, 4-10.
- Stirling, J., and R. M. Wakimoto, 1989: Mesoscale vortices in the stratiform region of a decaying mid-latitude squall line. *Mon. Wea. Rev.*, **117**, 452-458.
- Stumpf, G. J., R. H. Johnson, and B. F. Smull, 1991: The wake low in a midlatitude mesoscale convective system having complex convective organization. *Mon. Wea. Rev.*, **119**, 134-158.
- Tao, S.-Y. and Y.-H. Ding, 1981: Observational evidence of the influence of the Qinghai-Xizang (Tibet) plateau on the occurrence of heavy rain and severe convective storms in China. *Bull. Amer. Meteor. Soc.*, **62**, 23-30.
- Tepper, M., 1950: A proposed mechanism of squall lines: The pressure jump line. *J. Meteor.*, **7**, 21-29.
- , 1955: On the generation of pressure-jump lines by the impulsive addition of

- momentum to simple current systems. *J. Meteor.*, **12**, 287-297.
- Tollerud, E. I., J. M. Brown, and D. L. Bartels, 1989: Structure of an MCS-induced mesoscale vortex as revealed by VHF profiler, Doppler radar, and satellite observations. Preprints, *12th Conf. on Weather Analysis and Forecasting*, Monterey, CA, Amer. Meteor. Soc., 81-86.
- Trier, S. B., and C. A. Davis, 2002: Influence of balanced motions on heavy precipitation within a long-lived convectively generated vortex. *Mon. Wea. Rev.*, **130**, 877-899.
- , and -----, 2007: Mesoscale convective vortices observed during BAMEX. Part II: Influences on secondary deep convection. *Mon. Wea. Rev.*, **135**, 2051-2075.
- , -----, and W. C. Skamarock, 2000a: Long-lived mesoconvective vortices and their environment. Part II: Induced thermodynamic destabilization in idealized simulations. *Mon. Wea. Rev.*, **128**, 3396-3412.
- , -----, and J. D. Tuttle, 2000b: Long-lived mesoconvective vortices and their environment. Part I: Observations from the central United States during the 1998 warm season. *Mon. Wea. Rev.*, **128**, 3376-3395.
- Velasco, I., and J. M. Fritsch, 1987: Mesoscale convective complexes in the Americas. *J. Geophys. Res.*, **92**, 9591-9613.
- Verlinde, J., and W. R. Cotton, 1990: A mesoscale vortex couplet observed in the trailing anvil of a multicellular convective complex. *Mon. Wea. Rev.*, **118**, 993-1010.
- Vescio, M. D., and R. H. Johnson, 1992: The surface-wind response to transient mesoscale pressure fields associated with squall lines. *Mon. Wea. Rev.*, **120**, 1837-1850.
- Wakimoto, R. M., 1982: The life cycle of thunderstorm gust fronts as viewed with Doppler radar and rawinsonde data. *Mon. Wea. Rev.*, **110**, 1060-1082.
- Wang, B., 1987: The development mechanism for Tibetan plateau warm vortices. *J. Atmos. Sci.*, **44**, 2978-2994.
- , and I. Orlanski, 1987: Study of a heavy rain vortex formed over the eastern flank of the Tibetan plateau. *Mon. Wea. Rev.*, **115**, 1370-1393.
- Wang, W., Y.-H. Kuo, and T. T. Warner, 1993: A diabatically driven mesoscale vortex in the lee of the Tibetan plateau. *Mon. Wea. Rev.*, **121**, 2542-2561.
- Weber, B. L., D. B. Wuertz, D. C. Welsh, and R. McPeck, 1993: Quality controls for profiler measurements of winds and RASS temperatures. *J. Atmos. Oceanic Technol.*, **10**, 452-464.
- , and Coauthors, 1990: Preliminary evaluation of the first NOAA demonstration network wind profiler. *J. Atmos. Oceanic Technol.*, **7**, 909-918.

- Webster, P. J., and R. Lukas, 1992: TOGA COARE: The Coupled Ocean-Atmosphere Response Experiment. *Bull. Amer. Meteor. Soc.*, **73**, 1377-1416.
- Wei, T., and R. A. Houze, Jr., 1987: The GATE squall line of 9-10 August 1974. *Advances in Atmospheric Sciences*, **4**, 85-92.
- Weisman, M. L., and C. A. Davis, 1998: Mechanisms for the generation of mesoscale vortices within quasi-linear convective systems. *J. Atmos. Sci.*, **55**, 2603-2622.
- , W. C. Skamarock, J. B. Klemp, and C. Davis, 1993: The generation of mesoscale convective vortices within long-lived convective systems. Preprints, *20th Conf. on Hurricanes and Tropical Meteorology*, San Antonio, TX, Amer. Meteor. Soc., 120-123.
- Wetzel, P. J., W. R. Cotton, and R. L. McAnelly, 1983: A long-lived mesoscale convective complex. Part II: Evolution and structure of the mature complex. *Mon. Wea. Rev.*, **111**, 1919-1937.
- Wicker, L. J., and W. C. Skamarock, 1996: The dynamics governing surface pressure fields in mesoscale convective systems. Preprints, *Seventh Conf. on Mesoscale Processes*, Reading, United Kingdom, Amer. Meteor. Soc., 476-478.
- Wilczak, J. M., R. G. Strauch, F. M. Ralph, B. L. Weber, D. A. Merritt, J. R. Jordan, D. E. Wolfe, L. K. Lewis, D. B. Wuertz, and J. E. Gaynor, 1995: Contamination of wind profiler data by migrating birds: characteristics of corrupted data and potential solutions. *J. Atmos. Oceanic Technol.*, **12**, 449-467.
- Williams, D. T., 1948: A surface micro-study of squall-line thunderstorms. *Mon. Wea. Rev.*, **76**, 239-246.
- , 1953: Pressure wave observations in the central Midwest, 1952. *Mon. Wea. Rev.*, **81**, 278-289.
- , 1954: A surface study of a depression-type pressure wave. *Mon. Wea. Rev.*, **82**, 289-295.
- Wuertz, D. B., B. L. Weber, R. G. Strauch, A. S. Frisch, C. G. Little, D. A. Merritt, K. P. Moran, and D. C. Welsh, 1988: Effects of precipitation on UHF wind profiler measurements. *J. Atmos. Oceanic Technol.*, **5**, 450-465.
- Yu, C.-K., B. J.-D. Jou, and B. F. Smull, 1999: Formative stage of a long-lived mesoscale vortex observed by airborne Doppler radar. *Mon. Wea. Rev.*, **127**, 838-857.
- Zhang, D.-L., 1992: The formation of a cooling-induced mesovortex in the trailing stratiform region of a midlatitude squall line. *Mon. Wea. Rev.*, **120**, 2763-2785.
- , and N. Bao, 1996a: Oceanic cyclogenesis as induced by a mesoscale convective system moving offshore. Part I: A 90-h real-data simulation. *Mon. Wea. Rev.*, **124**,

- 1449-1469.
- , and -----, 1996b: Oceanic cyclogenesis as induced by a mesoscale convective system moving offshore. Part II: Genesis and thermodynamic transformation. *Mon. Wea. Rev.*, **124**, 2206-2225.
- , and J. M. Fritsch, 1985: Numerical simulation of a meso- β scale warm-core vortex over land. Preprints, *14th Conf. on Severe Local Storms*, Indianapolis, IN, Amer. Meteor. Soc., 29-32.
- , and -----, 1986: Numerical simulation of the meso- β scale structure and evolution of the 1977 Johnstown flood. Part I: Model description and verification. *J. Atmos. Sci.*, **43**, 1913-1943.
- , and -----, 1987: Numerical simulation of the meso- β scale structure and evolution of the 1977 Johnstown flood. Part II: Inertially stable warm-core vortex and the mesoscale convective complex. *J. Atmos. Sci.*, **44**, 2593-2612.
- , and -----, 1988a: Numerical sensitivity experiments of varying model physics on the structure, evolution and dynamics of two mesoscale convective systems. *J. Atmos. Sci.*, **45**, 261-293.
- , and -----, 1988b: Numerical simulation of the meso- β scale structure and evolution of the 1977 Johnstown flood. Part III: Internal gravity waves and the squall line. *J. Atmos. Sci.*, **45**, 1252-1268.
- , and -----, 1988c: A numerical investigation of a convectively generated, inertially stable, extratropical warm-core mesovortex over land. Part I: Structure and evolution. *Mon. Wea. Rev.*, **116**, 2660-2687.
- , and K. Gao, 1989: Numerical simulation of an intense squall line during 10-11 June 1985 PRE-STORM. Part II: Rear inflow, surface pressure perturbations and stratiform precipitation. *Mon. Wea. Rev.*, **117**, 2067-2094.
- , and R. Harvey, 1995: Enhancement of extratropical cyclogenesis by a mesoscale convective system. *J. Atmos. Sci.*, **52**, 1107-1127.
- , K. Gao, and D. B. Parsons, 1989: Numerical simulation of an intense squall line during 10-11 June 1985 PRE-STORM. Part I: Model verification. *Mon. Wea. Rev.*, **117**, 960-994.
- Zipser, E. J., 1977: Mesoscale and convective-scale downdrafts as distinct components of squall-line structure. *Mon. Wea. Rev.*, **105**, 1568-1589.